Louisiana State University
LSU Digital Commons

LSU Doctoral Dissertations | Graduate School

3-27-2020

# Transition Metal-doped Rare-earth Oxysulfide Catalysts for High Temperature Dry Reforming of Methane

Changyi Jiang
*Louisiana State University and Agricultural and Mechanical College*

Follow this and additional works at: https://digitalcommons.lsu.edu/gradschool_dissertations

 Part of the Catalysis and Reaction Engineering Commons

## Recommended Citation

Jiang, Changyi, "Transition Metal-doped Rare-earth Oxysulfide Catalysts for High Temperature Dry Reforming of Methane" (2020). *LSU Doctoral Dissertations*. 5196.
https://digitalcommons.lsu.edu/gradschool_dissertations/5196

This Dissertation is brought to you for free and open access by the Graduate School at LSU Digital Commons. It has been accepted for inclusion in LSU Doctoral Dissertations by an authorized graduate school editor of LSU Digital Commons. For more information, please contactgradetd@lsu.edu.

# TRANSITION METAL-DOPED RARE-EARTH OXYSULFIDE CATALYSTS FOR HIGH TEMPERATURE DRY REFORMING OF METHANE

A Dissertation

Submitted to the Graduate Faculty of the
Louisiana State University and
Agricultural and Mechanical College
in partial fulfillment of the
requirements for the degree of
Doctor of Philosophy

in

The Gordon A. and Mary Cain Department of Chemical Engineering

by
Changyi Jiang
B.S., Dalian University of Technology, 2011
M.S., Michigan Technological University, 2013
May 2020

# ACKNOWLEDGEMENTS

I would like to express my deepest gratitude to my advisor and mentor, Dr. Kerry Dooley, who guided and supported me during the process of pursuing my Ph.D. He trained me to think as a real engineer with great patience and taught me how to solve practical problems.

I would also like to thank my committee, Dr. Michael Benton, Dr. Ye Xu, and Dr. Phillip Sprunger for their valuable and professional advice on my research work. I want to express my gratitude to Dr. Michael Janik and his group member, Bo Li (Penn St. Univ.) for their support on the DFT work. I would also like to thank the National Science Foundation for financial support.

I want to acknowledge Oak Ridge National Laboratory and Dr. David Cullen, and also Dr. James Dorman and his group members, especially Natalia da Silva Moura and Behnam Safavinia (LSU), for their assistance in the TEM experiments. My sincere thanks also go to Dr. Amitava Roy and Dr. Orhan Kizilkaya of the Center for Advanced Microstructures & Devices (LSU), who helped me with both XAS and XPS experimental setup and measurement.

I want to thank my group member, Jaren Lee, who provided great help for the catalyst synthesis work and encouraged me to get through my toughest first year. In addition, of the Chemical Engineering department staff I am indebted to Joe Bell (mechanical shop), Rachel Landry (administrative), Darla Dao and Danny Fontenot for their wholehearted support. My special thanks also go to Emily Loisel and J.C. Davila (undergraduate student workers), who helped me with the lab work. At last, I want to thank my parents and beloved wife, Dr. Tao Jin, for their unconditional love and support. It is their encouragement that has seen me through the most difficult times and make all things possible.

# TABLE OF CONTENTS

# LIST OF TABLES

# LIST OF FIGURES

# ABSTRACT

Carbon dioxide reforming of methane is a catalytic reaction utilizing two kinds of greenhouse gases and converting them into a useful industrial gas stream, “syngas”. However, sulfur poisoning and coke formation are two major challenges for this reaction. In this study, we have synthesized and examined several Ce-La and Ce-Zr oxides, with different transition metal additives. A rapid screening technique was developed to measure reforming and coking rates at low partial pressures. It is a good indicator of catalyst behavior at higher conversions and partial pressures. Following the rapid screening, select catalysts were examined at longer times on stream. Those containing Ni and Co together were the most stable. Catalysts containing Ce-La oxides lacked practicality, partly due to more reverse water-gas shift. Catalysts containing Ce-Zr oxides fared better, with Ce/Zr = 3 (molar) showing the best stability for Ni-based catalysts. Reaction and deactivation results for Ni- and Ni/Co-containing catalysts could be explained partly in terms of DFT calculations, and partly in terms of spent catalyst characterizations. The Ni interacts strongly with the mixed oxides, even when it is in a mostly reduced state, as in Ce-Zr.

Ni-based catalysts were also examined for sulfur tolerance based on long-term reactor tests. Catalysts prepared on both Ce/Zr and Ce/La oxide supports, some without and some with additional Co metal, were tested under low and high conversion conditions. Long-term reaction runs were conducted both with and without sulfur added to the feed. The catalysts were also characterized by TEM, XPS, XAFS, and CO chemisorption. Only catalysts where Co is also present, and with the metals combined with a Ce-Zr oxide, are capable of extended sulfur tolerance at >20 ppm sulfur. This tolerance, and also a greatly reduced coking rate, is linked to

Co in contact with the Ni and existing in small aggregates where $CH_4$ activation takes place, anchored and influenced electronically by the oxide support. Larger metal aggregates formed during reaction appear to be spectators. Measured activation energies for the dry reforming reaction support the hypothesis that $CO_2$ activation takes place at the oxide interface and is a kinetically significant step.

# CHAPTER 1. INTRODUCTION AND LITERATURE REVIEW

## 1.1. Carbon Dioxide Reforming of Methane

Carbon dioxide reforming of methane ($CH_4 + CO_2 \rightarrow 2H_2 + 2CO$; abbreviated as DRM henceforth), also known as dry reforming of methane, is a process which can produce synthesis gas (mixtures of hydrogen and carbon monoxide) from carbon dioxide and methane. Compared with the steam reforming route, one of its advantages is the utilization of carbon dioxide, which is the most thermodynamically stable among all the greenhouse gases. The low ratio $H_2/CO_2$ syngas obtained in DRM can be used in the Fisher-Tropsch process to produce diesel or be converted into methane and methanol via other catalytic processes.[1, 2] In this way, two kinds of greenhouse gases are consumed and transformed into useful industrial materials.

However, the high symmetry methane molecule is very stable.[3] Also, the gas phase ionization energy of $CO_2$ is about 13.8 eV,[4] which means the $CO_2$ molecule is quite stable as well. In this case, high temperature and a catalyst are needed to overcome the DRM reaction energy barrier when methane is transformed or decomposed. The temperature range for DRM is usually 600-1000°C and many classes of catalysts have been studied, such as those containing noble metals and also most of the base transition metals from groups 7-11.DRM also has been studied over a wide GHSV range (2.9-230 L/gcat*h) at pressures of 1-10 atm. The $CH_4/CO_2$ feed ratio is usually 1, however, higher or lower ratios also have been studied. During tri-reforming, which involves $CO_2$ reforming, steam reforming, and oxidation of methane, such heat can be provided by the combustion of some methane.

Correlations between the thermodynamics of graphitic carbon deposition and operating conditions for gas mixtures ($CH_4$, $CO_2$, $H_2$, and $H_2O$) have been studied and reported[5, 6],

suggesting that carbon formation during DRM (but with $CO_2/CH_4$ ratios far above unity) is unfavorable even at ~700°C. However, working at lower temperatures with $CO_2/CH_4$ ratios close to unity might be preferred from an industrial point of view.[7] Rostrup-Nielsen et al.[8] reported that the amount of carbon deposited on a noble metal catalyst is less than that of nickel at 500°C (by an order of magnitude) and 650°C (slightly). Therefore, the noble metal catalysts show higher selectivities than supported nickel.[2] However, many researchers have also investigated DRM over Ni- and Co- supported catalysts due to the high costs and limited availability of the noble metals.[9-14] Although supported Ni catalysts are inexpensive and can show high catalytic activity for DRM, carbon deposition on the Ni catalysts is a crucial problem that needs to be solved.

Side reactions, CO disproportionation (the Boudouard reaction) and methane decomposition, occur during the reforming process and generate the carbon deposits.[1, 2] CO disproportionation is exothermic, which means the equilibrium constant decreases as temperature increases. Conversely, $CH_4$ decomposition is an endothermic process. The work of Reitmeier et al. shows that for any reaction mixture of $H_2$, CO, $H_2O$, $CO_2$, and $CH_4$ at thermodynamic equilibrium, the amount of graphitic carbon deposits decreases when reaction temperatures are higher.[6] This indicates that carbon deposition is mainly attributed to CO disproportionation.[1] The carbon formation will eventually deactivate the catalysts and block the reactor. One way to inhibit the carbon deposition might be to control the size of the ensembles of metal atoms on the surface, since carbon formation needs presumably larger ensembles compared with $CH_4$ reforming.[2, 15, 16] Therefore, carbon formation is a structure sensitive reaction.[17] Based on the carbon Auger Electron Spectroscopy results, there is no carbon deposited on Ni(111) at 250 and 345°C and ~$1.32\times10^{-5}$ atm, however, for the Ni(100) and Ni(110), the reaction does take place.

In this case, Ni(111) surface is less active in the decomposition of $CH_4$ to carbon than Ni(100) and Ni(110) surfaces.[18]

In addition, carbon formation can also be inhibited by choosing the proper support or promoters. For instance, Wang et al. showed that $La_2O_3$ and $CeO_2$ have positive effects on both catalytic activity and carbon suppression when present in Ni/$\gamma$-$Al_2O_3$.[19, 20] Laosiripojana et al. also showed that a $CeO_2$-$ZrO_2$ support suppresses carbon deposition in methane steam reforming at 650-900°C due to reactions with lattice oxygens at the surface; however, slightly deactivation due to sintering was found at high temperatures.[21]

Another big challenge for DRM is the presence of sulfur compounds in natural gas and biogas. These compounds are usually in the form of mercaptans, hydrogen sulfide and tetrahydrothiophene.[22] The sulfur can inhibit hydrocarbon reforming reactions on supported metal catalysts, especially Ni-based catalysts.[23-25] It will bond to the active sites reaching an equilibrium surface coverage that may deactivate the catalyst completely. The same also occurs with alumina-supported Rh, normally thought to be more sulfur-resistant.[26] The removal of $H_2S$ from natural gas by adsorption or absorption is called "sweetening", however, the sweetening process is quite impractical for low sulfur levels at high temperature, and especially when sulfur is also present in the $CO_2$ (e.g., $CO_2$ from biogas).

### 1.2. Research on the Mechanism

A kinetically significant and important step in DRM is the adsorption and dissociation of $CH_4$.[27] The mechanism for dissociation of $CH_4$ on a transition metal surface has been reported to be both direct and precursor mediated.[1] The latter pathway means formation of an intermediate, like the $CH_x$ or a formyl group with the oxygen coming from the support or from the oxidant (such as $CO_2$ in DRM).[27] Seets et al. found that the mechanism of $CH_4$ dissociation over Ir(110)

is related to temperature. At low temperature, the dissociation is dominated by a precursor-mediated mechanism. When the temperature increases, it gradually shifts to a direct dissociative mechanism.[28] Bitter et al. proposed that during DRM $CH_4$ is activated on the more reduced metal while $CO_2$ is activated on the support.[29] The $CO_2$ is activated and reduced to CO, which reaction provides surface oxygen to oxidize surface carbons generated from $CH_4$ decomposition.

It is wildly recognized that $CO_2$ chemisorption and dissociation on the surface of transition metal is controlled by electron transfer to form an anionic $CO_2^-$ precursor, and that the activation of $CO_2$ is structure sensitive.[30, 31] Activation of $CO_2$ can also occur on a support (except for inert materials like $SiO_2$) or even at the metal-support interface.[13, 15, 29] IR spectroscopy of $CO_2$ adsorption on the Pt-$ZrO_2$ indicates that the formation of carbonates and CO can take place on the support, or possibly the interface between support and Pt.[15] Van Keulen et al. noticed that conversion of $CO_2$ was greater for Pt/$ZrO_2$ than for Pt/$Al_2O_3$, for the same wt% of Pt. They suggested that $CO_2$ activation could be explained as the results of the greater basicity of the $ZrO_2$ support and the presence of more oxygen vacancies.[32] It has been reported that oxycarbonates were detected in DRM with both Ru and Ni catalysts supported on $La_2O_3$.[33] However, oxycarbonates are seldom detected when using alumina-based catalysts.[13] Mark et al. observed that $Al_2O_3$ does not activate $CO_2$, over Ru/$Al_2O_3$, and the lack of surface $CO_2$ will finally lead more coke formation.[34]

Various kinds of catalysts have been studied for DRM, in which case different mechanistic steps have been reported in the literature depending on the temperature and partial pressure range used.[27] A dual-site Langmuir-Hinshelwood mechanism has been proposed for DRM on Co-Ni/$Al_2O_3$ and Ce-Co-Ni/$Al_2O_3$ catalysts:[12]

$$CH_4 + 2X_1 \leftrightarrow CH_3\text{-}X_1 + H\text{-}X_1 \quad (1)$$

$$CH_3\text{-}X_1 + X_1 \leftrightarrow CH_y\text{-}X_1 + H\text{-}X_1 \quad 1 \leq y \leq 3 \tag{2}$$

$$\vdots$$

$$CH\text{-}X_1 + X_1 \leftrightarrow C\text{-}X_1 + H\text{-}X_1 \tag{3}$$

$$CO_2 + 2X_2 \leftrightarrow CO\text{-}X_2 + O\text{-}X_2 \tag{4}$$

$$C\text{-}X_1 + O\text{-}X_2 \rightarrow CO\text{-}X_2 + X_1 \tag{5}$$

$$2H\text{-}X_1 \leftrightarrow H_2 + 2X_1 \tag{6}$$

$$CO\text{-}X_2 \leftrightarrow CO + X_2 \tag{7}$$

$$H\text{-}X_1 + O\text{-}X_2 \rightarrow OH\text{-}X_2 + X_1 \tag{8}$$

$$H\text{-}X_1 + OH\text{-}X_2 \leftrightarrow H_2O + X_1 + X_2 \tag{9}$$

where $X_1$ and $X_2$ are both metal sites – $X_1$ more reducible and $X_2$ more oxophilic - and it was concluded that Step (5) is a rate-limiting step on the basis of pulse reactor experiments. Experimental data also show that DRM over Fe-Ni catalysts may follow a similar Mars-van Krevelen mechanism at 750°C, meaning that $CO_2$ oxidizes Fe to $FeO_x$, $CH_4$ is activated on Ni sites to form $H_2$ and surface carbon, and then surface carbon is reoxidized by the lattice oxygen from $FeO_x$, to CO.[11]

The activation energies for DRM over different catalysts have been reported and in all cases, the energy for the initial activation of $CH_4$ is 6.7-14 kJ/mol greater than the initial activation of $CO_2$,[27] so methane activation could also be a rate-limiting step.[35] Nandini et al. proposed a slightly different mechanism than steps (1)-(9) above, and hypothesized that $CH_4$ activation and $CH_xO^*$ decomposition were likely rate-limiting steps over a Ni-K/$CeO_2$-$Al_2O_3$ catalyst because the apparent $\Delta E$ of $H_2$ formation is greater than that of CO.[10, 36, 37] Isotopic experiments with a Rh/$Al_2O_3$ catalyst showed that its rate-limiting step in DRM involves the

breakage of a C-H(D) bond with an isotope effect around 1.5.[38] Since both the methane activation and $CH_xO$* decomposition involve C-H bond breakage, either or both of them could be rate-limiting steps for $Rh/Al_2O_3$ catalyst as well. From these studies, we can conclude that different catalysts can result in different rate-limiting steps (either step (5) above or $CH_4$ activation or $CH_xO$ decomposition).

### 1.3. Electronic Structure of REOs and REO Mixtures

The answer to the question of how we can describe the chemical bond between a surface and a molecule is of crucial importance in understanding surface chemical reactivity and catalysis. Several common properties that can be easily measured or estimated ("descriptors") can be used as surrogates for a complete description of the bonding. In this section, I discuss some common descriptors relevant to reforming catalysis.

The d-band model[39, 40],which describes the relationship between the valence states of an adsorbate and the *s* and *d* states of the transition metal surface, has been shown quite useful when it comes to rationalizing bond formation and trends in reactivity among transition metals.[41] For a clean metal surface, the energy of the d-band can be changed by filling antibonding states relative to the Fermi level.[41, 42] Due to the fact that the antibonding states are always higher in energy than the normally filled *d* states, the energy of the center of the *d* states relative to the Fermi level can be used to describe the bond strength.[41] Nørskov et al. show that the barrier for the activation of methane can be linearly related to the DFT-calculated Ni surface d-band center.[43] Liu et al. examined the d-band centers of a clean Ni surface and an ordered NiCo(111) alloy by DFT and related the differences to different rates of adsorption of $CH_X$.[44] Ruban et al. calculated the shifts in d-band centers due to surface impurities (Ag atoms) and Ag overlayers relative to a clean Ni surface, which are -0.53 eV and -1.14 eV, respectively.[45] In order to

identify a descriptor of catalytic activity for REOs and REO mixtures, recall that both the metal and oxygen centers contribute to the performance of the catalysts. A simple descriptor that includes both these two centers is the ligand-to-metal charge transfer (LMCT) excitation energy. In general, LMCT excitation energy is related to the band-gap energy, when it comes to metal oxides containing transition-metal centers in their highest oxidation states[46] Therefore, the band-gap energy is likely to be an activity descriptor for transition metal-doped REOs and REO mixtures. Khan et al. report that narrowing the band gap of $CeO_2$ nanostructures by electron beam irradiation can enhance their visible light activity.[47] The narrowing of the band gap might be due to the formation of some localized band gap states which arise from the structure of oxygen vacancy defects.[47, 48]

A universal electronic structure model for lanthanide materials is available.[49] This model is originally derived from experimental data on 4f and 5d energies of Ln ions as impurities in luminescent materials, however, it can be applied to stoichiometric Ln material as well. According to experimental data on Ln-doped materials, the variation over the Ln series (La, Ce, Pr,…, Lu) in energy difference between 4f and 5d state is not correlated to the type of Ln material and Ln valence state, and the variation in Ln 4f binding energy always shows a characteristic double-seated (two maxima, $Gd^{3+}$ and $Lu^{3+}$, two minima, $Ce^{3+}$ and $Tb^{3+}$) shape. However, the variation of 5d binding energies are quite different from 4f; the 5d binding energies are approximately constant. In this case, the energies of 4f ground state at the minima will be highest and result in the highest electrical conductivities. This model has been successfully validated by predicting basic material properties like semiconducting or metallic behavior, nature and magnitude of band gap energies and chemical stability[49] for well-studied materials such as LnS, LnO, $Ln_2O_3$ and $LnO_2$.

### 1.4. Other Key Descriptors of Activity of REOs and REO Mixtures

After cerium dioxide was first used as an oxygen storage component in car converters by Ford Motor Company, it became a promising constituent in catalytic systems for a wide range of applications, such as fuel cells, photocatalysis, the water-gas shift reaction, thermochemical water splitting, some reactions of organic compounds (e.g., condensations) and reforming processes.[50] The main reason $CeO_2$ is a common catalyst or part of a catalyst is its oxygen storage capacity (OSC), which allows it to release and store oxygen under different conditions, over a wide range of temperatures.[51] Yao and Yao[52] first studied the transient (pulse) oxidation of CO by ceria at 300-500°C, and cited $CeO_2$ as a suitable oxygen storage component for the three-way automotive catalyst. The OSC values of ceria strongly depend on the surface area, which can be determined by particle size, thermal or chemical pretreatment, and synthetic procedure.[50] Normally, the OSC of ceria can be improved by incorporation of Zr,[53-55] or other additives, such as Ni, Cu, Pt and Pd.[51, 56]

DFT can provide an explanation for the large OSC. Scanlon et al. report that the increased OSC of Pd- and Pt-doped $CeO_2$ arises from a large displacement of the dopant ions from the normal Ce lattice sites.[51] Pd(II) or Pt(II) moves by ~1.2 Å to adopt a square-planar coordination because of the crystal field effects. Therefore, one of three tri-coordinated oxygen atoms adjacent to the square planar structure becomes easier to remove, leading to increased OSC.[51]

Senftle et al. investigated methane activation on $Pd_xCe_{1-x}O_\delta$, and demonstrated that the rapid C-H activation can be attributed to the doped Pd, a $Pd^{4+} \leftrightarrow Pd^{2+}$ transition.[57] Cen et al.[58] reported that Mn doping could also make the $CeO_2$ (111) surface much more reducible (more O-vacancies can be formed) based on DFT. Mn doping introduces a Mn 3d–O 2p gap state as an

electron donor and acceptor, which lowers the formation energy of the first and second O-vacancies ($\Delta E_v$) by 2.54 eV and 0.68 eV, respectively, relative to $\Delta E_v$ of a clean $CeO_2$ (111) surface.[58] Krcha et al. also calculated $\Delta E_v$'s for surfaces of pure and sulfided, La, Tb and Mn-doped $CeO_2$(111) with the model in Figure 1.1, in which Mn doping lowers $\Delta E_v$ (first) by 1.66 and $\Delta E_v$ (second) by 1.58 eV relative to $\Delta E_v$ (first) and $\Delta E_v$ (second) of $CeO_2$ (111). But La or Tb doping has little effect on $\Delta E_v$'s. The calculations indicate that while the Mn dopant still leads to the fact that hydrocarbon species prefer to bind to surface oxygen rather than sulfur atoms, there is some potential to bind to sulfur, meaning such catalysts could exhibit sulfur tolerance.[59]

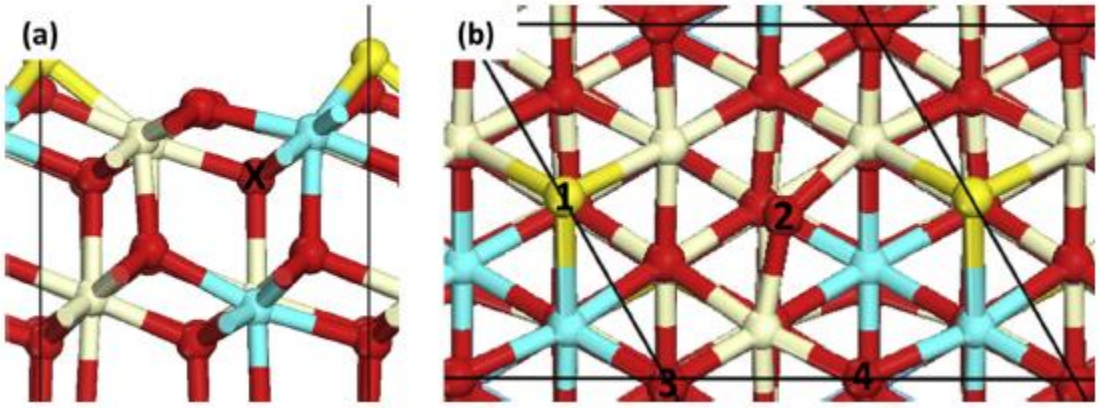


Figure 1.1. Top and side views of the p(2×2) unit cell expansion of sulfide M-doped $CeO_2$(111).(a) Side view, and (b) top view. The X is the position of the subsurface oxygen vacancy (X denotes an oxygen vacancy in front of the labeled oxygen). Ce is displayed as tan, M as light blue, O as red and S as yellow. This figure was adapted from Krcha et al. [59] with permission.

Base transition metal, noble metal and rare earth elements doped into ceria can lower $\Delta E_v$'s. Pd doping lowers the surface $\Delta E_v$ of $CeO_2$ by 2.4 eV (DFT calculation).[60] $\Delta E_v$ can be lowered even further upon doping Zr into $CeO_2$ with 50% Zr (Ce:Zr = 1:1) giving the lowest $\Delta E_v$ (DFT calculation),[61]consistent with results that $Ce_xZr_{1-x}O_2$ compositions of $0.5<x<0.8$ give the

highest OSCs.[62-65] Unlike isovalent nonreducible dopants ($Zr^{4+}$), which affect $\Delta E_v$ due to a size effect on the relaxation energy, trivalent cations ($La^{3+}$) change $\Delta E_v$'s by creating O•− radicals that are easier to remove (DFT predictions).[66]

Another descriptor that can be used to describe the activity of REOs and REO mixture is the ionic radius of the RE dopant. Kim et al. point out that the energy barrier of the rate-limiting step for CO oxidation with RE-doped $CeO_2$ (111) can be correlated with the dopant ionic radius, in which case it can predict the entire reaction activity.[67] Also, experimental results show that the activity of CO oxidation is as followed: $CeO_2$> Pr-doped $CeO_2$> Nd-doped $CeO_2$> Sm-doped $CeO_2$, which is consistent with the DFT calculation that there is a linear relationship between the ionic radius of the RE dopant and the activity represented by the energy barrier of the rate-limiting step.[67]

Surface reducibility might be treated as a descriptor for the activity of REOS and REO mixture as well. Kumar et al. investigated methane activation over a range of metal-oxide surfaces based on DFT calculation and reported that there is a linear relationship between activity, selectivity and surface reducibility for methane activation.[68]

When sulfur is present in a reforming feed, the ease of bulk sulfide formation of the catalyst (in the absence of other adsorbates) may be a suitable activity descriptor. Sulfur compounds, even at low concentration in the feed, can deactivate reforming catalysts.

Sulfur poisoning leads to bulk sulfidation.[69] For a zero-valent metal (Me), the process is (for the common sulfur poison $H_2S$):[70]

$$\mathrm{Me} + \mathrm{H_2S} \rightarrow \mathrm{MeS} + \mathrm{H_2}$$

At high temperature, poisoning decreases because sulfidation is thermodynamically unfavored. But the Gibbs free energy of the sulfidation reaction of Ni is negative even at 1000°C.

Sulfur can also cause catalyst deactivation in other ways, such as electronically modifying neighbor atoms' ability to adsorb or dissociate reactant molecules, or reconstructing the catalyst surface to an inactive state.[70]

Sulfur, when adsorbed on large Ni crystallites (on $Al_2O_3$ or $MgAl_2O_4$), can inhibit bimolecular coking more than reforming if: (a) the S coverage is near-monolayer; (b) temperature is high (>800°C); (c) the pressure of CO is relatively low.[71] In other words, the ensemble size of the reforming reaction with terraced Ni under these conditions is smaller than that of carbon nucleation from a hydrocarbon source. But this simple formulation seemingly fails for the more complex catalysts characteristic of modern reforming practice. A number of studies have suggested that certain oxide additives ($WO_3$, Re, REOs) can provide some coking resistance in the presence of sulfur, though the mechanistic source of this enhancement is unclear.[72-78]

On the other hand, $Ni/Ca_{12}Al_{14}O_{33}$, which is active at 800°C for toluene reforming, with almost no carbon deposition,[79] loses activity rapidly with 500 ppm $H_2S$ present. Air regeneration cannot recover the lost activity, suggesting it is due to more than just sulfur adsorption. Enhanced coking (observed indirectly through the $H_2$ production rate) was also observed for Ni-$Mo/Al_2O_3$ with 5 ppm $H_2S$ at 580°C,[80] and $Ni/Sr/Al_2O_3$ with 10 ppm organic sulfur at 800°C.[77] Base metals in the reduced state undergo a modest increase in coking rate in the presence of $H_2S$, e.g., Fe/Ni or Fe at ~827°C,[81, 82] with the metals on the surface also being converted to a variety of sulfide phases.[83]

From this small data set, one might conclude that some additives to Ni-based catalysts (e.g., $WO_3$, Re, rare earth oxides) may provide coking resistance in the presence of sulfur. But temperature, steam/carbon ratio and the partial pressure of the sulfur in the feed undoubtedly also

influence how adsorbed sulfur can affect coking rates. The potential positive effects on coking rate complicate any strategy to employ bulk sulfide formation thermodynamics as a reforming activity descriptor by itself.

# CHAPTER 2. RAPID SCREENING OF TERNARY RARE-EARTH – TRANSITION METAL CATALYSTS FOR DRY REFORMING OF METHANE AND CHARACTERIZATION OF FINAL STRUCTURES[1]

## 2.1. Introduction

Carbon dioxide or "dry" reforming of methane (DRM) produces synthesis gas from carbon dioxide and methane: $CH_4 + CO_2 \rightarrow 2H_2 + 2CO$. Compared with methane steam reforming, dry reforming has the advantage of utilizing the $CO_2$ greenhouse gas and producing a lower $H_2$:CO ratio, which can be advantageous in increasing selectivity to longer chain, diesel-range hydrocarbons in downstream Fisher Tropsch processes.[1, 2, 84] In this way, two types of greenhouse gases are consumed and transformed into a useful industrial gas stream.

DRM is a highly endothermic reaction, with an operating temperature range usually between 650-850°C, and with a wide GHSV range (2.9-230 L/(gcat•h)), and pressures of 1-10 atm. The $CH_4/CO_2$ feed ratio is usually one. Excess $CH_4$ can lead to more carbon formation via methane decomposition and block the reactor. A higher CO yield can be achieved by decreasing reaction. Catalysts include both supported noble metals, but also those based on group 7-11 base transition metals (TMs). However, Ni-based catalysts are considered the most promising candidates for further development due to their high activity, low cost and the abundance of the metal.[9-14, 21, 85-89] A major problem for any of these catalysts is deactivation due to CO disproportionation and $CH_4$ decomposition, and the sintering of metal particles at high temperature.[1, 2, 90] One way proposed to inhibit carbon deposition is to reduce the dispersion of

[1] This chapter previously appeared as Jiang, C.; Akkullu, M. R.; Li, B.; Davila, J. C.; Janik, M. J.; Dooley, K. M., Rapid Screening of Ternary Rare-earth – Transition Metal Catalysts for Dry Reforming of Methane and Characterization of Final Structures. *Journal of Catalysis* **2019,** *377*, 332-342. It is reprinted by permission of Copyright (2019) Elsevier Inc. DFT work was completed by Li, B and Janik, M.J. at Pennsylvania State University.

metal atoms on the surface, because the ensembles necessary for carbon formation are presumably smaller than those needed for removal of hydrogen from $CH_4$.[2, 15-17] But conversely it is also thought, based upon experience, that highly defective small metal crystallites make more stable DRM catalysts.[14, 43, 86, 87, 91-95] Therefore carbon formation might also be inhibited by choosing the proper oxide or second-metal promoters to interact with Ni, but the many possible combinations of these can make testing laborious.

Both $La_2O_3$ and $CeO_2$ have positive effects on catalytic activity and carbon suppression when present in, for example, Ni/$\gamma$-$Al_2O_3$.[12, 19, 20, 86, 93] Oxygen vacancies in $CeO_2$, $ZrO_2$ and other oxides activate $CO_2$ under DRM conditions,[32, 96-99] and facilitate oxidation of nascent coke.[21, 86, 93, 99-101] For $CeO_2$-oxide mixtures, a high oxygen storage capacity (OSC) arises from high vacancy concentrations and persists over a wide temperature range.[51, 102] The 3/1 Ce/La ratio is known to lead to even higher vacancy concentrations under reducing conditions. An alternative to 3/1 Ce/La with similarly high oxygen vacancy concentrations is the Ce/Zr system, especially in the 1/1 to 3/1 range.[14, 62, 65, 103-106] Its OSC is also greater than pure ceria,[53-55, 102] and Ce/Zr in this range suppresses carbon deposition in $CH_4$ steam reforming and DRM.[14, 21, 94, 107]

Both $La^{3+}$ and $Zr^{4+}$ dopants improve the thermal stability of ceria and its ability to incorporate TMs through creation of more defects. They also enhance the dispersion of, for example, Ni in the $CeO_2$, driving more Ni to the surface.[90, 107-109] Therefore in this work we have based our DRM catalysts on binary oxides containing $CeO_2$ and either $La_2O_3$ or $ZrO_2$, both of these with a series of TMs as active components.

In order to shorten the testing timeline and detect coking over shorter periods, we have developed a rapid online method to measure reforming and coking rates simultaneously without chromatography. This method allows us to rapidly screen many ternary mixed oxide

compositions (Ce - La/Zr – late TM), and then decide which compositions merit further examination in a more conventional fixed-bed reactor system, where long-term deactivation can be assessed. Integrated experimental and computational efforts provide a mechanistic rationale for designing more stable, coke-tolerant catalysts. Density functional theory (DFT) methods were used to identify likely vacancy locations and concentrations, examine C-H and C-C bond activation over the Ce-La oxide surface, and assess the tendency of TMs to reduce and segregate to the surface.

Further catalyst characterizations by XANES, XPS, CO chemisorption, BET surface area, Raman spectroscopy and XRD allow us to examine the modifications to the surfaces upon use in the longer term experiments.

## 2.2. Materials and Methods

### 2.2.1. Preparation of Catalysts

Ce/La mixed oxides were prepared by a templated sol-gel method adapted from previous work.[54, 110-112] The precursors $(NH_4)_2Ce(NO_3)_6$ (98+%, Alfa) and $La(NO_3)\bullet 6H_2O$ (99.9%, Alfa) were dissolved in 96% water/3% methanol/1% TMAOH surfactant (25% in methanol). The molar ratio Ce/La was 3:1, with a 1/100 wt ratio of the oxides in the sol-gel synthesis mixture. Ammonia solution was added to gradually bring the pH to 10.3 during aging (90°C, 2 d). After centrifugation and washings with deionized water and acetone, the mixed oxide was dried at 120°C overnight and calcined at 500°C in air for 6 h.

The Ce/La oxide was modified with Ni and/or Co by deposition–precipitation from 0.3 M urea for 24 h at 90°C. The precursors were $Ni(NO_3)_2\bullet 6H_2O$ (Aldrich, reagent) and/or $Co(NO_3)_2\bullet 6H_2O$ (J.T. Baker, reagent). Centrifugation, washing and drying were the same as above. These catalysts were typically reduced in 5% $H_2/N_2$ at 750°C for 6 h prior to use.

Mixed Ce/Zr oxides of molar ratios from 1:1 to 3:1 were prepared similarly to Ce3/La, except for the final pH (10.5). The Zr source was $Zr(NO_3)_4 \bullet H_2O$ (Aldrich, 99%). Mixed Fe/Ce, Co/Ce and Mn/Ce oxides were made similarly, but to final pH 10-10.2. Ni and/or Co addition to Ce/Zr oxides was by deposition-precipitation as described above. These catalysts were typically reduced in 5% $H_2/N_2$ mixture at 750°C for 6 h prior to use. Other metals were added to Ce3/La or the Ce/Zr oxides as follows. Fe (from 95% $FeCl_3$, Fisher) or Mn (from 52% aqueous $Mn(NO_3)_2$, J.T. Baker) were impregnated onto the support using incipient wetness. Pd (from $PdCl_2$, Pressure Chemical) was deposited from a 15 mmol solution with pH adjusted to 10 using $Na_2CO_3$. Ru (from $RuCl_3 \bullet H_2O$, Aldrich) was deposited from a solution containing a 5 molar excess of hydrazine hydrate. Workup, drying and calcination were as described previously.

**2.2.2. Dry Reforming of Methane**

The rapid online coking / reforming rate measurement method at differential conditions made use of a modified DSC/TGA (TA SDT Q600). We made up a cylinder of 33 vol% $CO_2$/balance $N_2$, and adapted the DSC/TGA controllers to handle a 1:1 $CO_2/CH_4$ feed typical of DRM, at 0.25 atm partial pressure of each reactant, 133 mL/min total, 750°C. Initial adsorption effects ended in less than 1 h and the DSC heat flow came to a constant endothermic value that can be mathematically related to the rate of the reforming reaction. Any coking reaction occurring would result in a constant slope weight gain, which can be mathematically related to the rate of the coking. Runs of 180 min were usually sufficient to measure both rates.

Based on the DSC/TGA experiments, promising materials were tested for longer times in fixed-bed reactors. In these experiments, the reactant partial pressures were higher (~0.65 atm of each species), and 250-500 mg catalyst typically used. Further details are in the Appendix C.

### 2.2.3. Characterization of Catalysts

The BET surface areas of the dried (300°C) catalysts were measured by $N_2$ adsorption (3 points) using a Quantachrome AS-1 porosimeter. CO chemisorption at 25°C was evaluated by the pulse technique using a Micromeritics 2700 apparatus. Elemental compositions of selected as-synthesized catalysts were determined by ICP-AES (Perkin Elmer Optima 8000). Samples were initially dissolved in a 3:2 mixture of hydrochloric acid (36.5-38%) and nitric acid (68-70%). Temperature-programmed reductions (TPR) and oxidations (TPO) took place in the DSC/TGA. For the reductions, the heat effect allows discrimination of a weight loss due to reduction (exothermic for the TM oxides) from one due to desorption (endothermic). The reduction ramp rate in 25% $H_2/N_2$ was 5°C/min, to 800°C. The oxidation ramp rate in air was 10C/min to 650°C, with a 60 min final hold.

XRD measurements (40 mA, 45 kV) employed a PANalytical Empyrean diffractometer with Cu Kα radiation. Spectra were recorded at 0.02° steps in the range $5° < 2\theta < 125°$. Raman spectra were recorded on a Renishaw inVia Raman microscope using the 532 nm laser, 1/1800 grating, at room temperature. The exposure time was 0.1 s with 100 accumulated spectra, which was found to minimize the fluorescence.

X-ray photoelectron (XPS) spectra were collected on a Scienta Omicron ESCA 2SR with a 128-channel detector. The C1s line (284.8 eV) was used to calibrate the binding energies. After Shirley background subtraction and with Gaussian-Lorentzian line-shapes applied, the spectra were deconvoluted using CasaXPS version 2.3.19.

X-ray absorption near-edge spectroscopy (XANES) was performed at the LSU Center for Advanced Microstructures and Devices (CAMD) HEXAS beamline, using a Ge 220 double crystal monochromator. The Ni K edge spectra were collected at room temperature in

fluorescence mode with a Ni foil calibration standard. Data were processed (background subtraction, deglitching, merging of 9 spectra) using Athena 0.8.061..[113]

### 2.2.4. Density Functional Theory Methods

Electronic structure calculations were performed using the Vienna ab initio simulation program (VASP).[114-116] A plane wave basis set was used to represent the valence electrons with a cutoff energy of 450 eV. The core region was represented using the projector augmented wave (PAW) method.[117] The valence configurations were $3d^8 4s^2$ for Ni, $5s^2 5p^6 6s^2 4f^1 5d^1$ for Ce, $4d^2 5s^2$ for Zr, and $2s^2 2p^4$ for O. All calculations were spin polarized. The exchange and correlation energies were represented using the Perdew, Burke and Ernzerhof (PBE) version of the generalized gradient approximation (GGA).[118] The Monkhorst Pack k-point sampling scheme was utilized with a (2 x 2 x 2) grid for the bulk $M_{32}O_{64}$ structure, and a (3 x 3 x 1) grid for the $M_{20}O_{40}$ (111) model. Structural optimizations were performed by minimizing the forces on all atoms below 0.05 $eV \bullet Å^{-1}$.

Considering the well-established difficulties within DFT to accurately represent the nature of localized d and f states,[119-121] we implemented the DFT+U approach which introduces the Hubbard U-term as an on-site Coulombic interaction term in the f states of cerium and d states of Ni.[122, 123] This U correction results in greater electron localization in these states when $CeO_2$ is reduced. The oxygen vacancy formation energies are closely related to the value of U chosen for the f-states of $CeO_2$ when Ce atoms are reduced. We used a U-value of 5 eV on the f-orbitals of cerium which is consistent with previous DFT studies of ceria.[59, 124-131] The U-value of 5 eV provides an accurate description of the electronic structure of reduced ceria. However, the empirical U value may introduce a possible error in all results which would be difficult to quantitatively estimate. We applied a U value of 5.3 eV on the d-states of Ni.[132] No U correction

was used for Zr d-states, as Zr is not observed to change oxidation state upon oxygen vacancy formation in the $Zr_xCe_{1-x}O_2$ structures.

## 2.3. Results

### 2.3.1. TGA/DSC Screening Experiments

The results of rapid screening experiments for DRM and coking rates are shown in Table 2.1, with selected results for Ni-containing catalysts in Figure 2.1. Catalysts are typically designated by their molar ratios. These were the ratios of the syntheses, but several catalysts were also analyzed by ICP-AES and the ICP molar ratios were within 10% of the nominal values in all cases. Analysis of the TGA/DSC results is as follows. Catalysts with little to no adsorption (exothermic) heat effect and/or weight gain are inactive. Catalysts with a significant, sustained exotherm and a large weight gain are coking rapidly. Those showing an early (<10 min) exotherm, but a later endotherm, and also showing initial weight gains followed by slow (or no) weight changes, are catalysts meriting further examination, because their reforming/coking rate ratios are high. The slopes of the TGA curves were roughly constant after 1 h (Figure 2.1), suggesting a constant rate of coking that is included in Table 2.1.

In Table 2.1, some of the coking rates are slightly negative, which suggests that some further oxide reduction might still be taking place, or that some material adsorbed at short times is slowly being desorbed due to changes in catalyst structure. For some materials, it may take several hours to complete the mixing process for the late TM with the REO matrix. For Ni-, Co-, Pd- and Ru-containing REOs, an initial reduction was found to be necessary in order to avoid a lengthy reduction during the rapid screening experiments that resulted in a lower rate of DRM at short times; this behavior was verified for a few materials by comparison experiments where they were treated with $N_2$ only (Table C.1). Reduction was unnecessary for Fe-, Mn- and non-

TM-containing catalysts, or for the one $Al_2O_3$-supported (benchmark) catalyst tested. Regardless of oxide mixing/reduction causing minor complications in interpreting the weight changes, we observed that any material exhibiting a negative weight gain in the first few hours won't coke in a flow reactor system over longer times. Coking is exothermic, reforming endothermic, so a negative or small positive heat flow (< 1 mw/mg) means there is no or almost no DRM reaction.

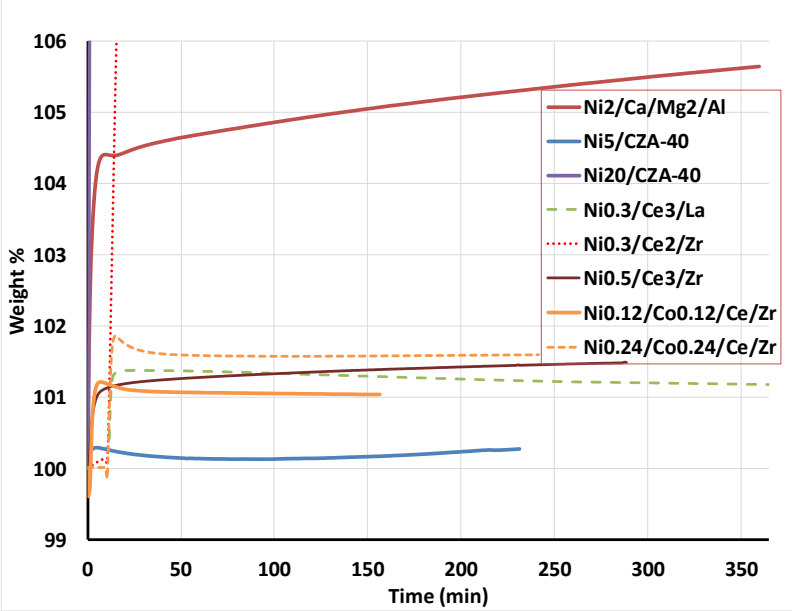


Figure 2.1. TGA coking experiments. Catalysts are pretreated with 25% $H_2/N_2$ at 750°C for at least 6 h, then fed 1:1 $CH_4$: $CO_2$ (0.25 atm apiece). For the catalysts using a commercial Ce-Zr-Al support (PIDC CZA-40), the numbers for Ni are wt%.

Table 2.1. Coking and reforming rates at >1 h calculated from DSC/TGA results. Samples pretreated with 25% $H_2/N_2$ at 750°C for at least 6 h, then fed 1:1 $CH_4:CO_2$ (0.25 atm each), except where noted.

| | Heat flow (mW/mg) | Coking Rate at >1 h (mg coke/(mg•h) | % $CH_4$ conversion | Reforming rate (mmol/mg• h) |
|---|---|---|---|---|
| Ni2/Ca/Mg2/Al[1,2] | 11.5 | 2.0E-3 | 4.9 | 0.16 |
| CZA-40[1,3] | 1.8 | -1.1E-4 | 0.56 | 0.024 |
| Ni5/CZA-40[3] (5 wt% Ni) | 21.1 | 2.4E-5 | 4.5 | 0.29 |
| Ni20/CZA-40[3] (20 wt% Ni) | 21.6 | 7.9E-2 | 5.8 | 0.30 |
| $CeO_2$[1] | 1.6 | -1.6E-4 | 0.66 | 0.023 |
| Fe/Ce3[1] | 0.50 | 1.0E-7 | 0.14 | 0.067 |
| Co/Ce5 | 6.7 | 6.4E-3 | 2.7 | 0.092 |
| Co/Ce9 | 2.4 | 2.0E-3 | 0.97 | 0.033 |
| Pd/Ce9 | 3.9 | 3.3E-2 | 1.6 | 0.054 |
| Ce3/La[1] | 0.094 | 4.7E-5 | 0.035 | 0.001 |
| Fe0.4/Ce3/La[1] | 1.2 | -2.6E-4 | 0.53 | 0.017 |
| Fe/Ce3/La[1] | 0.71 | 9.9E-4 | 0.59 | 0.010 |
| Pd0.4/Ce3/La | 5.7 | 0.36 | 2.7 | 0.079 |
| Ru0.2/Ce3/La | 7.3 | 5.1E-4 | 4.0 | 0.10 |
| Mn0.4/Ce3/La[1] | 1.8 | 4.7E-5 | 0.56 | 0.024 |
| Mn1.1/Ce3/La[1] | 1.9 | -2.3E-4 | 0.69 | 0.025 |
| Ni0.3/Ce3/La | 10.7 | -5.7E-4 | 4.1 | 0.15 |
| Ni0.6/Ce3/La | 7.9 | -5.7E-4 | 3.6 | 0.11 |
| Ni0.3/Co0.3/Ce3/La | 9.5 | -2.3E-4 | 3.9 | 0.13 |
| Ru0.1/Ce/Zr | 7.8 | 4.3E-4 | 3.9 | 0.11 |
| Mn0.2/Ce/Zr[1] | 0.88 | -2.8E-4 | 0.031 | 0.012 |
| Mn0.4/Ce/Zr[1] | 4.6 | 5.9E-5 | 2.5 | 0.064 |
| Ni0.1/Ce | 6.7 | 8.2E-5 | 3.2 | 0.12 |
| Ni0.12/Ce/Zr | 9.1 | 2.7E-4 | 3.9 | 0.13 |
| Ni0.2/Co0.2/Ce/Zr | 11.9 | -7.0E-5 | 3.7 | 0.16 |
| Ni0.24/Co0.24/Ce/Zr | 7.7 | 4.0E-5 | 3.2 | 0.11 |
| Ni0.15/Ce2/Zr | 9.1 | 8.0E-4 | 3.4 | 0.13 |
| Ni0.3/Ce2/Zr | 12.9 | 2.1E-2 | 5.6 | 0.18 |
| Ni0.15/Co0.15/Ce2/Zr | 8.5 | -3.5E-5 | 3.6 | 0.12 |
| Ce3/Zr[1] | 2.4 | -2.1E-6 | 0.68 | 0.032 |
| Co0.3/Ce3/Zr | 7.0 | 2.3E-4 | 2.8 | 0.096 |
| Pd0.27/Ce3/Zr | 6.2 | 0.42 | 2.6 | 0.086 |

(table cont'd)

| | Heat flow (mW/mg) | Coking Rate at >1 h (mg coke/(mg•h) | % $CH_4$ conversion | Reforming rate (mmol/mg• h) |
|---|---|---|---|---|
| Ru0.2/Ce3/Zr | 7.0 | 2.8E-3 | 4.3 | 0.096 |
| Mn0.82/Ce3/Zr[1] | 0.76 | 2.0E-4 | 0.58 | 0.010 |
| Ni0.5/Ce3/Zr | 9.2 | 5.5E-4 | 4.2 | 0.13 |
| Ni0.2/Co0.2/Ce3/Zr | 9.6 | 1.1E-4 | 3.5 | 0.13 |
| Ni0.3/Co0.3/Ce3/Zr | 9.8 | 1.4E-3 | 3.7 | 0.14 |

[1]Not reduced prior to experiment
[2]40 wt% $Al_2O_3$. The other numbers are molar ratios.
[3]A commercial (PIDC) $CeO_2/ZrO_2/La_2O_3/Y_2O_3/Al_2O_3$ 3-way catalyst support, 60 wt% $Al_2O_3$

Taking the DSC data at the endothermic plateau, we can estimate the fractional conversion of $CH_4$ and its rate of DRM. The following approximation was made: reforming reaction >> (sum of coking and reverse water-gas shift reactions). The fraction conversion equation is:

$$\text{Calculated heat flow} = \Delta H_R \times F_{in,CH4} \times X_{CH4}$$

where $\Delta H_R$ is the enthalpy change for DRM, and $F_{in,CH4}$ is the molar flow rate of the inlet $CH_4$. Calculations for $X_{CH4}$ and all thermodynamic calculations were performed in ASPEN-HYSYS®. The endothermic heat effect for DRM at 660-800°C is estimated as 7.2-7.5 times that of reverse water-gas shift (also endothermic), further justifying the approximations. Since the conversions are small, the differential approximation applies and the initial reforming rate ($r$) can be calculated as follows:

$$r = \frac{F_{in,CH4} \times X_{CH4}}{wt\ catalyst}$$

In Table 2.1, Ni2/Ca/Mg2/Al (a commercial high-temperature reforming catalyst formulation) is used as a benchmark. The reforming rates of the better REO-based catalysts are roughly equivalent on a weight basis, while the coking rates are typically smaller, often by more

than one order of magnitude. An optimal commercial REO support, such as CZA-40, loaded with Ni, gives a significantly higher reforming rate than that of the benchmark. Excessive Ni loading (e.g., Ni20/CZA-40) results in a catalyst with islands of Ni on the surface (it chemisorbs CO at RT), leading to rapid coking. Pd in $CeO_2$ or $CeO_2/La_2O_3$ are also rapidly coking catalysts, regardless of Pd composition.

Over a wide range of REO supports, the data in Table 2.1 shows an order of dopant metal activity of:

$$Ni > Ru > Co > Pd >> Mn > Fe$$

The position of Pd is somewhat indeterminate because its coking rates are high. Because the coking rates for some Ni-containing catalysts are low, while those for Ru-REOs are generally higher, we continued with mainly Ni and Ni-Co catalysts for analysis using fixed-bed reactors.

### 2.3.2. DRM in Fixed-bed Reactors

Promising catalysts based on the results of the DSC/TGA experiments were also tested in a conventional fixed bed reactor with 1:1 $CH_4$:$CO_2$ feed. The differences between these experiments are as follows. In the DSC/TGA experiments, the partial pressures and conversions are low, so the catalysts see mostly $CH_4$, $CO_2$ and $N_2$. The GHSVs are too high to give conversions above a few percent. However, for the fixed-bed experiments, the reactant partial pressures are ~0.65 atm each for $CH_4$ and $CO_2$, and the conversion can be >40% for active catalysts. The catalysts are exposed to more CO, $H_2$ and water, over a several (1-10) day period, depending on the catalyst. Finally, the fixed-bed experiments provided enough sample to do structural characterization of the spent catalysts.

Three equations are employed to represent the main reactions (DRM, water-gas shift, and coking) as follows, in closing a mass balance:

$$CO_2 + CH_4 \leftrightarrow 2H_2 + 2CO \qquad \xi_1$$
$$CO_2 + H_2 \leftrightarrow CO + H_2O \qquad \xi_2$$
$$H_2O + C \leftrightarrow H_2 + CO \qquad \xi_3$$

The ξ's are the molar extents of reactions for these three reactions in mol/min, and they were calculated by solving the component mass balances simultaneously, using both the compositions and the effluent flow rate. The terms $F_{in,CH4}$ and $F_{in,CO2}$ are molar flowrates of feed components in mol/min. The yields of the products on an elemental carbon basis and the conversion of $CH_4$ and $CO_2$ are calculated as follows:

$$Y(CO) = \frac{2\xi_1 + \xi_2 + \xi_3}{F_{in,CO2} + F_{in,CH4}}$$
$$Y(C) = \frac{-\xi_3}{F_{in,CO2} + F_{in,CH4}}$$
$$X(CH_4) = \frac{\xi_1}{F_{in,CH4}}$$
$$X(CO_2) = \frac{\xi_1 + \xi_2}{F_{in,CO2}}$$

The catalyst activities in these high conversion experiments are reported as $CH_4$ conversion times GHSV (which equals the reforming reaction rate for a zero-order reaction, and approximates the average reforming rate otherwise). For the non-Ni-series, these activities are given in Figure 2.2(along with the benchmark catalyst), for the Ni-REO series in Figure 2.3, with the $H_2$/CO ratios of the latter in Figure 2.4. In agreement with the results of Table 2.1, the activities of Fe, Mn and non-TM-containing catalysts are low compared with both the Ni2/Ca/Mg2/Al benchmark and the Ni-REO catalysts. For Pd-REO catalysts, the DRM reactor experiments also agree with the coking seen in the DSC/TGA results. In the flow reactor, Pd0.3/Ce2/Zr lost most of its activity within 3 h. The other Pd catalyst tested (Pd/Ce9) had a much lower Pd content but still deactivated. As shown in Figure 2.5, the coking rates measured

by TGA are not a reliable guide to how much the catalysts deactivate at higher pressures and over longer times (except for the Pd-based catalysts, one of which is not even shown in Figure 2.5 because it deactivated in <12 h). The BET surface areas of Ni-based catalysts decreased by roughly 50-90% during these runs (Table C.2), but surprisingly the activities are not much affected and in some cases actually increase with time on stream. Some details of longer-term runs are given in Figure C.1; the Ni0.2/Co0.2/Ce/Zr catalysts was kept online another six days without further loss of activity

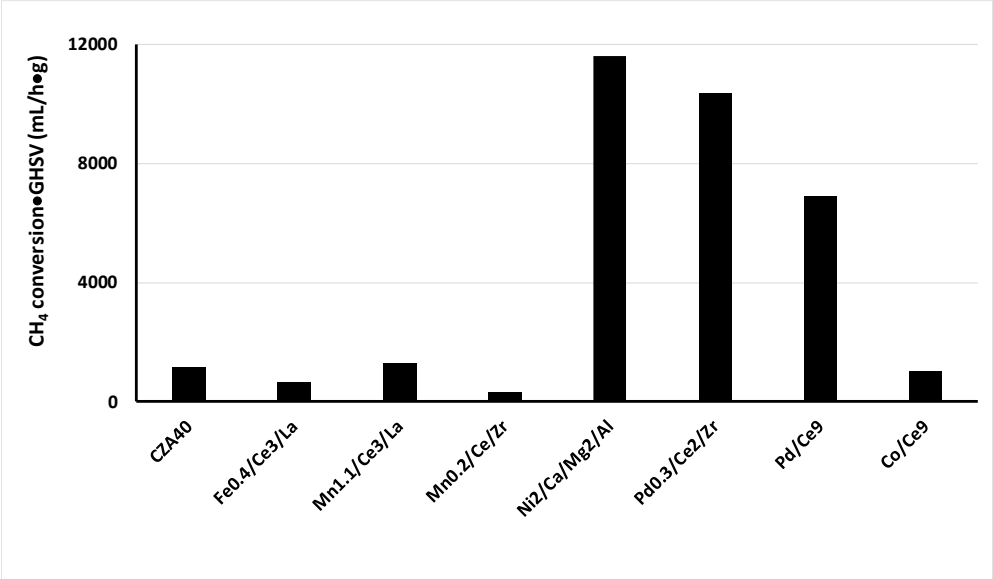


Figure 2.2. Catalyst activities at 750°C, 1.3 atm, minimum 12 h time onstream except for Pd-containing catalysts, which deactivated in shorter times.

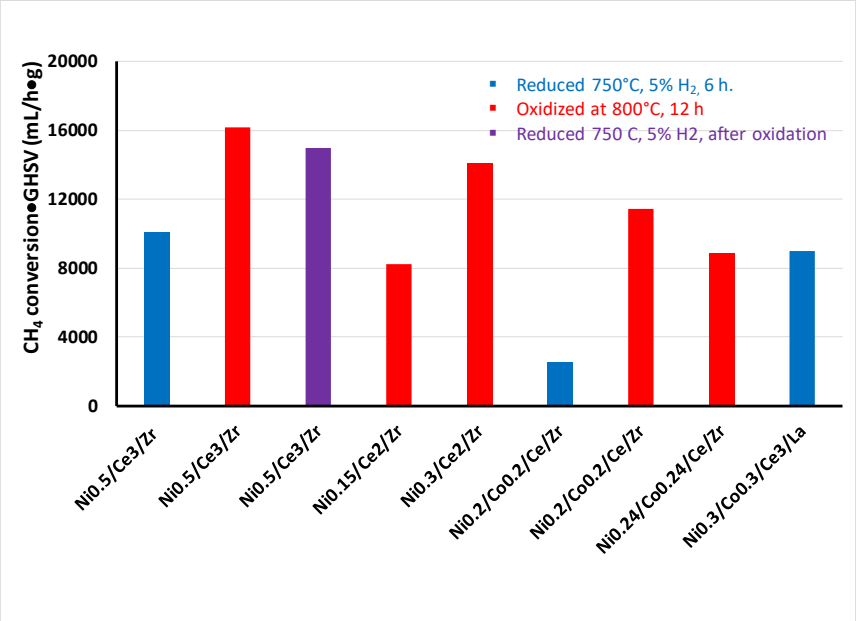


Figure 2.3. Catalyst activities at 750°C, 1.3 atm, minimum 12 h time onstream.

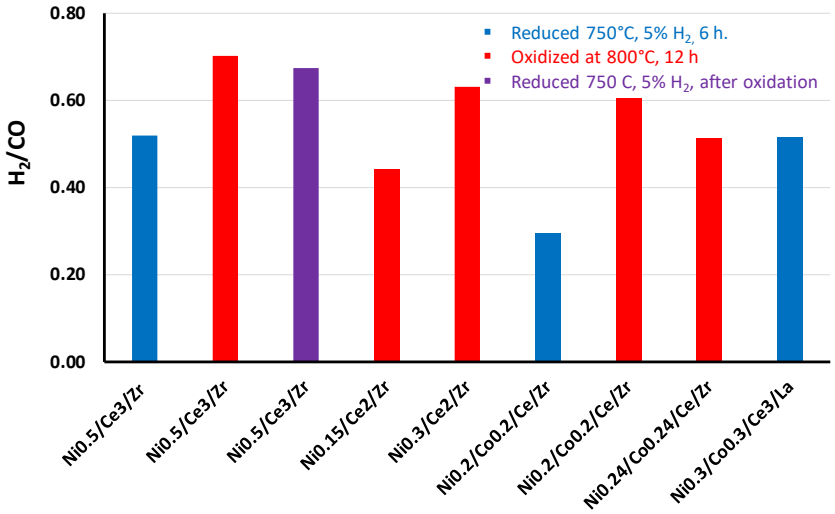


Figure 2.4. Product ratios at 750°C, 1.3 atm, minimum 12 h time onstream.

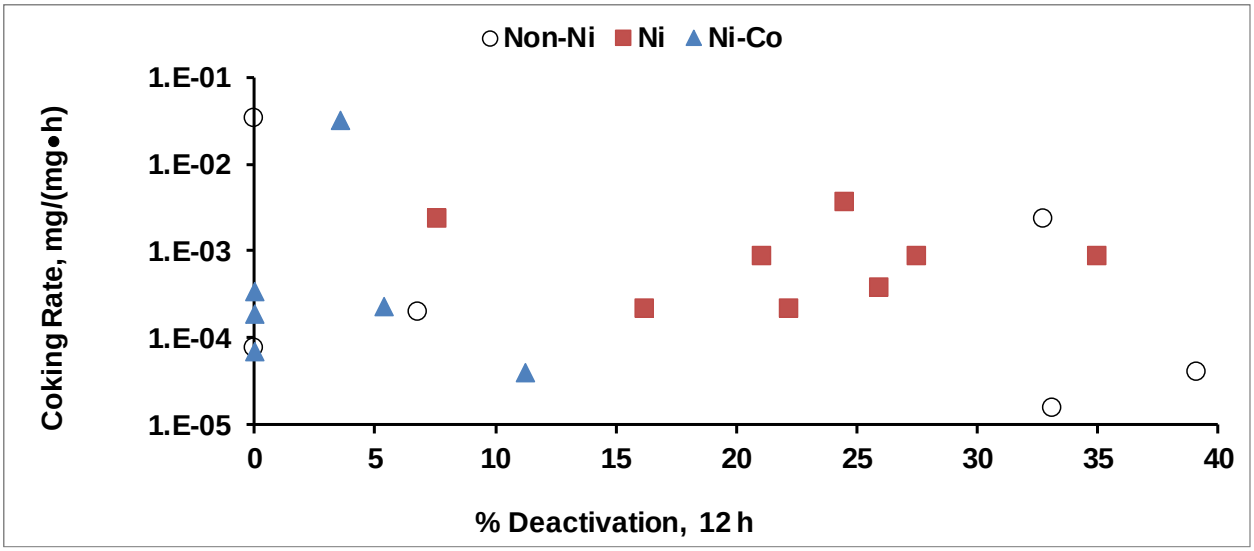

Figure 2.5. Comparison of coking rate from DSC/TGA experiments and % loss of DRM activity in a fixed bed reactor. A constant factor of 3E-4 was added to the Y-values to enable plotting on a log scale.

The catalyst Ni0.3/Co0.3/Ce3/La in Figure 2.2 and Figure C.1 showed little initial activity, but after ~3-4 h time onstream the activity increased. This led to a further exploration of pretreatments. We found that for Ni-containing catalysts an oxidation in air at 800°C (after the initial reduction) shortened the induction period and led to increased activities and $H_2$/CO ratios even at longer times onstream. Examples are shown in Figure 2.3, Figure 2.4 and Figure C.1. The changes in structure caused by this pre-oxidation must be significant and long-lived, as a second reduction following the oxidation reduced the activity, but only slightly.

There are no apparent benefits to either activity or CO:$H_2$ ratio of alloying or mixing Ni with Co (Figure 2.3 and Figure 2.4). As seen in Table 2.1, Co is less active as a TM additive metal in REOs than is Ni, and from Figure 2.3 it is evident that roughly the same amount of Ni with no Co (e.g., in Ni0.5/Ce3/Zr or Ni0.3/Ce2/Zr) leads to a more active catalyst. However, the rates of deactivation are lower for Ni-Co than for either Ni or Co catalysts (Figure 2.5). While

the (typically) 24 h long runs shown in Figure 2.2-Figure 2.5 and Figure C.1 were not long enough for any Ni-based catalyst to completely deactivate, the Ni-REOs experienced a pressure increase over this time period (due to whisker carbon formation in the reactor) and slight deactivation (Figure C.1), while Ni-Co-REOs did not. In summary, the Ni-Co-REO catalysts are clearly more stable, but their stability is not tied mainly to coking rates, as Figure 2.5 shows.

### 2.3.3. Ni-Containing Catalyst Characterization

#### 2.3.3.1. X-ray Diffraction

XRDs of catalysts before/after DRM were done to highlight gross changes in phase behavior and morphology arising from long-term use. Figure 2.6 shows diffractograms of three spent catalysts. The supports after 500ºC calcination (not shown) were poorly crystallized with peaks characteristic of only Ce/La or Ce/Zr mixtures with distorted fluorite structures. But for both Ni0.2/Co0.2/Ce/Zr and Ni0.3/Co.0.3/Ce3/La there is evidence of phase separation of both the $CeO_2$-$La_2O_3$ and $CeO_2$-$ZrO_2$ mixtures. For $La_2O_3$ this is in line with past studies showing surface segregation upon prolonged high temperature treatments.[133, 134] For $CeO_2$-$ZrO_2$, phase separation is less detectable at 2:1 Ce:Zr (Figure 2.6) and not observed at all in 3:1 Ce:Zr (Figure 2.7), both with Ni. There is, however, phase separation in 3:1 Ce:Zr with Pd (not shown). Scherrer calculations show that the particle size of the primary Ce-Zr fluorite phase remains <20 nm (only ~7 nm for 3:1 Ce:Zr) following reaction, when Ni is present. For Ce-La or for Pd-containing catalysts, the spent catalyst REO domains are larger, > 20 nm.

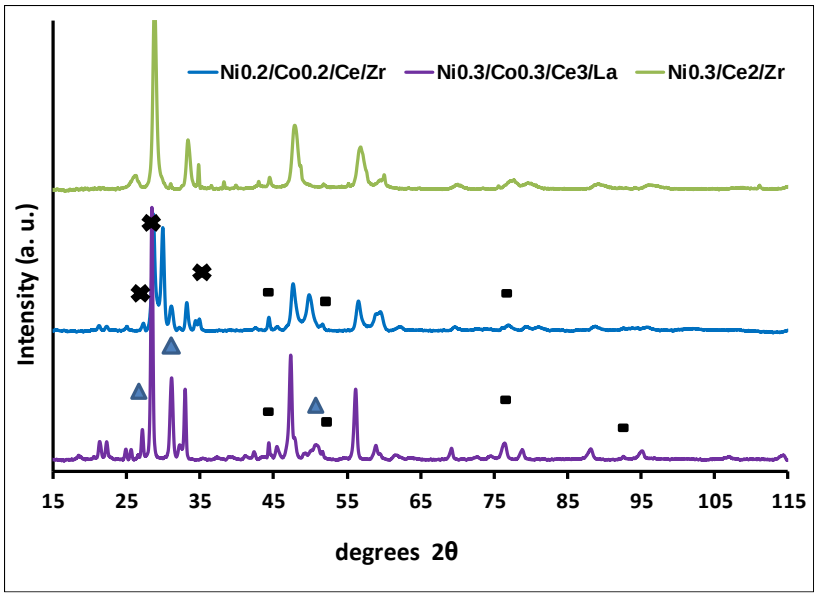


Figure 2.6. XRDs of spent catalysts. Filled squares mark peaks of fcc Ni (Co) metal, filled crosses $ZrO_2$ (tetragonal or monoclinic), and filled triangles $La_2O_3$. All other peaks are characteristic of $CeO_2/ZrO_2$ or $CeO_2/La_2O_3$ with the distorted fluorite structure.

The XRDs of the spent catalysts showed small peaks characteristic of metallic Ni or Co (fcc) at 44.4, 51.7 and 76.4 degrees 2θ. The XRDs of both Ni and Co fcc metals are similar. Quantitative XRD examination of 3 and 1 wt% Ni physical mixtures with $CeO_2$-$ZrO_2$ suggests that the metallic Ni and/or Co formed here could be as much as 40% of the total Ni-Co present in the spent catalysts, although overlap with other peaks such as carbon (~44.5°) contributes to overestimation. Nonetheless, it is evident that some of the late TM, initially mixed into the REO oxide, has egressed from the fluorite phase during the final reduction and DRM. The 40% calculation is based only on catalysts where little carbon was formed (e.g., Ni0.2/Co0.2/Ce/Zr), by taking the area ratio of the peak at 44.7° to those of the three largest Ce-Zr or Ce-La peaks.

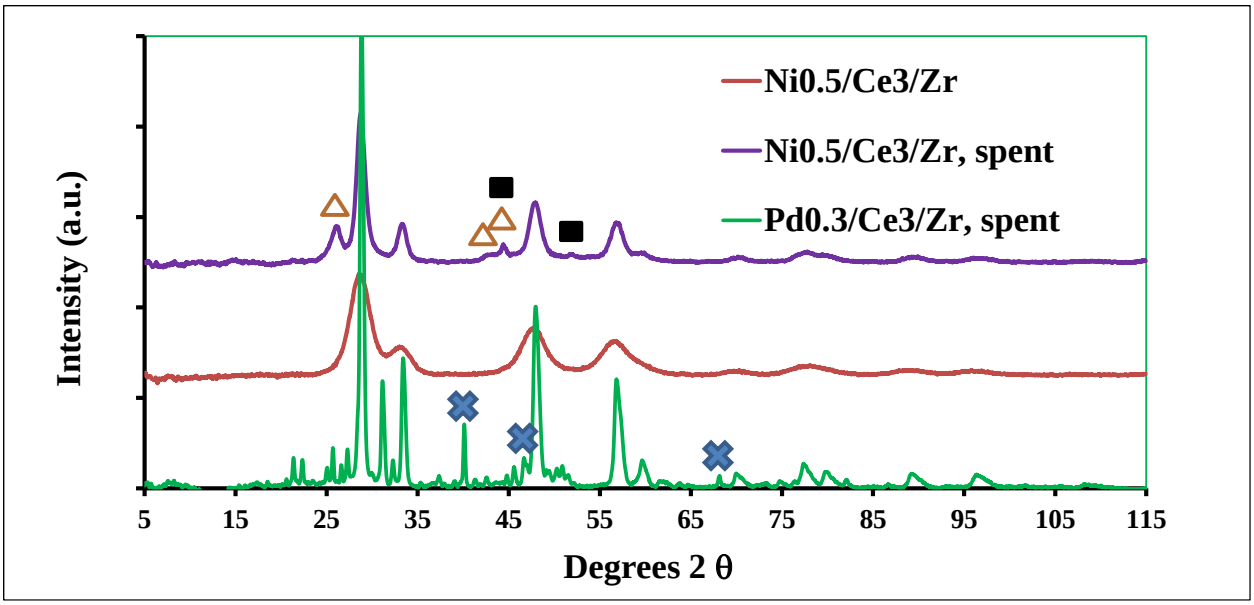


Figure 2.7. XRDs of Ce3/Zr-based catalysts. Filled squares mark peaks of fcc Ni metal, filled crosses metallic Pd, open triangles carbon. All other peaks are for the Ce/Zr oxide distorted fluorite phase (Ni0.5/Ce3/Zr) or for this phase plus some monoclinic $ZrO_2$ (Pd0.3/Ce3/Zr).

While carbon is clearly present in the spent Ni0.5/Ce3/Zr at 26.1, 42.5 and 44.5 degrees 2θ (Figure 2.7), and several other spent catalysts, it is mostly absent in the Ni-Co REOs. Spent Pd0.3/Ce3/Zr showed evidence of even more carbon, and a prominent metallic (Pd) phase.

We used CO adsorption at 25°C to measure the dispersion of any metallic phase present. However, little to no CO adsorption was observed for any of the Ni-REOs used here, with the exception of Ni20/CZA-40 (contains 20 wt% Ni). Computed metallic dispersions of these spent Ni- and Pd-containing catalysts were <1% on a total metal basis. The Ce-La and Ce-Zr supports themselves also cannot adsorb CO at this temperature. These results parallel $H_2$ chemisorption results for Ni-$CeO_2$-$Al_2O_3$ catalysts,[36] and other dispersion method measurements on Ni-$CeO_2$-$ZrO_2$.[94, 135]

We highlight that the fixed bed reactor testing demonstrates that: (a) the pre-oxidized Ni-Ce-Zr oxide catalysts are more active and already at maximum activity at the start of a run; (b)

all of the Ni-REO and Ni-Co-REO catalysts rapidly attain maximum activity, which can be maintained over several days. Figure C.2 and Figure C.3 show that for two typical spent catalysts, Ni0.3/Co0.3/Ce3/La and Ni0.24/Co0.24/Ce/Zr, the pre-oxidation essentially eliminates the peaks characteristic of metallic Ni and Co, although they return after several days usage as DRM catalysts.

**2.3.3.2. Raman Spectroscopy**

Raman can be used to explore the nature of oxygen vacancies present in both the support mixed oxides and the TM-containing catalysts. The key feature of the Raman spectra (Figure 2.8) of Ce3/La and Ce3/Zr catalysts is the Ce-O $F_{2g}$ band, at 464 $cm^{-1}$ for pure $CeO_2$. For Ce3/Zr this band does not shift, but for Ce3/La it red shifts to 445 $cm^{-1}$. This in in agreement with past studies.[136-139] However, for Ni0.5/Ce3/Zr this band red shifts to 455 $cm^{-1}$. The decreased intensities and increased band broadening for the Ni- and Ni-Co doped catalysts follow from the knowledge that the $F_{2g}$ band decreases and broadens upon doping of the fluorite lattice with metal atoms, due to increased disorder.[109, 140-143] The red shift for both fresh and spent Ni0.5/Ce3/Zr confirms that there is still Ni located within the $CeO_2/ZrO_2$ structure for the spent catalyst. Metal doping increases the asymmetry of the band on the lower frequency side, as also observed in Figure 2.8.

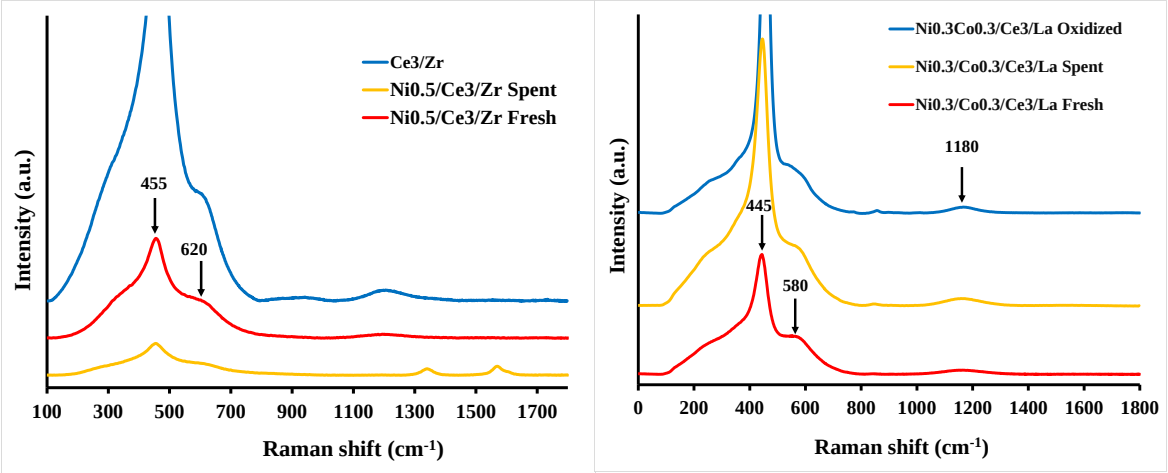


Figure 2.8. Raman spectra of (a) Ni-REO and (b) Ni-Co-REO catalysts

Band width is tied to grain size, larger crystals leading to more intense, narrower bands.[137, 140, 144, 145] For Ni0.3/Co0.3/Ce3/La, both high temperature oxidation and extended use in DRM should increase grain size, and the intensities in Figure 2.8b follow the expected trend. But for Ni0.5/Ce3/Zr the exact opposite is found, with intensities decreasing upon use, suggesting little crystal ripening, but further metal dissolution in the REO matrix. This is in partial agreement with the Scherrer calculation for the grain size of the Ce-Zr phase in the spent catalyst (only ~7 nm). Therefore, in the presence of the TMs, Ce3/La and Ce3/Zr behave quite differently.

The band at 580-590 $cm^{-1}$ in Ce3/La (LO phonon mode) is associated with oxygen vacancy formation and lattice disorder, both intrinsic and by mixing with La;[136] in Ce3/Zr the similar band appears at ~620 $cm^{-1}$.[138, 146] For Ni/$CeO_2$, the band is at ~615 $cm^{-1}$. The band at 1180-1190 $cm^{-1}$ is for a similar LO phonon mode. There are no bands characteristic of either Ni(0) or NiO. The primary Ni-O bands (not observed) would be at 1490-1550, 1090-1100, and 700-730 $cm^{-1}$.[147, 148] Again, the evidence points to more carbon associated with spent Ni-REO

than Ni-Co REO; both the D-band (1350 $cm^{-1}$) and the G-band (1580 $cm^{-1}$) of graphite are present in spent Ni0.5/Ce3/Zr.

**2.3.3.3. XPS**

XPS was used to explore the oxidation states of Ce in both fresh and spent samples. The Ce 3d core level spectrum shows multiple bands in the range of 880-920 eV due to O 2p valence band - Ce 4f hybridization.[149] The Ce 3d spectrum can be deconvoluted into ten bands. Five of them are assigned to $3d_{5/2}$ features, *v0* (881.2 eV), *v* (883), *v′* (886), *v″* (889.2), and *v‴* (898.5). The rest are assigned to $3d_{3/2}$, denoted *u0* (899.7 eV), *u* (901.6), *u′* (904), *u″* (908) and *u‴* (917.4).[138, 149-152] The spectra and their deconvolution are shown in Figure 2.9, Figure C.4 and Figure C.5. The fraction of surface $Ce^{3+}$ was calculated as:

$$Ce^{3+}\% = \frac{Ce^{3+}}{Ce^{3+} + Ce^{4+}}$$

where $Ce^{3+}$= *v0*+ *v′*+ *u0*+ *u′* and $Ce^{4+}$= *v*+ *v″*+ *v‴*+ *u*+ *u″*+ *u‴*.[153]

In Figure 2.9, the intensity of the band at ~917.4 eV ($Ce^{4+}$) decreases and the intensities at 886 and 904 eV ($Ce^{3+}$) remain intense in the spent compared to the fresh sample, phenomena also observed elsewhere.[150, 154] The $Ce^{3+}$ surface concentrations of fresh and spent Ni0.2/Co0.2/Ce/Zr were computed as 32% and 40%, respectively. Since the $Ce^{3+}$ content is directly related to the surface oxygen storage capacity and oxygen vacancies, a higher $Ce^{3+}$ concentration suggests better coking resistance, as exhibited by the Ni-Co-REO catalysts. In Figure C.4 and Figure C.5, the $Ce^{3+}$% in spent Ni0.15/Ce2/Zr and spent Ni0.24/Co0.24/Ce/Zr are 25% and 62%, respectively. An effect of Co is therefore to further promote the reduction of $Ce^{4+}$, as has also been observed in Co-$CeO_2$.[154] These $Ce^{3+}$ numbers connote trends only,

because it is generally agreed that irradiation at high vacuum causes additional $Ce^{4+}$ reduction, although the full extent is unknown.[155]

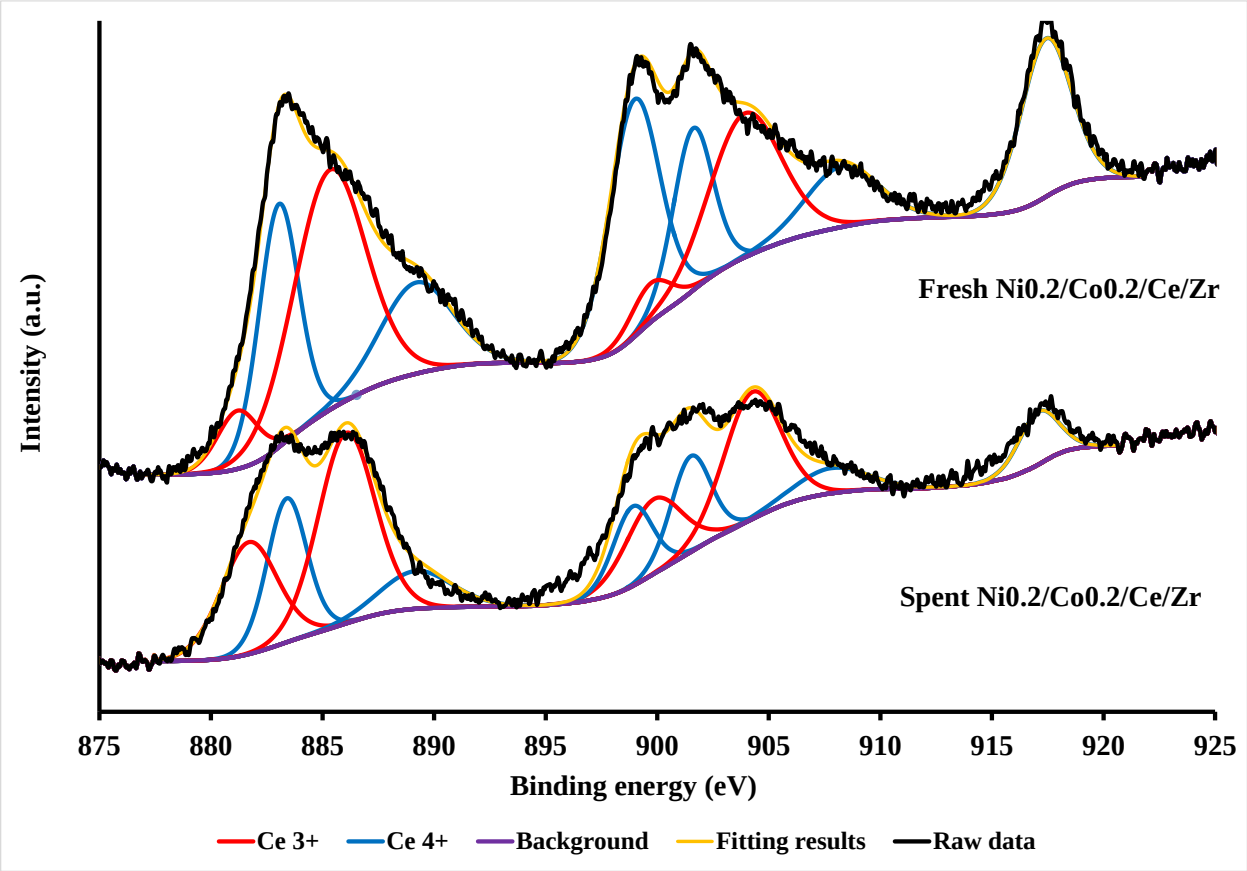


Figure 2.9. Ce3d XPS of Ni0.2/Co0.2/Ce/Zr

Figure C.6 shows the Ni $2p_{3/2}$ spectra of some fresh (unoxidized, unreacted) and spent catalysts. The primary band for all the spent samples is at 856-857 eV, attributed to $Ni^{2+}$ species that are in a different coordination environment than Ni atoms in NiO (~853.7eV).[102, 107, 109, 154] Several $Ni^{+2}$ salts with highly distorted octahedral environments give similar binding energies. $Ni^0$ bands (not observed) are normally at ~852.6 eV.[147, 156] A broad band can sometimes be observed in fresh samples at ~863 eV, assigned as a combination of the shake-up satellite and the main peaks of $Ni^{2+}$ (NiO) and $Ni^{3+}$ ($Ni_2O_3$).[157] However, this band is also absent in the spent

catalysts. For the fresh samples the Ni $2p_{3/2}$ band is at slightly lower binding energy, suggesting the presence of some $Ni^0$. In one case (Ni0.5/Ce3/Zr) a second contribution was obvious, and deconvolution suggested roughly 27% of the Ni was likely $Ni^0$.

Surface composition ratios determined by XPS are given in Table 2.2, along with the bulk composition ratios used in the catalyst syntheses. Compared with fresh catalyst, the Ni concentration at the surface decreased somewhat during the reaction, more so for the catalysts without Co.

Table 2.2. Summary of the results of XPS, ICP and TPO analyses

| Catalyst | State | Ni/(Ni+Ce) (at%, bulk) | Ni/(Ni+Ce) (at%, XPS) | TPO result (mg C/mg cat) |
|---|---|---|---|---|
| Ni0.2/Co0.2/Ce/Zr | Fresh | 15 | 25 | |
| | Spent | 15 | 16 | 0.099 |
| Ni0.24/Co0.24/Ce/Zr | Spent | 19 | 11 | 0.16 |
| Ni0.15/Ce2/Zr | Spent | 7.1 | 19 | 0.068 |
| Ni0.5/Ce3/Zr | Fresh | 14 | 80 | |
| | Spent | 14 | 13 | 0.34 |
| Ni0.3/Co0.3/Ce3/Zr | Fresh | 10 | 23 | |
| | Spent | 10 | 15 | 0.026 |

**2.3.3.4. XANES and TPR**

Given the poor quality of the spent 2p3/2 Ni XPS, XANES was also used to explore the oxidation states of Ni in both fresh and spent samples. The Ni K-edge data for spent catalysts are shown in Figure 2.10. Again, Ce3/La and Ce/Zr catalysts behave quite differently. The Ni0.3/Co0.3/Ce3/La catalyst showed little to no evidence of reduced Ni. This catalyst was not pre-oxidized; the Ni remained in the same state throughout DRM. On the other hand, all of the Ce/Zr mixed oxide catalysts underwent significant reduction during reaction, according to XANES. While the spectra show some differences from Ni foil consistent with the presence of oxidized Ni (in particular the increased intensity at ~8347 eV),[95] it is evident that the bulk of the

Ni is in a reduced state. The white line position of NiO (8345 eV) is quite close to a derivative peak of Ni foil after its white line position. Therefore linear combination fitting of unknown spectra is unlikely to lead to exact numerical results. We did the procedure anyway, to spot trends, and determined that for Ni0.3/Co0.3/Ce3/La linear combination fitting suggests 95% $Ni^{+2}$ by XANES, while for all the others there is on average 7%.

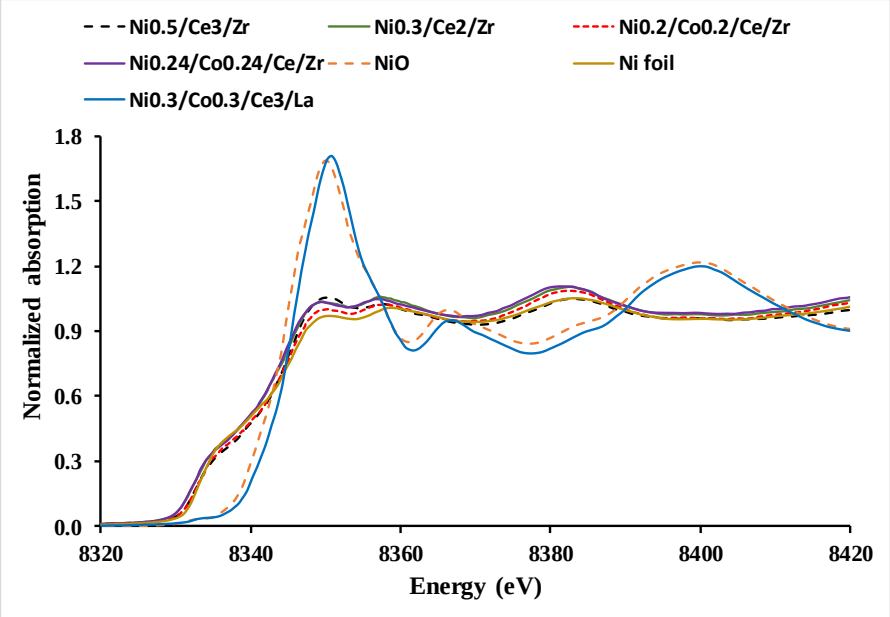


Figure 2.10. Ni K-edge XANES of spent catalysts

The reduction propensity of the catalysts was further examined by TPR. Figure 2.11 shows the $H_2$ reduction of representative Ni- and Ni/Co-containing catalysts. The fresh Ni-containing catalysts show a large reduction peak centered at 247°C for Ni0.3/Ce2/Zr and 264°C for Ni0.15/Ce2/Zr, with a second smaller peak for both centered at ~390°C. The even smaller peaks at >550°C represent further reduction of bulk $CeO_2$, often promoted by the TMs.[14, 135, 147, 158-161]

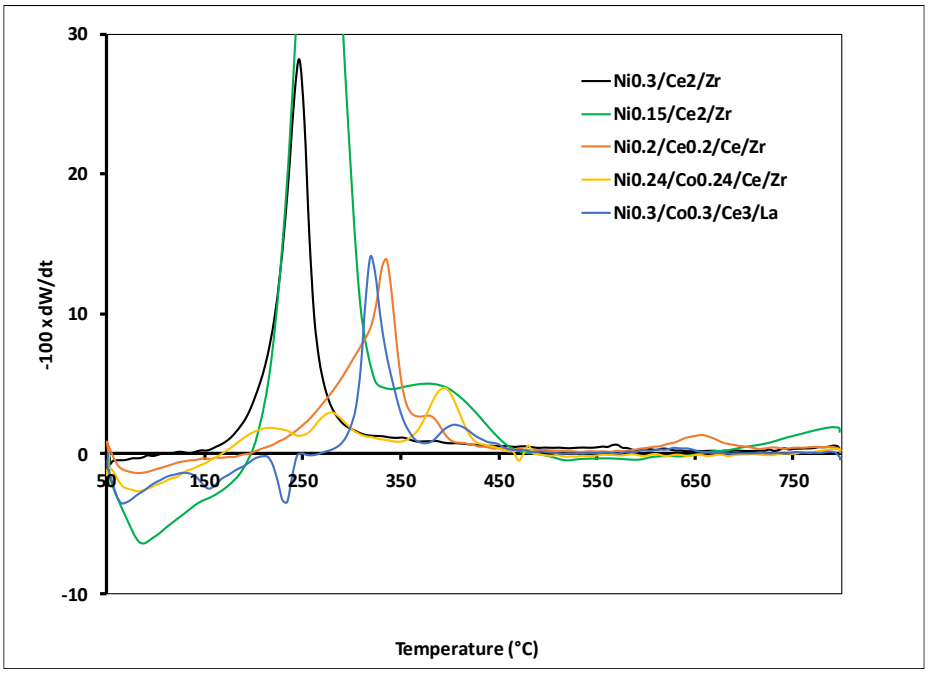


Figure 2.11. TPR (25% $H_2/N_2$, 5°C/min) of unreduced catalysts. The derivative weight of the catalyst is plotted on the y-axis.

The lower temperature peak is variously attributed to facile reduction of the surface oxygens of NiO, and of reduction of oxygens creating vacancies in the mixed oxide.[14, 147, 159, 162-164] It makes sense that for the catalyst with less Ni this peak would appear at higher temperature, as a higher percentage of the Ni would be dispersed (soluble) within the REOs. The higher temperature peak is usually attributed to NiO domains interacting with $CeZrO_x$. For the catalyst with less Ni, this peak is again larger, reflecting better dispersion in the oxide, because the maximum of the reduction peak for bulk NiO is ~420-447°C,[109, 135, 161] which is higher than any of the maxima observed here. These results suggest strong interaction with the REO, in agreement with the XRD, Raman, chemisorption and XPS data.

For the Ni/Co catalysts, the reduction peaks are at higher temperature, the only exception being the first peak for Ni0.24/Co0.24/Ce/Zr at ~220°C, suggesting imperfect alloying of Co and

Ni for this catalyst initially, because Co on $CeO_2$ or $CeO_2/ZrO_2$ in low loadings is reduced at this temperature.[158, 165] Alloy Ni-Co reductions are characterized by peaks with maxima between 360-500°C,[166] different peaks representing different aggregate sizes. This behavior was observed, with at least two distinct higher temperature reduction peaks for all the Ni/Co catalysts. The lower temperature peak arises from the smaller aggregates interacting strongly with $CeO_2$.[147, 158, 163] The most important result is that a higher average oxidation state for Ni can be maintained in alloy materials; less total reduction is observed, taking place at higher temperatures. Also, there is clearly less reduction for the Ce3/La-supported catalyst, in agreement with the XANES results.

### 2.3.4. Density Functional Theory Calculations

DFT calculations were first used to investigate oxygen vacancy formation and distribution in La-doped ceria. Detailed results are presented in the Appendix C (Figure C.7-Figure C.12 and Table C.3-Table C.5), and we summarize the main findings here. For $Ce_xLa_{1-x}O_{2x}$ bulk and surface models, we find that the reaction energy to remove a lattice O as ½ $O_2$ is negative when two La atoms are included. This is expected, allowing La to take on the 3+ formal oxidation state, and we refer to these oxygen vacancies as "stoichiometric vacancies." Using either bulk $La_2Ce_{30}O_{63}$ or $La_8Ce_{24}O_{60}$ periodic models, we find a significant preference for these stoichiometric O vacancies to occupy next-nearest neighbor positions to La atoms. Rather than removing O atoms directly adjacent to La atoms, the preference for next-nearest neighbor vacancies, along with no observed preference for multiple La dopants or vacancies to cluster, suggests facile mixing of La and Ce in the fluorite structure. The formation of a second O vacancy to form the $La_2Ce_2O_6$ structure has a reaction energy of 2.76 eV, whereas vacancy formation to form $Ce_4O_7$ has a reaction energy of 3.77 eV. Vacancy formation that reduces both

a La and a Ce atom to form $LaCe_3O_7$ has a formation energy of 1.53 eV, suggesting isolated La atoms not present in pairs can greatly promote $Ce^{3+}$ formation. Using a $La_2Ce_{18}O_{39}$ model of the (111) surface, we find that La atoms prefer to surface segregate, with at least one of the La atoms in the surface layer. The most stable arrangement occurs with the O vacancy in the first subsurface layer. Beyond the stoichiometric O vacancy, we find La doping promotes further O vacancy formation.

We also used DFT to examine the DRM mechanism over a Ni-doped $CeO_2$ surface. The model used was a 2x2 $CeO_2$ (111) surface, with one of the surface Ce atoms substituted by Ni. An adjacent O atom was also removed, as we found vacancy formation to be exothermic allowing Ni to form a stable 2+ oxidation state. This model is used with the hypothesis that Ni atoms are well dispersed and mixed ("doped") into the ceria in order to facilitate DRM. Despite the presence of a coordinatively unsaturated Ni site, all $CH_x$ adsorbates bind to surface O atoms, with adsorbed CH* and C* binding both to O and Ni (Figure C.13). The elementary steps involved in methane dehydrogenation to form a surface adsorbed C* atom and 4 H* atoms are all exothermic, suggesting methane conversion is viable on the Ni-doped ceria surface (Figure C.14). As all $CH_x$ (x=0, 1, 2, 3) species bind to surface O atoms, it is unlikely for the doped Ni to form carbonaceous species on the mixed oxide surface, which is in agreement with our reaction results at both lower and higher reactant partial pressures.

## 2.4. Discussion

### 2.4.1. Nature and Importance of Oxygen Vacancies, Ce/Zr versus Ce/La

The addition of La or Zr to the $CeO_2$ lattice increases the concentration of vacancies, as predicted by the DFT results and confirmed by XPS and Raman. This clearly impacts DRM performance favorably, although in the case of many catalysts with TM additives, reverse water-

gas shift (RWGS) rates are also increased. Among the REOs, $La_2O_3$ doped into $CeO_2$ results in the most oxygen vacancies,[136] either "stoichiometric" or due to isolated La-atoms affecting surrounding Ce. Unlike isovalent nonreducible dopants ($Zr^{4+}$), which affect $\Delta E_v$ (vacancy formation energy) due to a size effect on the relaxation energy, trivalent cations ($La^{3+}$) change $\Delta E_v$'s by creating O•− radicals that are easier to remove (per DFT predictions).[66] As shown above, "stoichiometric" vacancies are easily formed with La addition, and Zr is equally effective in promoting formation of vacancies that reduce Ce to the 3+ state and can participate in redox cycling.[124] DFT simulation of the Ce:La = 30:2 supercell confirms an energetic preference for next-nearest neighbor (to La) vacancy sitings. Even for the Ce:La = 24:8 supercell (same as the 3:1 composition used here), the vacancies do not prefer to cluster next to $La^{3+}$.

The $\Delta E_v$ values for Ce2/Zr and Ce/Zr are slightly less than Ce3/Zr,[61] and so all of these compositions might be expected to show similar DRM activity to Ce3/La (where lower molar ratios cannot be monophasic under any conditions), with the same TM to activate the $CH_4$. This optimal Ce:Zr range (1-3) from the DFT studies is consistent with experimental results showing that $Ce_xZr_{1-x}O_2$ compositions of $0.5<x<0.8$ give the highest OSCs.[62-65]

### 2.4.2. Comparative Reaction Behavior, DRM, RWGS, Coking

DRM rates at low conversion are similar for the same metals, for example, in Table 2.1 compare Ru0.2/Ce3/La to Ru0.1/Ce/Zr, or Mn0.4/Ce3/La to Mn0.2/Ce/Zr, or Pd0.4/Ce3/La to Pd0.27/Ce3/Zr, or Ni0.3/Ce3/La and Ni0.6/Ce3/La to Ni0.12/Ce/Zr, Ni0.15/Ce2/Zr, Ni0.3/Ce2/Zr, and Ni0.5/Ce3/Zr. Within this Ce:Zr range the vacancy concentrations themselves are more sensitive to the TM.[102, 138] Changing the TM varied the reforming rates by an order of magnitude, which was more than obtained by just varying the Ce:Zr ratio.

The $H_2$/CO ratios observed here (all <1) show that, for Ni-based REOs at high conversion, RWGS takes place. While a Ce3/La support can result in an active and stable catalyst, it is nonetheless impractical for DRM due to higher rates of RWGS and sintering (based on the XRD results) and Ce-La phase demixing, all more than in 3:1 and 2:1 Ce-Zr oxides. We speculate that other trivalent REO dopants would exhibit similar weaknesses. The experimental results are consistent with the DFT calculations showing that La should surface segregate leading to more O vacancies at or near the surface, also in agreement with past experimental findings,[108] and ultimately resulting in phase demixing and sintering, because both pure $La_2O_3$ and pure $CeO_2$ are more prone to sintering than their mixture.

The results for Ce3/La also highlight an apparent weakness of the rapid assessment method – it cannot immediately identify those catalysts that exhibit high rates of RWGS. However, even for such catalysts, the calculated reforming rates from the rapid assessment method are reasonably accurate, with a calculated <7% error, after accounting for the relative DRM/RWGS ratios and the differences in their heat effects.

Our results to date lead us to conclude that, in the absence of Co, only Ce:Zr = 3 catalysts appear to be entirely stable to long-term deactivation (Table 2.1 and Figure C.1), which conclusion for the lower Ce:Zr ratios is consistent with the work of Kiennemann and co-workers.[89] This deactivation takes place through a combination of metal sintering to some zero-valent aggregates, gradual oxide demixing and loss of surface area, and (less certainly) coke formation. The results in Table 2.1 show that $ZrO_2$ actually increases coking rates for Ni/$CeO_2$-based catalysts, in agreement with others.[14] However, with Co present, the range of potentially useful Ce:Zr ratios is expanded and coking suppressed. The estimated coke amounts from TPO measurements (Table 2.2) are low for DRM catalysts, and the result for Ni0.24/Co0.24/Ce/Zr is

slightly misleading in that it was kept online for 6 days, without deactivation after the first day. The obvious conclusion (as Co in Ce-Zr oxides by itself is less active and not as stable) is that Co and Ni are interacting, a conclusion reinforced by the TPR results.

### 2.4.3. Nature of the TM-Ce Interactions in DRM

The results suggest strong oxidized metal-Ce interactions, as found elsewhere for Ni-$CeO_2$ both with and without a second dopant oxide, even under highly reducing conditions,[36, 89, 102, 107, 135, 147, 164, 167-169] and also for Co-$CeO_2$.[158] The XPS results, in particular Ni 2p peak locations and the additional $Ce^{3+}$ found, are often ascribed to such interactions.[102, 147, 164, 167, 170] The characterization results do not indicate the formation of large metal aggregates (except for the 20 wt% Ni catalyst) or bulk NiO, and the DFT results suggest the Ni-$CeO_2$ mixed oxide avoids coke formation by preferentially forming C-O bonds after methane activation. Therefore, the likely location of active Ni and Ni-Co is in intimate contact with the oxide lattice. This conclusion is consistent with the XPS, Raman, chemisorption and TPR results, but, just as importantly, consistent with the reaction behavior after pre-oxidation, and the fact that the DRM activity remains constant even while more Ni is being reduced during the first days of reaction.

### 2.4.4. Comparison to Other Stable DRM Catalysts

Nevertheless it is evident by XANES that for Ce-Zr catalysts reduction of bulk Ni is taking place during DRM, as also found from in-situ XANES for Ni/$ZrO_2$ and Ni-Co/$ZrO_2$.[95] Reconciling the XANES and XPS results for the Ce-Zr catalysts requires recognizing the limitations of XPS. In the absence of other peaks characteristic of NiO, the XPS results (Ni $2p_{3/2}$) for Ce-Zr catalysts do not prove the presence of NiO, merely an electron-deficient form of Ni in (probably) a different coordination environment. Bhatia and co-workers suggested the increased binding energies resulted from Ni-Co alloying, not $Ni^{2+}$.[170] But as others do not see

any shifts in-situ (i.e., the Ni $2p_{3/2}$ is exactly where it should be for Ni(0)) at 427°C,[171] or clearly see peaks characteristic of both oxidized and reduced Ni,[147] a universal explanation for the XANES-XPS discrepancy is not available at present.

We conclude that the active and stable Ni-Co REOs are characterized by interactions between Ni and Co, but additional interactions exist between the metals in small aggregates and the mixed oxide. The primary benefits of Co are in generating mixed metal sites characterized by lesser rates of sintering and coking (Table 2.1, Table 2.2, Figure 2.5), and which generate additional oxygen vacancies (XPS results), above those of the Ce-Zr or Ce-La oxides. However, we have not yet identified specific structures responsible for the stability in DRM of the mixed Ni-Co catalysts. For Ni-Ce-Zr catalysts of similar contents, others have calculated only 40-80% Ni reduction by 800°C in $H_2$ TPR,[94, 161, 164] but such calculations are subject to dispute.[14] Our XANES results show that significant TM reduction does take place for Ce/Zr, but not for Ce/La, but in both cases the Ni-Co interactions lead to similar DRM results.

There have been reports of reduced coking in various reforming processes with supported Ni-Co catalysts, on $Al_2O_3$,[172] $(M_{0.75}Mg_{0.25})Al_2O_4$,[88] $ZrO_2$,[95] $TiO_2$.[173] and $MgO/ZrO_2$.[170] But these catalysts appear to be different from the Ni-Co-REO catalysts studied here. Reduced Ni on spinel supports is characterized by flat low-index facets of Ni in registry with the spinel,[88] with some or much of the metal in the spinel.[88, 170] On both $ZrO_2$ and $TiO_2$, there are clearly large metallic domains on the surface, which for $ZrO_2$ at least leads to noticeable deactivation. The TOF on a per metal atom basis of Ni-Co-$TiO_2$ is low. And in almost all of these studies the reaction conditions were less conducive to coking than ours (e.g., higher temperature and/or lower $CH_4$:$CO_2$ feed ratios). Aw and co-workers, who used catalyst formulations similar to ours

(e.g., Ni0.3/Co0.45/Ce4.2/Zr), but on $Al_2O_3$ or SiC supports, also found good long-term stability (550 h, minimal deactivation), with rates similar to ours at 750°C.[174]

But the most active and stable DRM catalysts could be those with Ni-Co supported on $MgAl_2O_x$ (Ni:Co ~0.73, 3-4 times more active than the best Ce-Zr catalysts).[175] The Ni-Co mixture or alloy in these catalysts has been described as electron-deficient, stable metallic nanoparticles,[176] in accord with the XANES/XAFS/HRTEM work of Wang and co-workers (same support), who in particular noted the more electron-deficient state of Ni in Ni-Co catalysts, compared to Ni only catalysts.[87] This general picture also appears to hold for Ni-Co-$CeO_2/ZrO_2$.

The behavior of pre-oxidized Ni-Co-$CeO_2/ZrO_2$ catalysts suggests that, whatever the precise nature of Ni-Co interactions, the DRM active sites are not large crystal zero-valent metal. Even when there was a XRD-visible metallic phase, it was small and constituted a minority of total metal sites, and the DRM rates of those catalysts without an XRD-visible metallic phase were higher. Interaction with the Ce-Zr or Ce-La supports, leading to smaller metal particle sizes and (at least for Ce-La) a higher oxidation state, is therefore seen to correlate with both lower coking rates and higher reforming rates.

**2.5. Conclusions**

1) Both Ce/Zr and Ce/La oxides with TM additives are active for DRM, activity tied to the generation of additional oxygen vacancies in the $CeO_2$ fluorite structure.

2) A rapid screening method based on DSC/TGA can identify the best TM additives (Ni, Ni/Co, Ru) to REOs based on simultaneous measurement of reforming and coking rates. The DSC/TGA screening method can be completed in at most 3 h, needs only small sample sizes (10-20 mg), and directly measures reaction rates at differential conditions. Results from this method agree with those obtained using conventional fixed-bed reactors in that a high coking rate

measured by the rapid screening method signals deactivation by coking on the longer (days) time scale of the fixed-bed reactor experiment, but requires much shorter preparation.

3) Using Co with Ni as TM additives (at near 1:1 ratio) results in further Ce reduction to $Ce^{3+}$, and lower rates of catalyst deactivation. However, Co by itself does not increase the rate of DRM, while a pre-oxidation of such catalysts does. There is strong interaction between the oxidized, highly dispersed metal atoms and the neighboring rare earth oxide.

4) Ni- and Ni/Co-based Ce-Zr oxide catalysts gradually form detectable (by XANES) zero-valent metal aggregates. While some oxide demixing takes place (except for Ce/Zr = 3), the catalysts show little to no deactivation over a period of a few days.

# CHAPTER 3. ON THE ENHANCED SULFUR AND CARBON TOLERANCE OF NI-CO DOPED RARE-EARTH OXIDE CATALYSTS FOR DRY REFORMING OF METHANE

## 3.1. Introduction

Carbon dioxide or "dry" reforming of methane (DRM) is potentially a better way to utilize greenhouse gases compared to steam reforming, since two GHGs are consumed and made into a useful industrial gas stream of theoretically 1:1 $H_2$/CO, $CH_4 + CO_2 \rightarrow 2H_2 + 2CO$.

The rationale and basics behind DRM have been reviewed extensively over the years.[2, 50, 177] However, several challenges remain in order to enable large scale implantation of DRM. The high temperatures required (typically >700°C) is one, and relatively fast deactivation of non-noble metal (mainly Ni-based) catalysts the other. The former challenge can be addressed by application of hybrid technologies such as oxy-steam $CO_2$ reforming (aka "tri-reforming"). The latter challenge has been addressed through alloying of Ni with certain other metals (Co, Mn) and/or the application of supports that slow down deactivation. As the deactivation can be due to coking, active metal sintering, or poisoning by sulfur, chlorine etc., or some combination of these, no support is at present considered optimal for all feeds. The two most important methane sources, natural gas and biogas, can both contain significant amounts of sulfur compounds (up to 100 ppm) such as $H_2S$, mercaptans, sulfides and tetrahydrothiophene,[22] all of which can eventually lead to catalyst poisoning.

We have discussed how to design and evaluate catalysts that can minimize coke formation and lead to stable catalysts for DRM in previous work.[178] It was found that mixed rare-earth oxide supports such as $CeO_2$-$ZrO_2$ and $CeO_2$-$La_2O_3$ can both lead to low-coking rates in DRM, with Ni-based catalysts. Addition of Co leads to further gains in stability for largely

unknown reasons, although Co by itself is not a very active metal for DRM. This study will focus on a comparison of long-term behavior of both, how sulfur-tolerant they are, the Ni-Co interactions, and how their final states actually differ greatly. This last result has implications toward the mechanism of DRM that will be exploited further in subsequent work. Fresh and spent catalysts of both types have been characterized by XAFS, CO chemisorption, TEM, and XPS.

## 3.2. Materials and Methods

### 3.2.1. Catalyst Preparation

Ce/La mixed oxides were prepared by a templated sol-gel method adapted from previous work.[54, 110-112, 178] The precursors for Ce and La were $(NH_4)_2Ce(NO_3)_6$ (98+%, Alfa) and $La(NO_3)\bullet 6H_2O$ (99.9%, Alfa), which would be dissolved in 96% water/3% methanol/1% TMAOH surfactant (25% in methanol). The molar ratio Ce/La was 3:1, with a 1/100 wt ratio of the oxides in the sol-gel synthesis mixture. Ammonia solution was used to gradually adjust the pH to 10.3 during aging (90°C, 2 d). After separation and repeated washings, the mixed oxide was dried at 120°C overnight and calcined at 500°C with air for 6 h. Ce/Zr oxides of molar ratios from 1:1 to 3:1 were prepared similarly to Ce3/La, except for the final pH (10.5). The Zr source was $Zr(NO_3)_4\bullet H_2O$ (Aldrich, 99%).

The Ce/La and Ce/Zr oxides were both modified with Ni and/or Co by deposition–precipitation from 0.3 M urea for 24 h at 90°C. The precursors were $Ni(NO_3)_2\bullet 6H_2O$ (Aldrich, reagent) and/or $Co(NO_3)_2\bullet 6H_2O$ (J.T. Baker, reagent). After separation and washings, these catalysts were reduced in 5% $H_2/N_2$ at 750°C for 6 h prior to use. The catalysts are denoted by

their elemental molar ratios (example - Ni0.24/Co0.24/Ce/Zr), which were determined by ICP-AES analysis after calcination and reduction.

### 3.2.2. Catalytic Reactions

Reaction experiments were conducted in a fixed bed ½" stainless steel tube packed with mixed α-alumina and either 0.5 or 0.25 g of catalyst, at 130 kPa total pressure. Electronic mass flow controllers were used to prepare the feed gas mixture ($CH_4$: $CO_2$=1:1). An online Agilent 6890N GC-MS was used to analyze the gas composition. Sulfur was added into the system in the form of aqueous dimethyl sulfoxide (DMSO, 12.1 mL DMSO/L) by a Harvard 944 infusion pump. This results in 1 kPa of water in the feed. It was established that the presence of this amount of water in the feed had no effect on the reactions. Further details of the reaction system are given in a thesis.[179]

The reforming rates at differential conditions were measured using a DSC/TGA method as discussed previously. The mol fractions of the feed gas mixture were $CH_4$: $CO_2$: $N_2$ = 0.25:0.25:0.5 (133 mL/min total). The experiments were performed at six temperatures between 650-775℃ using a TA SDT Q600 DSC-TGA. The measured endothermic heat flows were converted to fraction conversions using an ASPEN HYSIS® process simulator.

### 3.2.3. Catalyst Characterizations

The morphology and size of Ni:CZO NPs were analyzed by high-resolution transmission electron microscopy (HRTEM) at Oak Ridge National Lab using a 200 kV JEOL NEARM electron microscope equipped with double aberration correctors, a dual-energy-loss spectrometer, and a cold FEG source. The powder samples were dispersed in ethanol and drop casted on a 300 mesh, lacey carbon grid prior to imaging. The data were analyzed using ImageJ

1.50i software. One sample (Ni0.3/Co0.3/Ce3/La) was analyzed on the JEOL 2011 HRTEM at the LSU shared instrumentation facility, using similar procedures.

The X-ray photoelectron spectroscopy (XPS) spectra of fresh and spent Ni0.5/Ce3/Zr and Ni0.3/Co0.3/Ce3/Zr were collected under UHV at the endstation of the 5-m toroidal grating monochromator (5m-TGM) beamline at the Center for Advanced Microstructures and Devices (CAMD) at Louisiana State University. The endstation is equipped with an Omicron EA125 hemispherical electron energy analyzer with a five-channel detector. An Al Kα X-ray source (1486.6 eV) was used and XPS spectra collected in the constant pass energy mode with pass energies of 25 eV. XPS data processing was performed with CasaXPS, version 2.3.1 PR1.0. The binding energies were calibrated using the C1s signal (284.8 eV) as a reference. Other XPS spectra were taken at the LSU Shared Instrumentation Facility on a Scienta Omicron ESCA 2SR instrument with a 128-channel detector and processed similarly.

X-ray absorption spectra (both XANES and XAFS) were taken at the LSU Center for Advanced Microstructures and Devices (CAMD) HEXAS beamline, using a Ge 220 double crystal monochromator. The Ni K edge spectra were collected at room temperature in fluorescence mode with a Ni foil calibration standard. Data were processed (background subtraction, deglitching, merging of 9 spectra) using Athena 0.8.061.[113]

The Ni K-edge XAFS fitting was performed with Artemis 0.9.26. Five parameters were determined, $N_i$ (coordination number), $S_0^2$ (amplitude reduction factor), $\sigma^2$ (Debye-Waller factor), $\Delta E_0$ (deviation in $E_0$ caused by structural deviations from an ideal crystal structure) and $\Delta R$ (deviation in interatomic distance). The Ni and NiO standards were fit first to get information on $S_0^2$ with known coordination numbers and $\Delta R$. The fitting range in R space was 1-5 Å and all significant scattering paths were included.

## 3.3. Results

### 3.3.1. Long-term Catalyst Evaluations

Catalysts from previous work that were found to exhibit low rates of coking and high initial activities were tested over longer periods in a conventional fixed-bed reactor at 775°C.[178] No Co-only catalysts are included because these were found to be less active than any Ni-based ones. The activities can be quantified as the product of the GHSV (mL/(g•h), typically 44000), and the $CH_4$ conversion, on a molar basis. For a zero-order reaction, this is the same as the average rate of reaction, while for other orders it is close to that. DRM activities over long periods are dependent upon initial pretreatments that affect the distribution of Ni(0)/$Ni^{2+}$, as observed by us and others.[178, 180] We chose to standardize on the freshly reduced catalyst, although in general partly oxidized catalysts are more active, as shown in Figure 3.1, and give a higher $H_2$/CO ratio.

Catalysts containing both Ni and Co are stable over long periods but as seen the Ni-only catalyst undergoes steady if gradual deactivation. Ni-only catalysts at ratios less than 3:1 Ce:Zr are even less stable and not shown here. Sulfur tolerance experiments were also conducted at 775°C with two different amounts of feed sulfur, <1 ppm and 20-30 ppm. For <1 ppm sulfur, all the catalysts tested showed good sulfur tolerance (Appendix D, Figure D.1), either with no deactivation (those containing both Ni and Co) or gradual deactivation (Ni-only catalysts). However, when the sulfur concentration increased to 20~30 ppm, the only catalyst showing extended sulfur tolerance (four days online) is Ni0.24/Co0.24/Ce/Zr. As shown in Figure 3.2, the other catalysts deactivated completely after contacting with sulfur in amounts that corresponded closely to the total amount of Ni present. There were 0.18 mmol Ni in the Ni0.24/Co0.24/Ce/Zr load in this experiment. Using an $H_2S$ gas monitor we confirmed that there

was unadsorbed $H_2S$ in the reactor exhaust, at concentrations consistent with what is formed from the breakdown and hydrogenation of DMSO. But there was also unadsorbed sulfur in the exhausts of the catalysts that completely deactivated during these experiments. After the sulfur was removed from the feed, the average activity of Ni0.24/Co0.24/Ce/Zr was 16% higher than the initial activity in Figure 3.1.

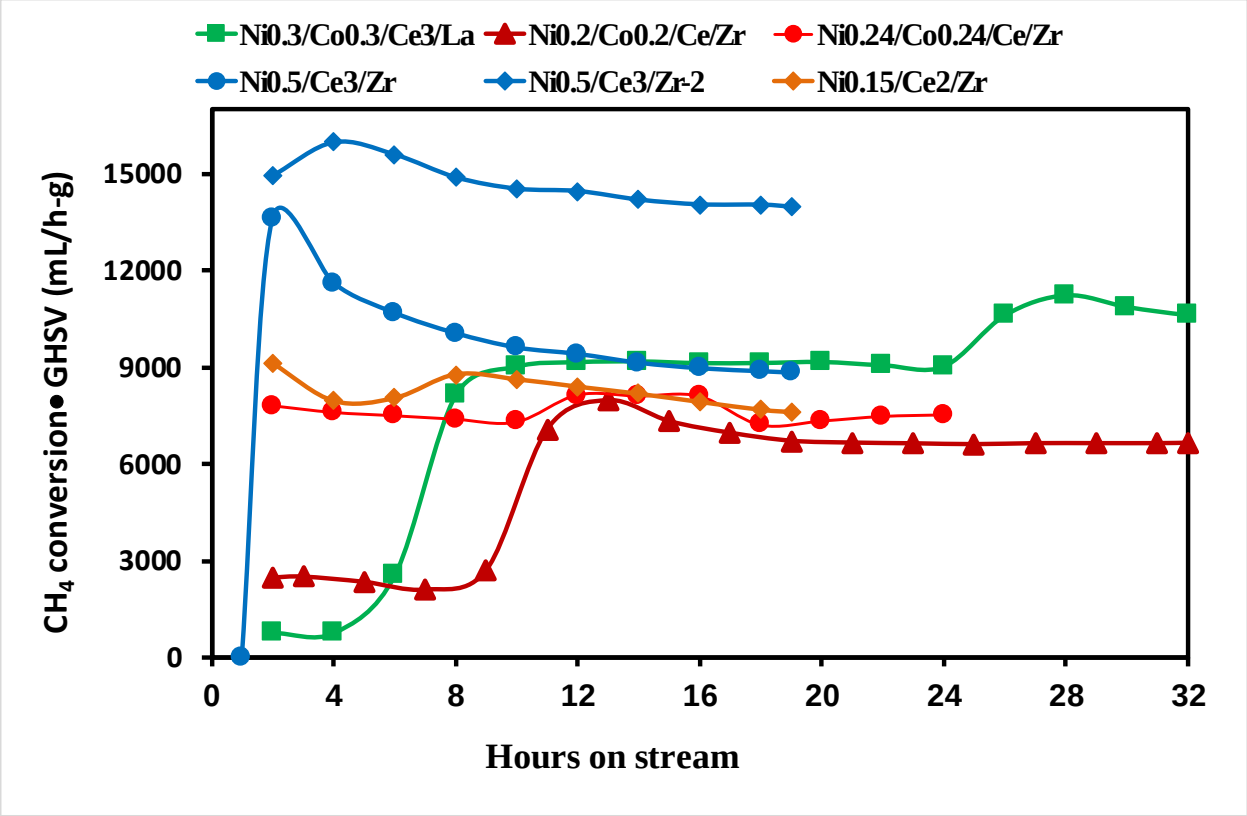


Figure 3.1. Activities at 775°C of freshly reduced (5% $H_2$, 750°C, 6 h) Ni-based catalysts with time on stream. Second data set at higher activity for Ni0.5/Ce3/Zr-2 taken after an intermediate oxidation step in air at 800°C. The Ni-Co catalyst runs were extended for a few more days and they were stable.

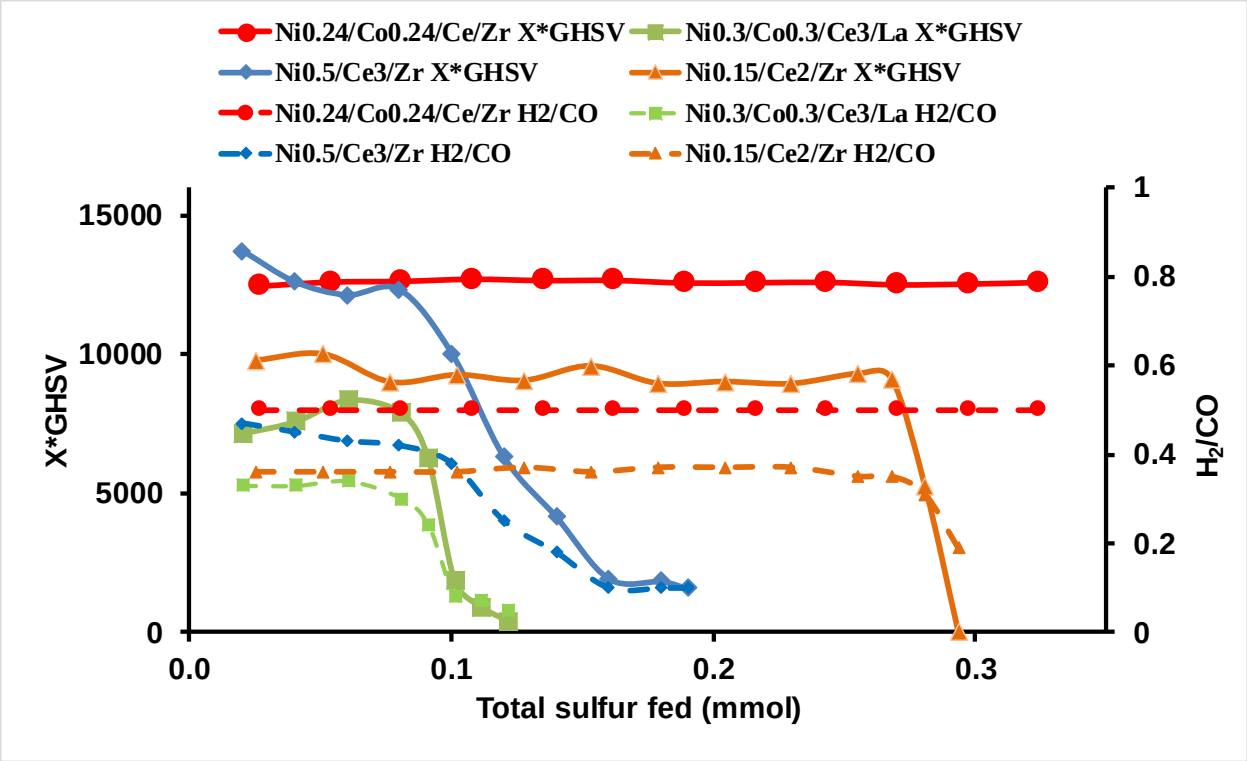


Figure 3.2. Activities at 775°C of catalysts shown in Figure 3.1 after the addition of 20-30 ppm sulfur fed as DMSO. The fraction conversion of $CO_2$ is denoted by "X".

### 3.3.2. Intrinsic Activities

The observed reforming rates for Ni0.2/Co0.2/Ce/Zr and Ni0.3/Ce2/Zr were measured at six temperatures from 650-775°C from the endothermic DSC heat rate using the procedure developed previously.[178] The conversions in these experiments are all <5%, so the observed rates are characteristic of the initial feed composition. The activation energies were computed from the Arrhenius plots of Figure 3.3 and are shown in Table 3.1 along with the measure coking rate at one of the temperatures.

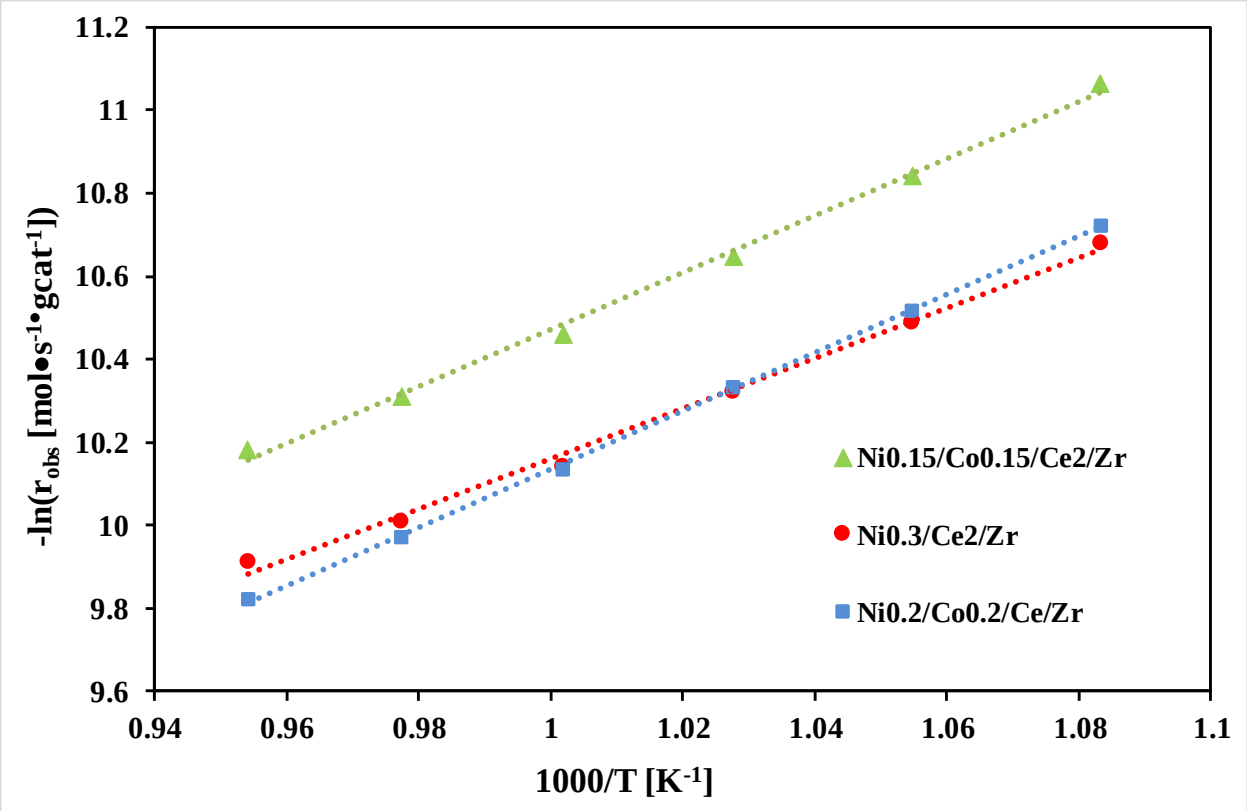

Figure 3.3. Arrhenius plots based on observed rates computed from DSC heat rates.

Table 3.1. Results from low conversion DRM reactions in DSC/TGA

| Composition | Total Activation Energy (kJ/mol) | Coking Rate at 725˚C $\left(\frac{\text{moles of carbon}}{\text{s} \bullet \text{gcat}}\right)$ |
|---|---|---|
| Ni0.3/Ce2/Zr | 50±5 | 1.2E-8 |
| Ni0.2/Co0.2/Ce/Zr | 58±2 | 4.8E-9 |
| Ni0.15/Co0.15/Ce2/Zr | 57±5 | ~0 |

The Weisz modulus was used to estimate the influence of pore diffusion on reaction rates in these DRM experiments. The Weisz modulus ($W_M$) can be expressed as follows:[181, 182]

$$W_M = \frac{r_{vobs}\, L^2}{C_A D_e}$$

Where $r_{vobs}$ is the observed reaction rate per unit particle volume, $L$ the characteristic catalyst dimension, $C_A$ the concentration at the limiting reactant in the fluid and $D_{eA}$ its effective diffusivity in the catalyst particle. For $W_M << 1$, there should be no pore diffusional limitations. In our case, the Weisz moduli (Ni0.2/Co0.2/Ce/Zr) for $CH_4$ and $CO_2$ were calculated as 4.6 E-2 and 7.6 E-2, respectively, at the highest temperature.[179] Therefore the measured rates and activation energies in Figure 3.3 and

Table 3.1 should be intrinsic, i.e., characteristic of the reaction kinetics alone.

### 3.3.3. Characterization Results

#### 3.3.3.1. TEM

Four samples were analyzed : Ni0.5/Ce3/Zr, Ni0.24/Co0.24/Ce/Zr, Ni0.3/Co0.3/Ce3/Zr and Ni0.3/Co0.3/Ce3/La. These are all spent (used) samples, after long-term runs in the fixed bed reactor. Therefore, there were variable amounts of carbon (coke). We ignored the filamentous coke in the TEM analysis, although such coke was present in TEM images and according to EDS. The Ni0.24/Co0.24/Ce/Zr and Ni0.3/Co0.3/Ce3/La samples were those contacted with sulfur-containing feed, and so also probably contain some sulfur.

TEM and EDS analyses of the spent Ni-Ce-Zr catalysts indicate a wide range of Ni particle sizes, with some visible ones being too small to measure. We were able to measure the medium- and larger-sized Ni- and Co-containing domains from the EDS maps. An example of the EDS maps is shown in Figure 3.4, with other maps shown in Appendix D (Figure D.2-Figure D.7). The results of the Ni and Co domain measurements for five typical maps (minimum 20 domain measurements) are shown in Table 3.2. The distributions of all elements appear relatively uniform, at least in the main particle.

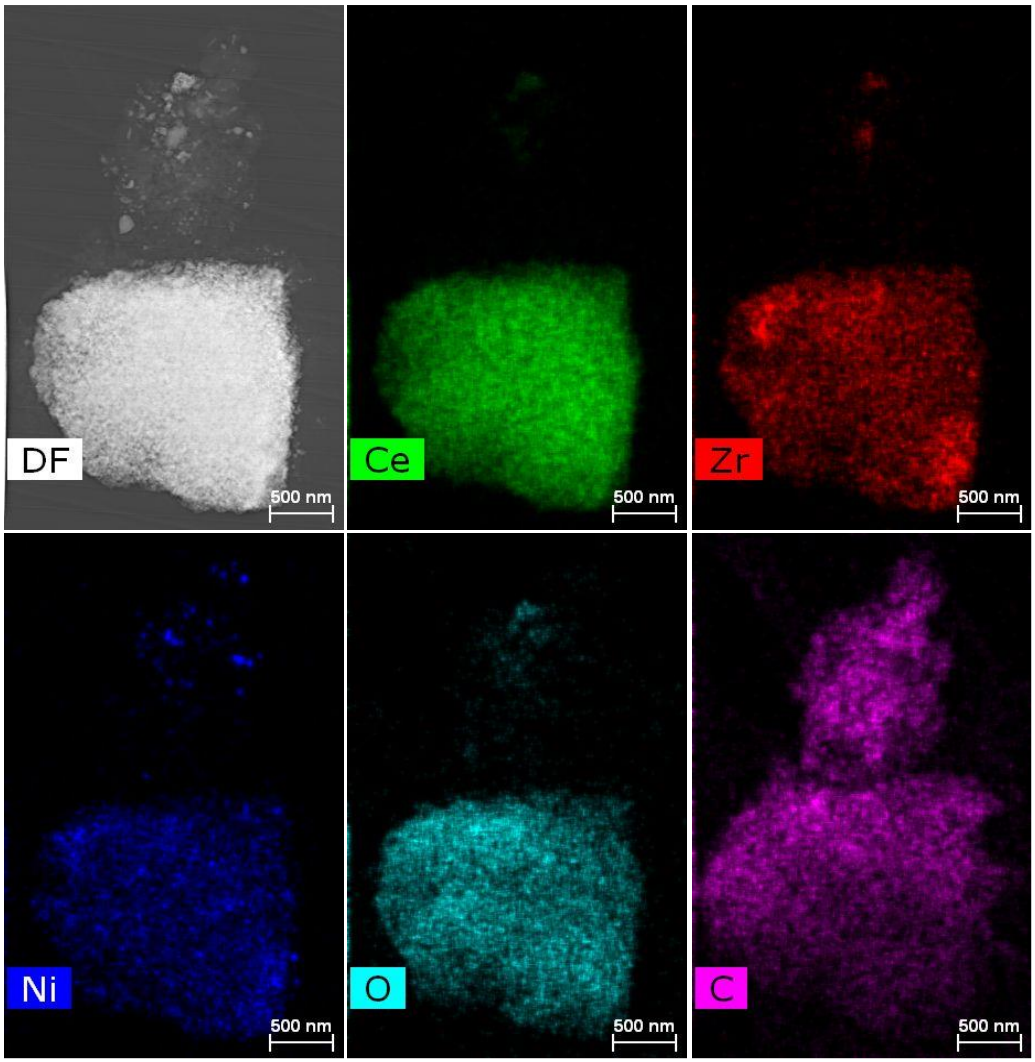

Figure 3.4. EDS maps of a typical spent catalyst particle of Ni0.5/Ce3/Zr, DF = dark field. The images not only show the uniformity of the used catalyst but also the prevalence of carbon. Filamentous carbon attached to the particle has apparently extracted some metals from the particles.

Table 3.2. Ni/Co Domain Measurements from EDS Maps

| Catalyst | Ni Range, nm | Ni Smallest, nm | Co Range, nm | Co Smallest, nm |
|---|---|---|---|---|
| Ni0.5/Ce3/Zr | 26 ± 5 | 19 | | |
| Ni0.5/Ce3/Zr | 28 ± 24 | 12 | | |
| Ni0.24/Co0.24/Ce/Zr | 60 ± 41 | 7 | 156 ± 103 | 59 |
| Ni0.24/Co0.24/Ce/Zr | 40 ± 10 | 20 | 81 ± 35 | 41 |
| Ni0.3/Co0.3/Ce3/Zr | 42 ± 15 | 12 | 103 ± 27 | 55 |

The Ni0.24/Co0.24/Ce/Zr was exposed to 20-30 ppm sulfur for four days. Clearly such exposure has promoted ripening. It appears as if Co has little to no role in limiting the metal particle size, either in non-sulfided or sulfide samples. We superimposed Ni and Co maps to try to determine if the metals were intimately mixed or alloyed with one another. These results are shown in Figure 3.5. There is a high degree of correlation between the Ni and Co in the spent catalysts.

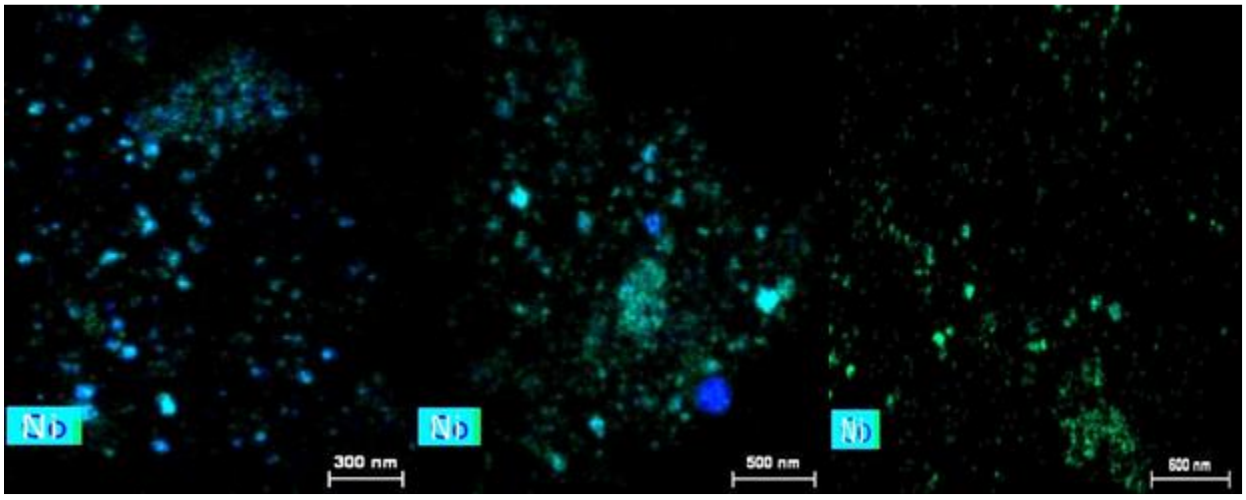

Figure 3.5. Superimposed EDS maps of Ni/Co(Ni blue, Co green) for (L to R): Ni0.24/Co0.24/Ce/Zr, Ni0.24/Co0.24/Ce/Zr, Ni0.3/Co0.3/Ce3/Zr.

We did the same type of superposition for Ce and Zr. The superimposed maps are shown in Appendix D, Figure D.8. These show an even better level of superposition, meaning that there is minimal phase separation of the Ce and Zr oxide, in agreement with previous XRD results.[178]

Multiple TEM images of three different catalysts at high magnification are shown in Figure 3.6-Figure 3.8. Figure D.9-Figure D.11 of Appendix D show higher magnifications for one particle of each catalyst. In Figure 3.6-Figure 3.8, the planes marked "$CeO_2$" are actually for the mixed $CeO_2$-$ZrO_2$ oxide in a distorted fluorite structure. There is some evidence of crystalline Ni/NiO domains in all three spent catalysts. These transition metal domains would include Co/CoO because the lattice d-spacings for Co and CoO are so close to Ni and NiO that they are undistinguishable by this method. Some of the evidence for Ni/NiO and Co/CoO is less certain, because the prominent (220) plane for $CeO_2$-$ZrO_2$ is close in spacing to both the (111) plane for the Ni cubic phase and the (200) for the NiO cubic phase (0.191 nm for $CeO_2$,[183] 0.186-0.192 nm for $CeO_2$-Zr $O_2$ mixed oxide,[155, 184, 185] 0.203 nm for Ni,[186] 0.209 nm for NiO[187]). Where qualification was necessary it is given in the figures. However, there are some images where NiO is clearly present, because its (111) plane is sometimes visible, with a d-spacing (0.241 nm) that does not overlap with any characteristic of $CeO_2$-$ZrO_2$.

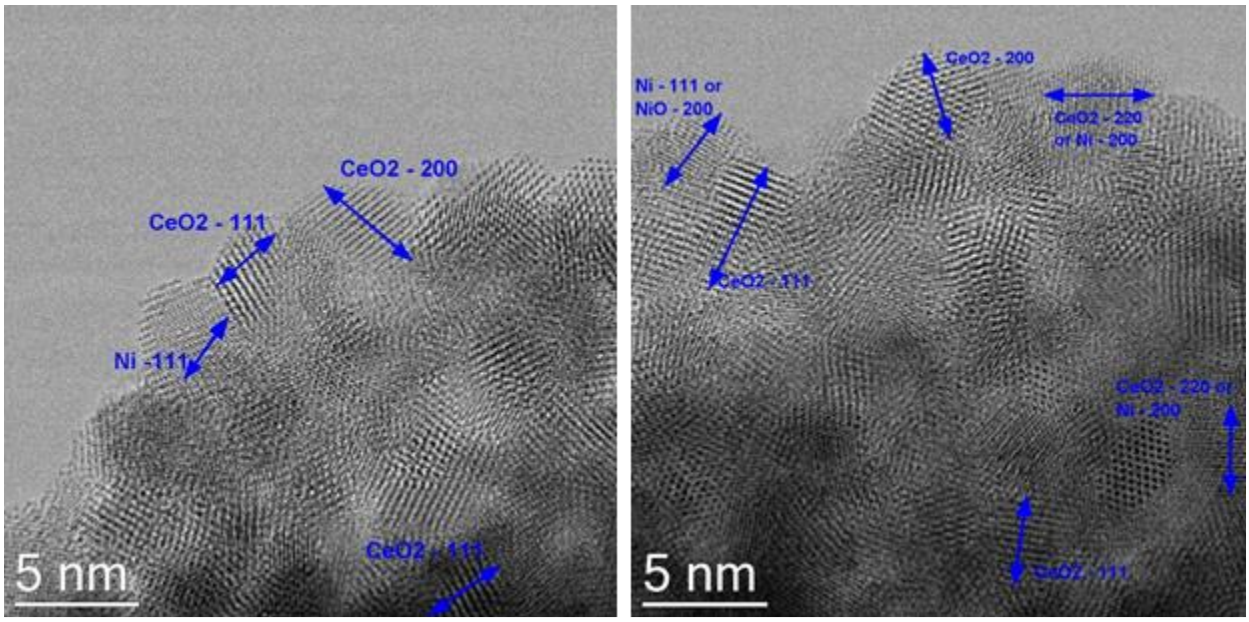

Figure 3.6. TEM images for spent catalyst particles of Ni0.5/Ce3/Zr.

In a bright field image, the $CeO_2$-$ZrO_2$ should appear darker than either Ni(Co) or NiO(CoO) because the atomic weight of Ce is much higher, which means it absorbs more light. The opposite is true for a dark field (DF) image. However, this can be difficult to interpret because shading also depends upon differences in particle location (focal length) and (especially) differences in sample thickness. Planes nearer the outer edge of the particles often appear lighter in dark field only because such particles are thinner near the outer edges. Therefore we judge identity on the basis of lattice spacings only, using multiple images. This evidence for Ce-Zr mixed oxides suggests a mix of Ni and NiO constituting the larger metal aggregates, but with more Ni than NiO for the Ce-Zr supports.

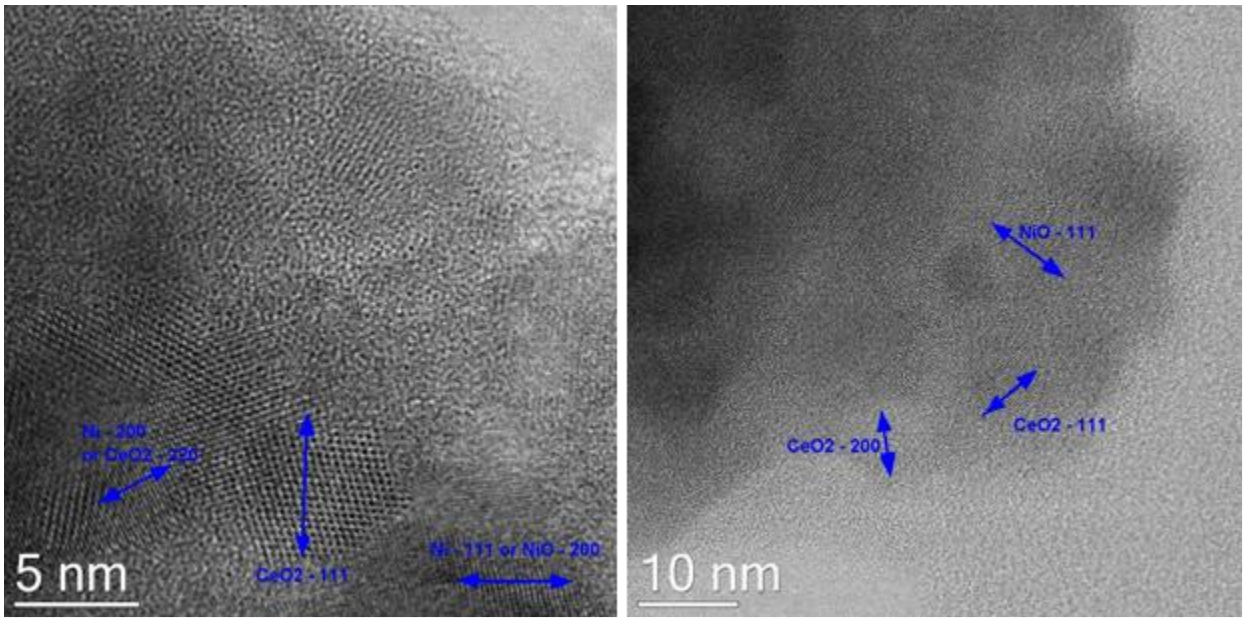

Figure 3.7. TEM images for spent catalyst particles of Ni0.24/Co0.24/Ce/Zr (sulfur treated).

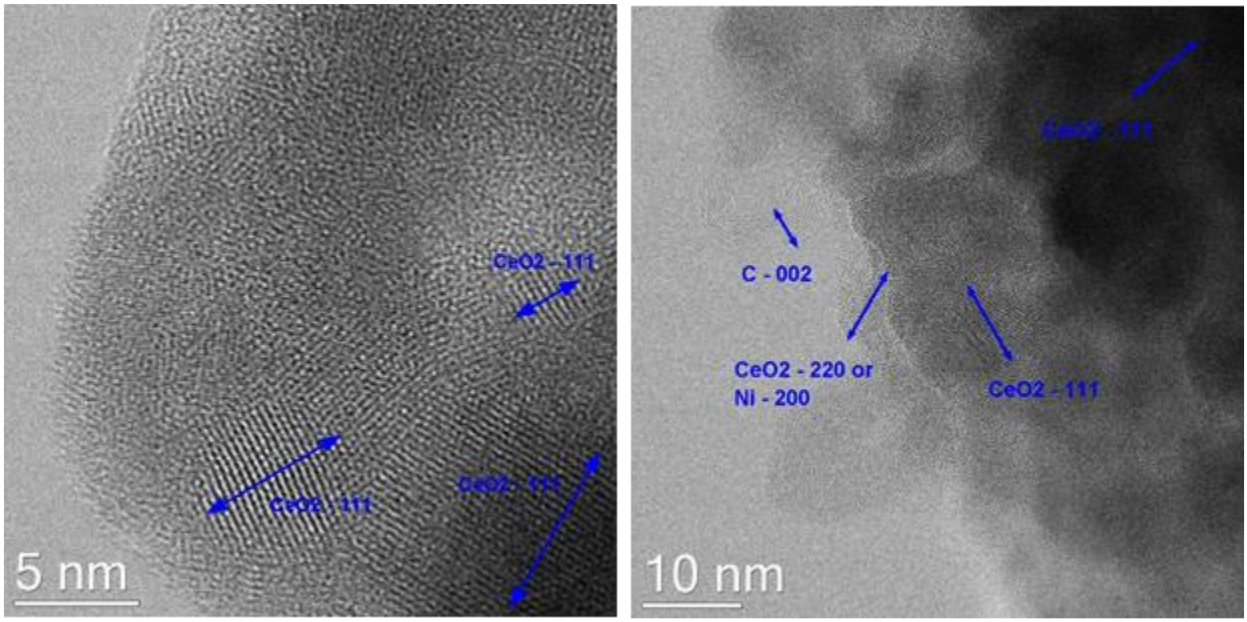

Figure 3.8. TEM images for spent catalyst particles of Ni0.3/Co0.3/Ce3/Zr.

Figure D.9-Figure D.11 show TEM images of typical particles for three spent catalysts. What is apparent is that while a range of particle sizes exist, there do not appear to be differences in appearance for the particles, other than in how much filamentous carbon is extending from

them. Because these catalysts were used over differing durations (Ni0.24/Co0.24/Ce/Zr the longest, for roughly 10 days), it is not surprising that variable amounts of carbon have been deposited. The similarity of the TEM images for different particles suggests that the high magnification images shown are characteristic of the materials.

For the Ni0.3/Co0.3/Ce3/La catalyst, the TEMs show evidence of the mixed oxide and some NiO particles. Two typical high magnification images (as high as this machine could image) are given in Figure 3.9. The measurable lattice fringes are actually 2λ and 3λ spacings. Most of them are characteristic of the $CeO_2$-$La_2O_3$ mixed oxide (111) plane, 0.313-0.318 nm, or the (200), 0.275-0.280 nm.[112, 134] The observed NiO plane is the dominant (100).

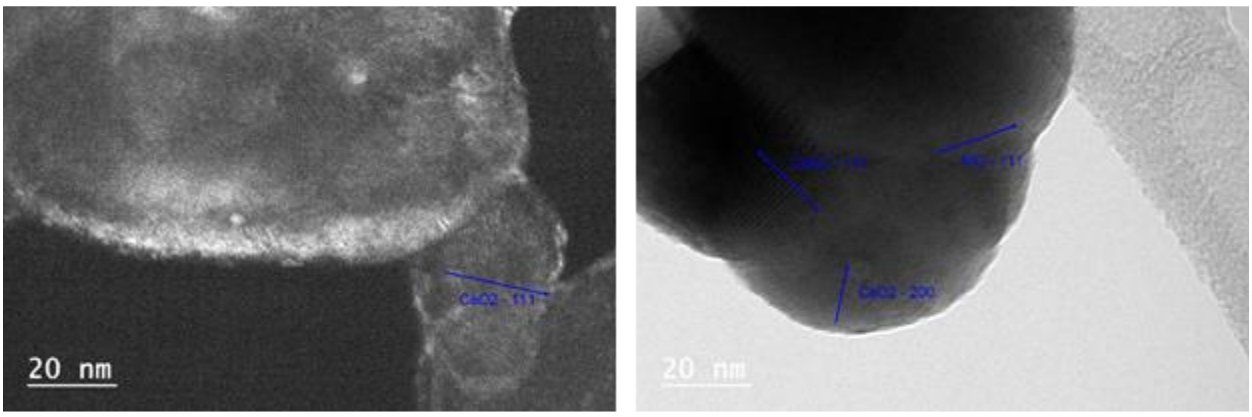

Figure 3.9. TEM images for spent catalyst particles of Ni0.3/Co0.3/Ce3/La.

We measured CO chemisorption at 25°C (Table 3.3) just as a check on the TEM results. The results show that significant ripening did indeed take place during the reaction, and that the final metal surface aggregates were large, characterized by low dispersion. For fcc Ni(0), a 1% dispersion is roughly consistent with 100 nm spherical particles, assuming a typical Ni atomic surface area.[188] However, CO won't adsorb on NiO at 25°C, so the measured dispersions are

skewed lower by the presence of some oxidized Ni, the presence of which is suggested both by the TEM data above and the XPS and XAFS data below.

Table 3.3. CO chemisorption results for fresh and spent catalysts.

| Designation, Molar Ratios | State | % Dispersion |
|---|---|---|
| Ni0.5/Ce3/Zr | fresh | 7.3 |
| Ni0.5/Ce3/Zr | spent | 0.82 |
| Ni0.24/Co0.24/Ce/Zr | fresh | 2.8 |
| Ni0.24/Co0.24/Ce/Zr | spent | 0.2 |
| Ni0.2/Co0.2/Ce/Zr | spent | 0.55 |
| Ni0.3/Co0.3/Ce3/La | spent | 0.2 |

### 3.3.3.2. XPS

O1s XPS results for spent catalysts are shown in Figure 3.10. The peaks at ~530.5, 531.5 and 533 eV are attributed to lattice oxygen ($O_\alpha$), surface adsorbed oxygen such as in $O^-$ or $OH^-$ ($O_\beta$), and the oxygen in adsorbed water, respectively.[189] The $O_\beta$ peak provides information on surface adsorbed oxygen into the oxygen vacancies.[190] The fitting results are shown in Table D.1, Appendix D. Ni0.15/Ce2/Zr, with the lowest Ni+Co content, gives the lowest $O_\beta/ (O_\alpha + O_\beta)$ ratio. This suggests fewer vacancies. The fourth peak at ~535-537 eV, which doesn't show up in the fresh catalysts (spectra in Figure D.12), is likely due to oxygen adsorbed on graphitic carbon.[191] For Ni0.15/Ce2/Zr, the fourth peak is at 534.4 eV, attributed to the C-O-C group,[192] an assignment which is consistent with a peak at ~286 eV in the C1s spectrum.

Note that two of the four catalysts in Figure 3.10 were sulfided, extensively. The spent catalysts were not further treated to remove any sulfur. Yet there was no evidence of sulfur in the S 2p XPS.

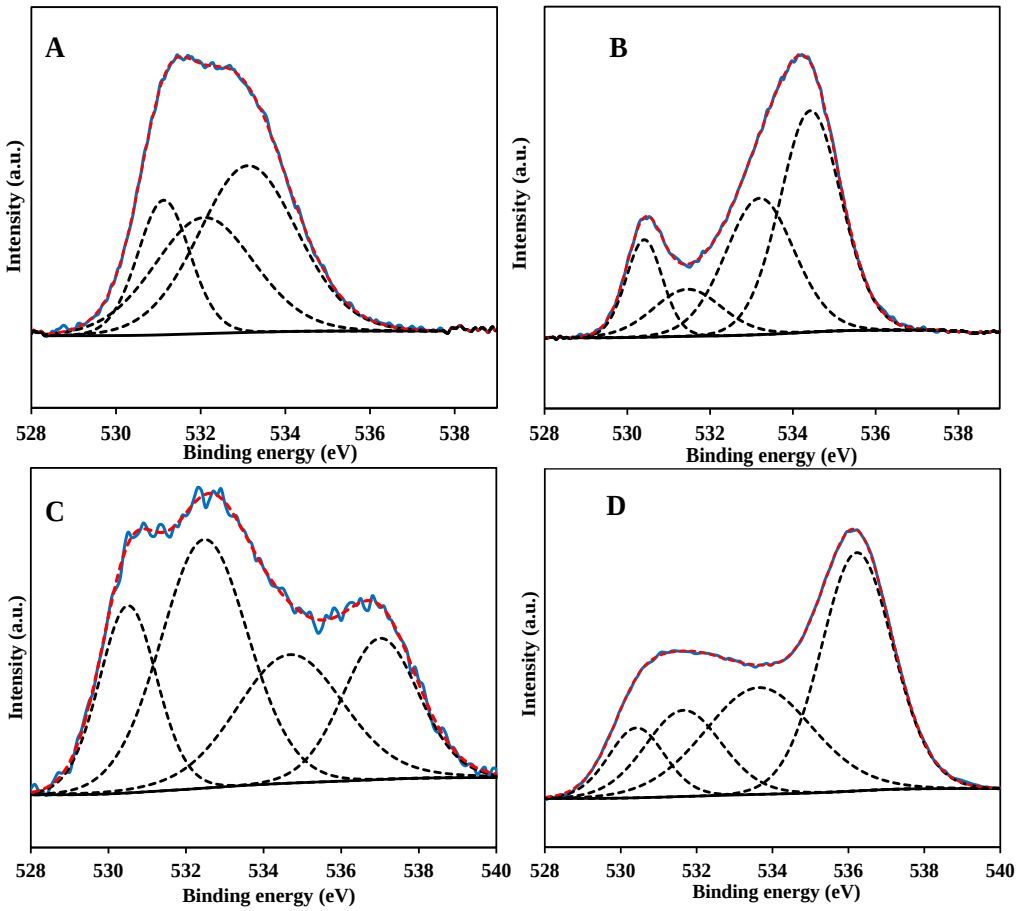


Figure 3.10. O1s XPS of spent catalysts. Solid blue lines are experimental, dotted black lines are the deconvoluted spectra, dotted red lines are the linear combination fits, and solid black lines the backgrounds. A- Ni0.24/Co0.24/Ce/Zr (sulfided) ; B- Ni0.15/Ce2/Zr (sulfided) ; C- Ni0.5/Ce3/Zr ; D- Ni0.3/Co0.3/Ce3/Zr.

The Ni 2p 3/2 spectra are shown in Figure 3.11, with the largest peak near 855 eV characteristic of $Ni^{2+}$. For the fresh Ni0.3/Co0.3/Ce3/Zr catalyst the deconvoluted spectrum shows a small peak at 851.6 eV (green dotted line) distinct from the main $Ni^{2+}$ peak at 855.5 eV (orange dotted line) and an uptake satellite peak at 861eV. The small peak at 851.6 eV indicates the existence of some $Ni^{0}$. The location of the main $Ni^{2+}$ peak at 855.5 instead of 853.4 eV (pure NiO) indicates that these $Ni^{2+}$ species were in the Ce/Zr oxide.[102, 109, 154, 193] Compared to the fresh catalysts, the $Ni^{2+}$ peaks in spent catalysts shift to an even higher binding energy (~+2 eV),

which suggests an even stronger interaction with the oxide. However, the peak intensities of spent catalysts are much lower, which can be due to either or both particle sintering or coking. These intensities are so low that it would be impossible to identify $Ni^0$ from these spectra – even the $Ni^{2+}$ peak is barely visible.

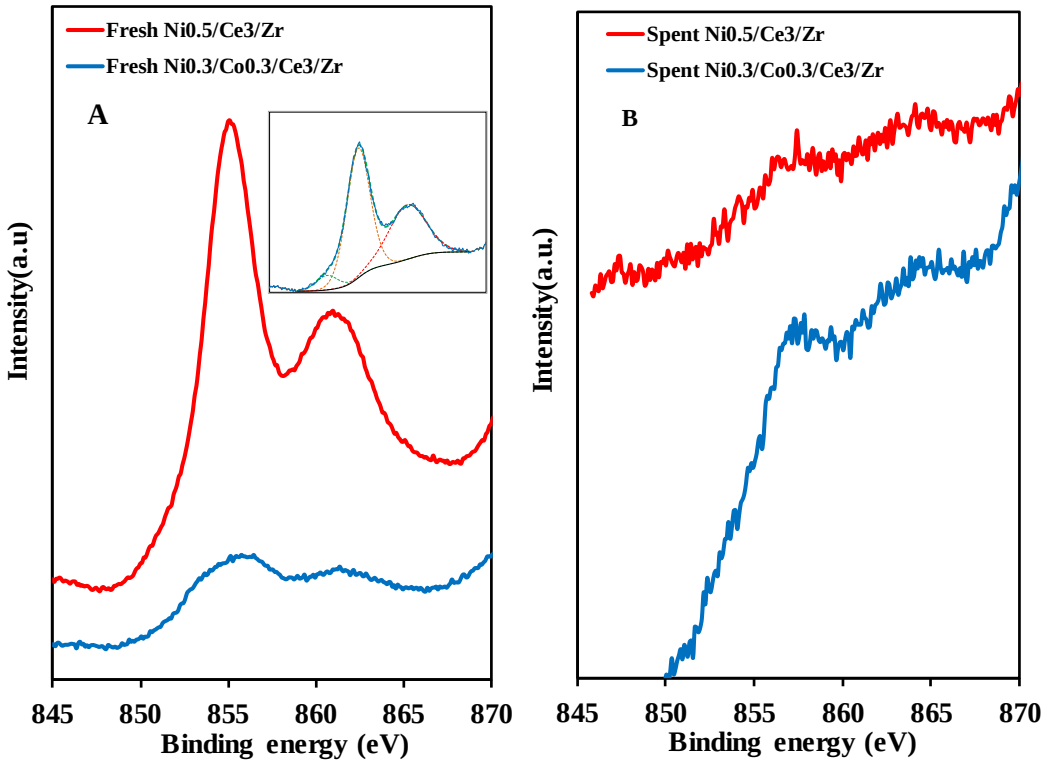


Figure 3.11. Ni 2p 3/2 XPS of fresh and spent catalysts.

Figure D.13 shows the Co2p 3/2 core level spectra of fresh and spent Ni0.3/Co0.3/Ce3/Zr, which can be deconvoluted into three peaks, $Co^0$ at ~778 eV , $Co^{2+}$ at ~781 eV and the $Co^{2+}$ satellite peak at ~786 eV.[194] Metallic Co doesn't have a satellite peak.[195,196] The metallic Co in the fresh catalyst is partly oxidized during reaction, because the first peak shifts to a higher binding energy but does not disappear entirely. Figure D.14 shows the Co 2p

3/2 XPS of spent Ni0.24/Co0.24/Ce/Zr. The prominent peak and its satellite also suggest most of the Co is $Co^{2+}$.

The C 1s spectra of spent catalysts are shown in Figure D.15. There are peaks at binding energies higher than the normal graphitic carbon at 284.8 eV. For example, for spent Ni0.3/Co0.3/Ce3/Zr and Ni0.5/Ce3/Zr there is a strong peak at 288 eV. This peak is assigned to the carbonyl group (C=O).[197] For Ni 0.2/Co0.2/Ce/Zr, the peak appears at ~289 eV, which can arise from carboxylate carbon (O–C=O).[197-199] The peak at ~284.8 eV is the most prominent, suggesting graphite is still the main form of carbon among all the spent catalysts. The small peak at 283-284 eV reveals the existence of some nickel carbide in spent Ni0.24/Co0.24/Ce/Zr.[200] The spectrum for Ce 4s partly overlaps with C 1s; the broad weak peak at ~291 eV is probably due to multiple Ce 4s peaks.[201]

**3.3.3.3. XAFS**

XAFS spectra were taken in order to further explore the Ni coordination environment and how it changes during DRM. The spectra of spent catalysts and Ni foil are shown in Figure 3.12. The prominent peaks in all spent Ce/Zr catalysts can be assigned to Ni-Ni scattering with Ni in its mostly metallic form. We did not attempt to distinguish Ni-Ni from Ni-Co scattering in the fits; the structural and electronic similarities in Ni-Co alloys vs. Ni or Co alone would make this difficult if not impossible. The intensity of these peaks (Figure 3.12) and the regressed coordination numbers (shown in Table 3.4) are both less than that of Ni foil, suggesting that most of the Ni exists as dispersed clusters where a large amount of Ni is coordinatively unsaturated. For pure Ni foil, the 1$^{st}$ through 4$^{th}$ shell coordination numbers (N's) would be 12, 6, 24, and 12, respectively.

The Ni-Co-Ce-Zr spent catalysts show less coordinatively unsaturation of Ni than the other spent catalysts, or the fresh catalysts (Table 3.4). For all of the others, the amount of coordinative unsaturation is significant and outside the uncertainty range of the fitted N-values. Because Ni and Co scattering cannot be differentiated in the XAFS, this result supports the hypothesis that Ni and Co become more alloyed upon use in the DRM reaction.

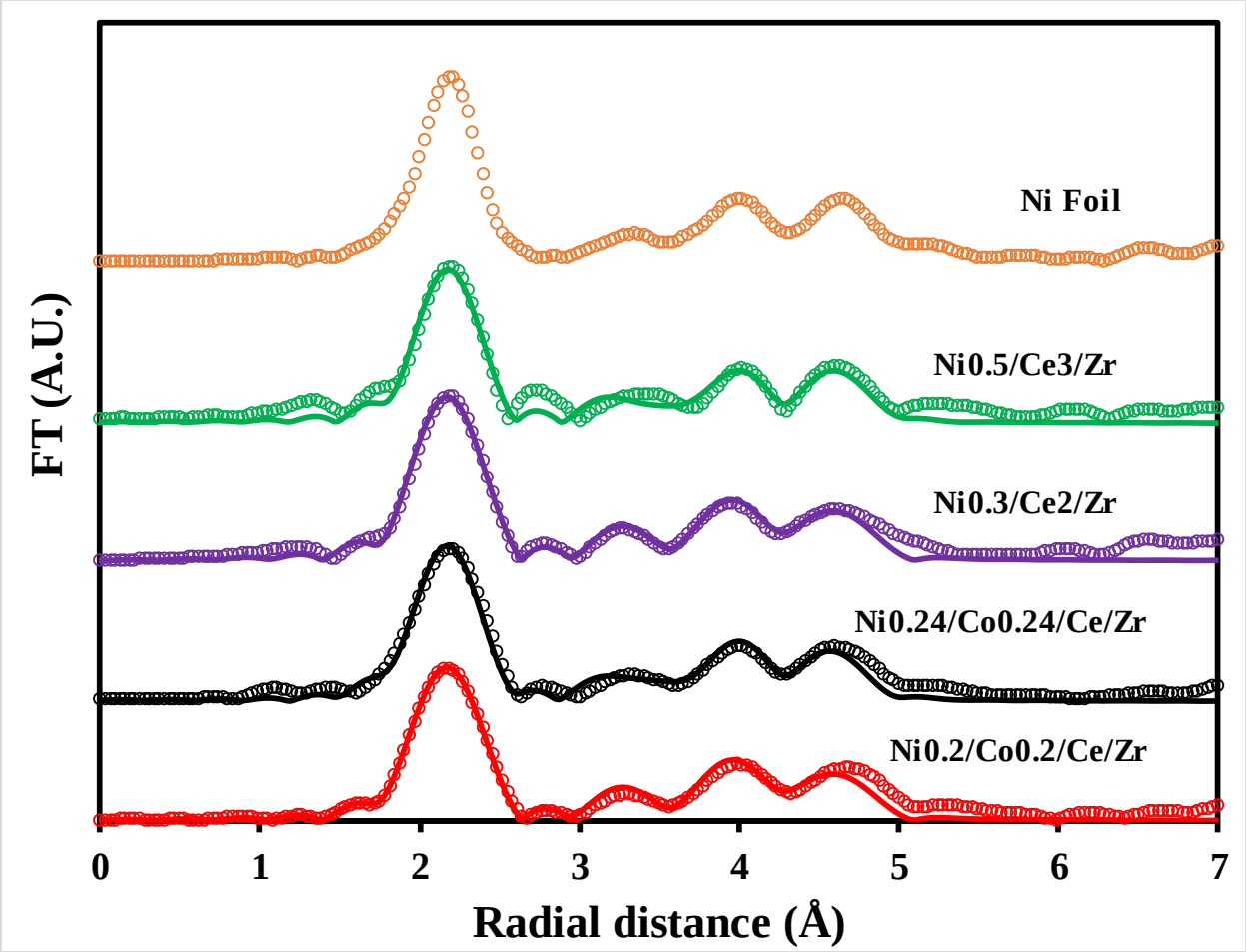


Figure 3.12. Fourier-transformed XAFS (circles) and the theoretical fit for the spent Ce/Zr to structures described in Table 3.2 (solid lines). The fitting range in R space is 1-5 Å.

Table 3.4. EXAFS fitting results for fresh and spent catalysts.[a]

| Sample | State | Shell | N | σ2 (Å2) | R (Å) | R-factor |
|---|---|---|---|---|---|---|
| Ni0.2/Co0.2/Ce/Zr | Spent | 1st Ni-Ni | 11.8±0.3 | 0.0063±0.0003 | 2.47±0.002 | 0.018 |
| | | 2nd Ni-Ni | 5.9 | 0.0081 | 3.50 | |
| | | 3rd Ni-Ni | 23.6 | 0.0081 | 4.31 | |
| | | 4th Ni-Ni | 11.8 | 0.0081 | 4.84 | |
| Ni0.3/Ce2/Zr | Spent | 1st Ni-Ni | 11.1±0.3 | 0.0054±0.0002 | 2.48±0.002 | 0.017 |
| | | 2nd Ni-Ni | 5.6 | 0.0077 | 3.50 | |
| | | 3rd Ni-Ni | 22.3 | 0.0077 | 4.30 | |
| | | 4th Ni-Ni | 11.1 | 0.0077 | 4.85 | |
| Ni0.24/Co0.24/Ce/Zr | Spent | 1st Ni-Ni | 11.9±0.4 | 0.0065±0.0003 | 2.48±0.002 | 0.026 |
| | | 2nd Ni-Ni | 6.0 | 0.0086 | 3.50 | |
| | | 3rd Ni-Ni | 23.8 | 0.0086 | 4.31 | |
| | | 4th Ni-Ni | 11.9 | 0.0086 | 4.84 | |
| Ni0.24/Co0.24/Ce/Zr | Fresh | 1st Ni-Ni | 11.0±0.3 | 0.0062±0.0003 | 2.48±0.002 | 0.027 |
| | | 2nd Ni-Ni | 5.5 | 0.0085 | 3.51 | |
| | | 3rd Ni-Ni | 22.0 | 0.0085 | 4.31 | |
| | | 4th Ni-Ni | 11.0 | 0.0085 | 4.86 | |
| Ni0.5/Ce3/Zr | Spent | 1st Ni-Ni | 9.2±0.3 | 0.0050±0.0003 | 2.47±0.003 | 0.032 |
| | | 2nd Ni-Ni | 4.6 | 0.0076 | 3.49 | |
| | | 3rd Ni-Ni | 18.4 | 0.0076 | 4.29 | |
| | | 4th Ni-Ni | 9.2 | 0.0076 | 4.86 | |
| Ni0.3/Co0.3/Ce3/La | Spent | 1st Ni-O | 5.5±0.1 | 0.0050±0.0006 | 2.07±0.004 | 0.016 |
| | | 1st Ni-Ni | 11.0±0.1 | 0.0064±0.0003 | 2.96±0.002 | |
| | | 2nd Ni-O | 7.3 | 0.0138 | 3.51 | |
| | | 2nd Ni-Ni | 5.5 | 0.0075 | 4.29 | |
| | | 3rd Ni-O | 22.0 | 0.0138 | 4.62 | |
| | | 3rd Ni-Ni | 22.0 | 0.0075 | 5.15 | |

[a]N is the coordination number. $\sigma^2$ is the Debye–Waller factor, R is the Ni–O or Ni–Ni distance. The uncertainty in the structural parameters for the first shell obtained from XAFS fitting were output from Artemis are given for N, $\sigma^2$ and R.

A comparison between fresh and spent Ni0.24/Co0.24/Ce/Zr is shown in Figure D.16. Both Ni foil and NiO powder have been used as reference spectra. The main peaks in both samples can be assigned to Ni-Ni scattering. However, the fresh catalyst is more coordinatively unsaturated, which is consistent with the smaller metallic cluster/aggregate sizes of the fresh catalysts suggested by both the CO chemisorption and XPS. However, all of the Ce/Zr catalysts

remain coordinatively unsaturated to some degree, and to a large degree for the Ni-only catalyst (Table 3.4). The oxidation of the Co during reaction, evident in the XPS results, may have a role in reducing the Ni in these catalysts.

However, the Ni in the spent Ce/La catalyst exhibits a completely different state. Figure D.17 shows the XAFS of spent Ni0.3/Co0.3/Ce3/La. The peak at 1.8 Å can be assigned to Ni-O scattering and the second major peak corresponds to Ni-Ni scattering. The Ni-Ni peak at ~ 4.8 Å has shifted to a slightly higher distance relative to that of NiO powder. Therefore these catalysts present an entirely different and more oxidized structure where most of the Ni remains in the CeO2-ZrO2 mixed oxide. The result (and the Ni-O coordination number) is similar to what has been found for active nickel aluminate catalysts[180].

## 3.4. Discussion

### 3.4.1. Origin of Sulfur Tolerance

At low sulfur concentrations in the feed, all catalysts tested here are fairly stable. The Ni-only catalysts show some deactivation, but they do so even when sulfur is not present (Figure 3.1), so this is not due to sulfur poisoning. But in a high sulfur concentration environment (20-30 ppm), only catalysts where Ni is paired with Co, and Ce with Zr, and the Ce/Zr ratio is high (1:1) can survive over the long term (Figure 3.2). The addition of Co in particular is crucial to the sulfur tolerance. Simpler catalysts such as $Ni/Al_2O_3$ deactivate rapidly even in 10 ppm sulfur at similar conditions.[202] However, Misture et al. observed similar excellent sulfur tolerance for DRM using a $Ni_{0.375}Co_{0.375}Mg_{0.25}Al_2O_4$ spinel-based catalyst synthesized at 1500°C.[88] They hypothesized that the sulfur tolerance is related to the highly oxygen-defective spinel support that results after such high temperature pretreatment. Oxygen defects provide sites for the

activation of $CO_2$, which when reduced to CO supplies active oxygens that react with and so remove surface carbon.[14, 21, 86, 93, 94, 96, 99-101, 107, 147, 203, 204] But such sites could do the same for oxidative sulfur removal. This is only a partial explanation of the origin of sulfur tolerance, however, because it cannot explain why Ni0.3/Co0.3/Ce3/La and the Ni-only catalysts deactivated completely in a high concentration sulfur environment; the Ce/La support is at least as effective in creating oxygen vacancies as Ce/Zr supports,[136, 178, 205] and many such vacancies in either oxide can be at or near the surface.[65, 103-106, 108, 203, 205, 206] It is also unrealistic to expect the spinel-based catalysts not to undergo the metal particle ripening and reduction under DRM conditions, as observed here.

Our evidence points to Ni-Co alloying as another key to sulfur tolerance, along with the presence of high oxygen vacancy concentrations. The TEM data suggest that such alloying occurs, the XPS data show that much of the Ni migrates or exsolves to larger aggregates, with more of the Ni becoming reduced. The XAFS results confirm that Ni in the metal aggregates is closer to zero-valent. The main difference between the catalysts based on Ce/Zr oxides and the one based on the Ce/La oxide is that the latter keeps more of its Ni in at a fully $Ni^{2+}$ state, and there is less exsolved Ni to poison. The possibility of poorer alloying with the Co in Ce/La oxide can also not be excluded.

The strongest proofs of Ni-Co interaction as an alloy or metal mixture under DRM conditions are of course its behavior in the presence of sulfur, the lower coking rates for Ni-Co catalysts at low conversion conditions measured both previously[178] and in Table 3.1, and the lower rates of deactivation in the absence of sulfur (Figure 3.1). With sulfur present at 20-30 ppm, Ni-only catalysts deactivate fully at contacting times where the molar amounts of sulfur passed over the catalysts is similar to the mols Ni present in the catalyst (Figure 3.2), while

certain Ni-Co-Ce-Zr catalysts were stable beyond this limit. The electronic modifications of the Ni in the metal aggregates caused by Co must hinder adsorption of $H_2S$. The simple experiment where we used a sulfur meter to check the breakthrough of $H_2S$ to the exhaust showed almost three times higher $H_2S$ levels for Ni0.24/Co0.24/Ce/Zr than for a Ni-only catalyst. From Figure 3.2 it is seen that for this catalyst neither the DRM nor the reverse water gas shift activities of the catalyst were affected. We also confirmed that coking was less in these runs, because standard temperature-programmed oxidation with air gave only 0.16 mg carbon/mg catalyst in 10 days total usage, while Ni0.5/Ce/Zr accumulated 0.34 mg carbon/mg catalyst in 5 days.

### 3.4.2. What Are the Active Sites for DRM?

The characterization results do not present a simple consistent picture on where the active DRM sites are. While there is no doubt that there are large Ni/Co metal aggregates present in spent catalysts, and while it appears that in these aggregates the Ni is close to its zero-valent form on a Ce-Zr support (although less so on a Ce-La support), nevertheless the relevance of the large aggregates to the DRM reaction is questionable. XPS indicates little Ni(0) present in the fresh catalysts, which is consistent with previous XRD work.[178] The only Ni present is either $Ni^{2+}$ doped into the oxide lattice (most of it) and Ni present in smaller crystallites. We know these initial aggregates are much smaller both from the XAFS results (for Ni0.24/Co0.24/Ce/Zr), showing extensive coordinative unsaturation in the fresh catalyst (Table 3.4), and the CO chemisorption results. But the catalysts are almost immediately active – in the DSC/TGA low conversion tests they are within 10% of full activity in 30 min or less, and this is the time over which the surface intermediates build to their steady-state values, as determined by the weight changes. Combined with the positive and long-lasting effects of pre-oxidation on catalyst

activity (an example of which is shown in Figure 3.1), this time is probably associated with slight changes in metal oxidation states starting from the freshly reduced catalysts.

The evidence therefore suggests that the active sites for methane activation must either be interfacial Ni-metal sites or those present in the small metal aggregates present at the start of the reaction, and that the active sites are more coordinatively unsaturated than bulk Ni metal and stabilized by the oxide. Smaller aggregates would contain a much higher percentage of sites at the rare-earth oxide interface. This conclusion is in broad agreement with the work and mechanistic proposals of others on both similar[108, 147, 204, 207-209] and dissimilar[210, 211] DRM catalysts. While both $CH_4$ and $CO_2$ activation can also take place on a Ni-only catalyst if different oxidation states of Ni are initially present, such catalysts are incapable of long-term stability on practical feeds.[35] Figure 3.13 (adapted from Figure 8, Liang et al.[212] with permission) summarizes pictorially how and where the activations of the two reactants take place.

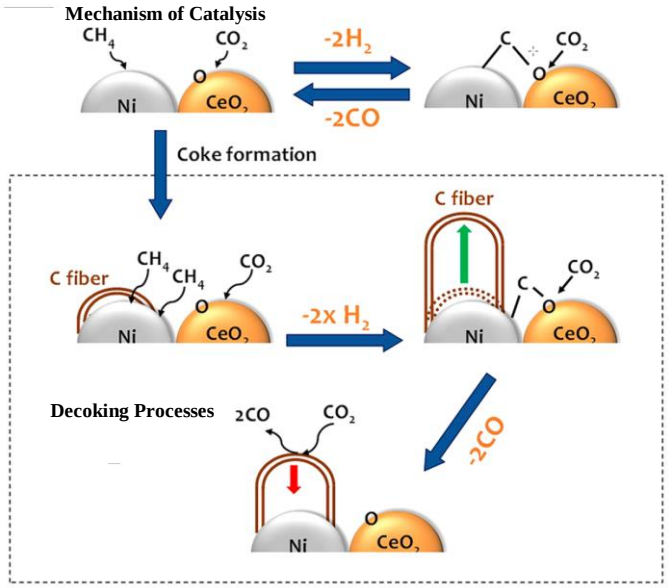


Figure 3.13. An illustration of carbon buildup on a catalyst (coking) with removal through activation of $CO_2$ on $CeO_2$

### 3.4.3. Is There Kinetic Evidence That the Oxide Sites Are Involved in DRM?

In Section 3.4.1 we summarized the evidence for how defect (oxygen vacancy) sites in the rare earth oxides could participate in the mechanism through activation of $CO_2$. If this supposition is true, then there should be a significant difference in overall activation energy between catalysts where such vacancy formation is likely, and other DRM catalysts. Also, because the activation of $CO_2$ or the desorption of CO in the simpler catalysts is considered a kinetically slow step,[35, 210] the observed activation energy ($\Delta E$) for the catalysts with higher vacancy concentrations should be lower. We note that DFT calculations estimate the activation energy to dissociate $CH_4$ as 124 kJ/mol on $CeO_2$ (111), but by the same methods -59 kJ/mol on Ni-doped $CeO_2$ (111).

The $\Delta E$'s over several different DRM catalysts are shown in Table 3.5. The $\Delta E$'s for our catalysts are between 50-58 kJ/mol (Table 3.1). From these data, two different groupings are evident, high (>104 kJ/mol) and low (<80 kJ/mol) ranges. What looks to distinguish these ranges is that the former was determined for catalysts either without the capacity to generate high oxygen vacancy concentrations, or where the temperature range was too low to do so. This suggests that the support's ability to activate $CO_2$ independently of the transition metal sites is important in DRM and that the best catalysts will exhibit this functionality.

Table 3.5. Comparison of apparent activation energies (ΔE, kJ/mol) over DRM catalysts

| Measured ΔE kJ/mol | P range （Kpa） | T range (◦C) | $CH_4/CO_2$ ratio | Catalyst | Ref |
|---|---|---|---|---|---|
| 54 | 101.3 | 600-800 | $CH_4$:$CO_2$:$N_2$ = 1:1:3 | Ni-K/$CeO_2$-$Al_2O_3$ | 10 |
| 147 | | 620-690 | | Ni/CaO/$Al_2O_3$ | |
| 113 | | 400-550 | | Ni/$SiO_2$ | |
| 134 | | 400-550 | | Ni/C | |
| 146 | | 400-550 | | Ni/MgO | |
| 67-79 | 101.3 | 580-780 | 1:1 | Ni/$CeO_2$-$ZrO_2$ | 14 |
| 54.5,56.4 | 110 | 650-750 | 1:0.75- 1:2.5 | 5Co–15Ni/$Al_2O_3$ | 12 |
| 46.7-46.9 | 110 | 650-750 | 1:0.75- 1:2.5 | Lanthanides / Co–Ni/$Al_2O_3$ | 93 |
| 105 | 100–1500 | 550-750 | 1:1 | Ni/MgO | 213 |
| 41.4-48.9 | 101.3 | 550-800 | 1:1 | Ni−Ce−Al Oxide | 214 |
| 32, 32.5 | 100 | 650–850 | 1:1, 1:2 | $Ni_{0.75}Mg_{0.25}Al_2O_4$ | 88 |

### 3.5. Conclusions

1) Extended sulfur tolerance in Ni-based DRM catalysts at the 20-30 ppm level can be attained by the addition of Co, and supporting the metals on mixed rare earth oxides such as Ce-Zr oxide, that exhibit high concentrations of oxygen defect sites. Extended sulfur tolerance at <1 ppm is possible with both Ce-Zr and Ce-La oxides, and without Co.

2) In catalysts containing both transition metals, at least some of the Co is alloyed with the Ni. The combination reduces the rate of coking even further, to the point that there is almost no observable coking rate.

3) While large Ni/Co aggregates (with the Ni nearly zero-valent) are formed during long-term DRM reaction, and are present in spent catalysts, these are spectators. Interfacial sites closely associated with the mixed oxide, and exhibiting some coordinative unsaturation, are the reaction loci for methane activation.

4) Activation energies measured over a wide temperature range at low conversions support the hypothesis that $CO_2$ activation takes place at the oxide interface.

5) While $CeO_2$-$La_2O_3$ mixed oxide is a good support for Ni-based DRM catalysts in the absence of sulfur, the relatively lower Ni surface concentrations limit its utility when sulfur is present in the feed. More of the Ni remains buried as $Ni^{2+}$ within the oxide.

# APPENDIX A. EXPERIMENTAL PROCEDURES – REACTOR TESTING

## A.1. Dry Reforming Experiments

A schematic of the reactor system is shown as Figure A1. It includes four electronic mass flow controllers to prepare the gas mixture, a Harvard 944 infusion pump to supply a water/dimethyl sulfoxide (DMSO) solution from a calibrated syringe, a ½" stainless steel reactor tube packed with α-alumina and either 0.5 or 0.25 g of catalyst, and an online Agilent 6890N GC-MS to analyze the gas composition. The reactor tube is heated by a furnace (Teco F-5-1000, 320 watt) whose temperature was controlled by a Eurotherm 818P PID controller. Additional K thermocouples are placed on heated lines carrying the gases to and from the reactor. The sampling valves (GSVs) inside the GC are Valco 10-port; the switching valves outside the GC are Valco 6-port and 8-port.

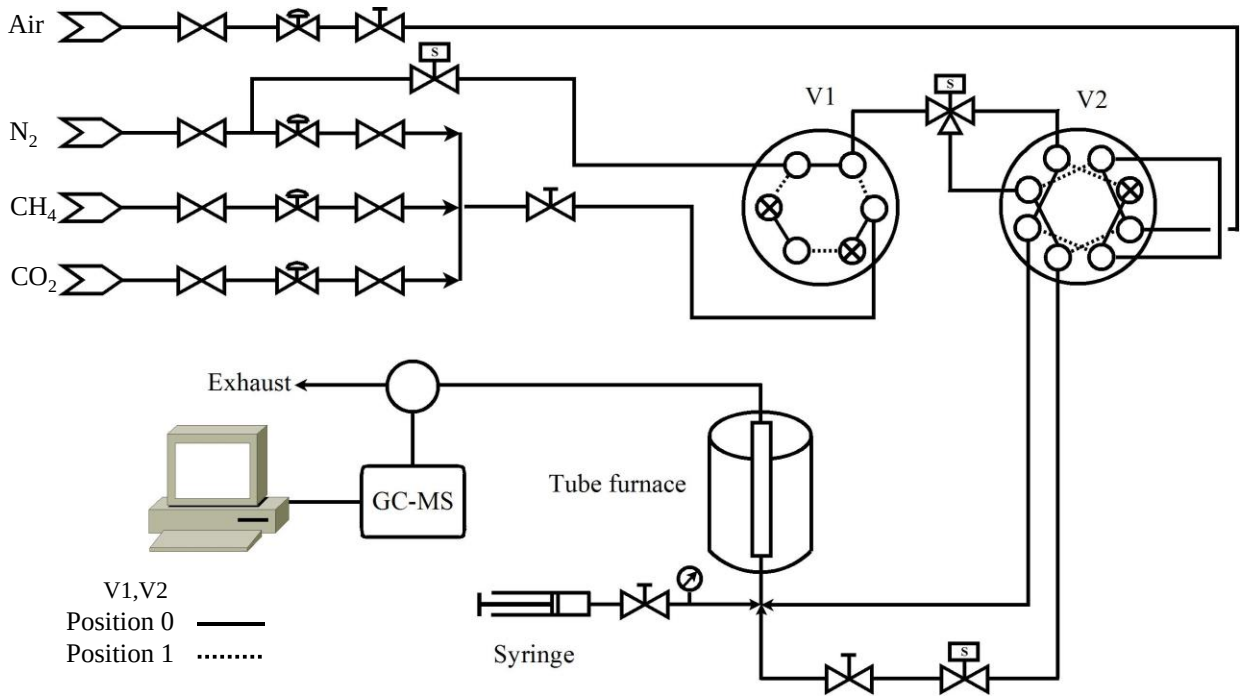


Figure A.1. Schematic of reactor system for DRM. Position 0 is for normal operation and position 1 is for air pretreatment or regeneration

After the DRM experiments, the reactor was cooled in flowing $N_2$ and the catalyst isolated immediately for use in post-mortem characterizations. The sulfur was supplied to the reactor in the form of aqueous DMSO (12.1 mL DMSO/L). The solution was injected into the feed line from a calibrated 5 mL Hamilton syringe using a dual infusion/withdrawal pump (Harvard Apparatus, Model 944). The lines were heated above 100°C so that the solution would be gasified. It was verified that the DMSO decomposed in the reactor to a mixture of $H_2S$ and S in the reactor by testing the exhaust for $H_2S$/sulfur, using a sulfur analyzer (Industrial Scientific TMX412).

**A.2. Reactor Operating Procedures**

1. Load catalyst from the bottom. Fill bottom and top of reactor with $\alpha$-$Al_2O_3$ and quartz wool.
2. Purge the system with $N_2$ at least for 10 min.
3. Bring the reactor temperature to the target, and all feed and product lines above 100°C.
4. Pretreat the sample with either $N_2$, 5%$H_2$/$N_2$ or Air overnight.
5. Purge the system with $N_2$ again at least for 10 min.
6. Bring the reactor temperature up to the operating temperature.
7. Switch from $N_2$ to the reaction feed. Gas flows are controlled and measured by the mass flow controllers, with flow rates recorded using the LabVIEW software. The total outlet flow rates were measured by bubble meter.
8. Inject water or aqueous DMSO into the system from the syringe pump, if desired.
9. Set up a GC sequence to take samples automatically.
10. Switch the reacting gases to $N_2$ after the experiment finished. Turn off the syringe pump and lower the temperature for the reactor and lines.

## A.3. TGA/DSC Experiments – Calculating Conversions and Rates

Taking the DSC data at the endothermic plateau, we can estimate the fractional conversion of $CH_4$ and its rate of DRM. The following approximation was made: reforming reaction >> (sum of coking and reverse water-gas shift reactions). The fraction conversion equation is:

$$\text{Calculated heat flow} = \Delta H_R \times F_{in,CH4} \times X_{CH4}$$

where $\Delta H_R$ is the enthalpy change for DRM, and $F_{in,CH4}$ is the molar flow rate of the inlet $CH_4$. Calculations for $X_{CH4}$ and all thermodynamic calculations were performed in ASPEN-HYSYS®. The $X_{CH4}$ was varied until the calculated heat flow matched the experimental (DSC) heat flow. From ASPEN-HYSYS, the endothermic heat effect for DRM at 660-800°C was estimated as 7.2-7.5 times that of the heat effect for the reverse water-gas shift (RWGS, also endothermic but far less so), further justifying the approximations. Since the conversions are small, the differential approximation applies and the initial reforming rates (*r_reforming*, in mmol/(mg•h)) can be calculated as follows:

$$r\_reforming = \frac{F_{in,CH4} \times X_{CH4}}{wt\ catalyst}$$

The coking rates (*r_coking*, mg coke/(mg•h))are calculated as follows:

$$r\_coking = \frac{\Delta wt}{\Delta t * wt\ catalyst}$$

where Δwt is the weight change of the catalyst measured after the first hour of the experiment (which typically lasted 3 h) and Δt is the time span of this weight change.

## A.4. Flow Controller Calibration

$N_2$ (Tylan General FC2979MEP5): y = 20.051*x-1.1995 R=0.9938

$CO_2$ (Aera FC 7700C): y =15.361*x+1.22 R=0.9922

$CH_4$ (Unit UFC 1200A): y = 46.775*x+2.8237 R=0.9915

y: Flowrate in mL/min; x: Voltage in Volts

## A.5. Gas Chromatographic Analysis

The gas samples taken after the reactor were analyzed by an Agilent 6890N GC/MS. Three 1/8" molecular sieve columns Wasson K1 (6 ft), K2 (7 ft), and K2S (2 ft) in series were used to separate hydrogen from the rest of the gaseous mixture, with the $H_2$ analyzed by a thermal conductivity detector. A 1 mL sample was injected using $N_2$ as the carrier gas. A pressure regulator set at 30 psig controlled the flow of carrier gas in the columns. Another 1 mL sample was injected into a 0.53 mm, 50 m capillary column (Wasson KC080) to separate $N_2$, CO, $CO_2$, $CH_4$ and water, also analyzed by a thermal conductivity detector. Helium was the carrier gas, controlled by the back inlet electronic flow controller. A third sample was injected (as needed) to a 100 m, 0.25 mm Wasson KC066 column which separated all components and fed the MSD, which was used for qualitative confirmation of the components. Helium was the carrier gas, controlled by the front inlet electronic flow controller. The oven program and TCD details are provided below. GC calibration factors and retention times are presented in Table A1. A screenshot of a typical separation is shown as Figure A.2.

Front Inlet – Split; 120°C; P: 4.5 psi; column flow 0.5 mL/min; total flow: 7.8 mL/min; split ratio = 10:1; split flow = 4.8 mL/min

Back Inlet – Split; 120°C; P: 7.4 psi; column flow 5.4 mL/min; total flow: 79 mL/min; split ratio = 13.1:1; split flow=70.4 mL/min

Front Detector – TCD; 200°C; 16.5 mL/min ref. flow; 11 mL/min makeup flow; Gas = He

Back Detector – TCD; 200°C; 20 mL/min ref. flow; 3 mL/min makeup flow; Gas = $N_2$; Negative polarity

GC Oven Program – Initial Temp = 30°C; Initial time = 7 min; Rate1 = 10°C/min to 100°C; 5 min hold; Rate2 = 10°C/min to 130°C; 16 min hold

Post Temp= 30°C; Post Time = 15 min; Total run time = 38 min

Packed Auxiliary Oven Temperature Program – Initial Temp = 50°C; Initial time = 5 min; Rate1 = 10°C/min to 120°C, hold 11 min; Rate2 = 10°C/min to 50°C

Chase heater – 100°C

Injector (GSVs) oven – 200°C

Table A.1. GC Calibration Factors and Retention Times

| Component | GC Factor mol(μmol)/area(MM)[1] | Retention time (min) |
|---|---|---|
| CO | 0.46 | 3.6 |
| $CO_2$ | 0.42 | 8.9 |
| $N_2$ | 0.50 | 3.5 |
| $CH_4$ | 0.60 | 4.3 |
| $H_2O$ | 0.55 | 21.3 |
| $H_2$ | 0.095 | 2.8[2] |

[1]These are the final GC factors. The system was re-calibrated twice in four years.
[2]This is the retention time for the packed columns.

The component identities and calibration factors were determined by injection of a series of standards, both mixture and pure component.

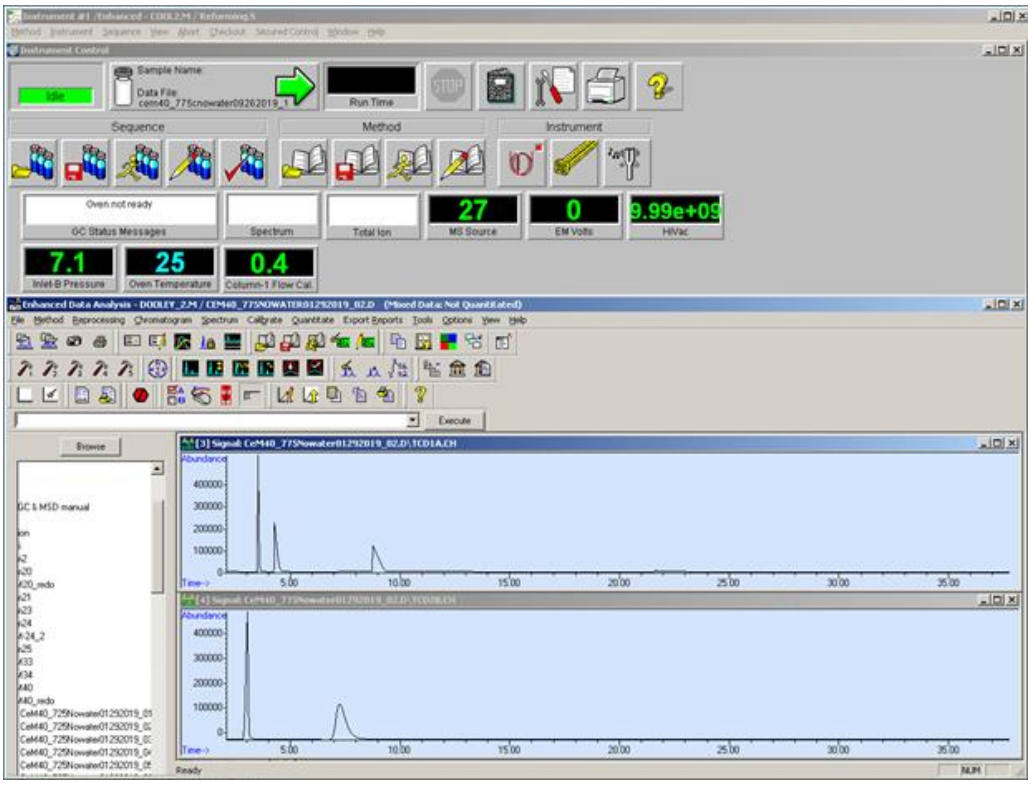

Figure A.2. Chromatograms of a typical separation. Top is for the capillary column to the front detector; bottom is for the packed columns to the back detector.

## A.6. Estimation of Weisz Moduli

The Weisz modulus ($W_M$) can be expressed as follows:

$$W_M = \frac{r_{vobs}\, L^2}{C_A D_e}$$

Where $r_{vobs}$ is the observed reaction rate per unit particle volume, $L$ the characteristic catalyst dimension, $C_A$ the concentration at the limiting reactant in the fluid and $D_{eA}$ its effective diffusivity in the catalyst particle. For $W_M << 1$, there should be no pore diffusional limitations.

$W_M$ was calculated based on the results for the oxidized Ni0.2/Co0.2/Ce/Zr catalyst. As this was one of the more active catalysts (Ch. 2, Table 2.1), and as all of the catalysts were made from similar batches of the rare-earth oxides with similar particle sizes, the $W_M$ results shown

here are characteristic of all active catalysts. Particle sieving established the weight-average spherical diameter ($d_p$) as roughly 200 μm. For spheres, $L = d_p/6$. The partial pressures of $CH_4$ and $CO_2$ were both 26 kPa (51 kPa $N_2$) and the temperature of the DSC/TGA experiment 750°C. From these, the diffusivities of $CH_4$ and $CO_2$ could be computed by the Chapman-Enskog equation.

$$D_{CH4} = 1.7 \times 10^{-4}\ m^2/s$$

$$D_{CO2} = 1.3 \times 10^{-4}\ m^2/s$$

For the catalyst, the skeletal densities of $CeO_2$ etc. were weighted to give 6.56 $g/cm^3$. The surface area and pore volume prior to use were 22 $m^2/g$ and 0.14 $cm^3/g$, respectively. From these the porosity (ε) was computed (0.48), and the average cylindrical pore size ($1.3 \times 10^{-6}$ cm), and to determine effective pore diffusivities the standard equation was used:

$$D_{ej} = D_j\ \varepsilon/\tau$$

where Dej is the effective pore diffusivity of component j, $D_j$ is the combined (bulk – Knudsen) diffusivity of component j, and τ is the tortuosity, which is taken as the random pore result (τ = 3). The effective diffusivities are:

$$D_{CH4} = 1.5 \times 10^{-6}\ m^2/s$$

$$D_{CO2} = 9.2 \times 10^{-7}\ m^2/s$$

The final Weisz moduli are:

$$W_{M,CH4} = 4.6 \times 10^{-2}$$

$$W_{M,\,CO2} = 7.6 \times 10^{-2}$$

which proves that the rates are not pore diffusion-limited. Catalysts that aren't pore-diffusion limited can't be diffusion-limited in the boundary layer, but this was checked in the standard way (assuming the Sherwood number at low Reynolds number = 2) and it was found that the partial

pressure gradient in the boundary layer could be no more than 0.17% of the bulk concentration of either reactant.

# APPENDIX B. DATA PROCESSING DETAILS OF XPS, XANES AND XAFS

## B.1. XPS

XPS data processing was performed with CasaXPS, version 2.3.1 PR1.0. The Shirley background subtraction[215]and Gaussian/Lorentzian peak shapes were applied during the peak fitting. The binding energy of all spectra were calibrated using the C1s (284.8 eV) photoelectron lines as a reference. During the deconvolution, the peak maximum, full width at half maximum (FWHM), peak position and peak area ratio between two peaks in a doublet were constrained. For instance, the peak area ratio for Ni $2p_{1/2}$:$2p_{3/2}$ would be constrained to 1:2. Surface atomic concentrations was estimated from peak area ratios. Relative sensitivity factors (RSF) were provided by the software.

## B.2. XANES AND XAFS

### B.2.1. XANES Fitting

The XANES data processing was performed with Athena 0.8.061.[113] The spectra were merged after deglitching to get a better white line and S/N ratio. The normalization step is controlled by the value of $E_0$, and the pre-edge and normalization range. The $E_0$ was determined as the maximum of the first derivative. The pre-edge range was set to -150 to -30 eV relative to $E_0$. The normalization range is >150 eV beyond $E_0$. For the background subtraction, the Rbkg (distance in Å for $\chi$(R) above which the signal is ignored) is set to 1. This parameter is used for the backgroud subtraction based on a built-in AUTOBK algorithm.

### B.2.2. XAFS Fitting

The XAFS fitting was performed with Artemis 0.9.26. ATOMS was used to generate the input file for the Feff calculation. The output Feff file contains the crystal structure information

such as the normal coordination numbers, effective path lengths, and description of scattering paths.

The XAFS spectrum can be understood in terms of the XAFS equation, which can be written as a sum of the contributions from all the scattering paths. For each scattering path, the equation can be written as following:[216, 217]

$$\chi_i(k) \equiv \frac{(N_i S_0^2) F_{eff_i}(k)}{kR_i^2} \sin\left[2kR_i + \varphi_i(k)\right] e^{-2\sigma_i^2 k^2} e^{\frac{-2R_i}{\lambda(k)}}$$

Five parameters can be fit from this equation, $N_i$ (coordination number), $S_0^2$ (amplitude reduction factor), $\sigma^2$ (Debye-Waller factor), $\Delta E_0$ (the deviation in $E_0$ caused by structural deviations from an ideal crystal structure) and $\Delta R$ (the deviation in interatomic distance from the ideal crystal structure).

For Ni K-edge XAFS, the Ni and NiO standards were fit first to get information on $S_0^2$ with known coordination numbers and distances. The fitting range in R space was 1-5 Å and all significant scattering paths were included.

For the Debye-Waller factors for multiple scattering paths, the following constraints were used based on the recommendations of the program.

Double scattering: S1S2 = 1.5*ss

3-leg (triangle): S1S2 = 0.5*ss + ssa

Non-forward linear: S1S1 = ss2

Forward through absorber: S1+S1 = 2*ss

Rattle: S1 + S1 = 4*ss

where ss is the Debye-Waller factor of the primary scatterer, and ssa is the factor to the next nearest atom. $S_0^2$ varies for different scattering paths as well. For example, for a two-leg Ni

atoms scattering path, the $S_0^2$ is estimated as the product of two $S_0^2$ factors for Ni single scattering.

Table B.1 shows the fitting results for the NiO powder standard. The XAFS plot showing the fit is given in Chapter 3.

Table B.1. Results of fitting analysis of Ni K-edge XAFS for NiO powder standard

| Name | N | $\sigma^2$ | R |
|---|---|---|---|
| 1st Ni-O shell | 6 | 0.0041±0.0007 | 2.07±0.01 |
| 1st Ni-Ni shell | 12 | 0.0056±0.0003 | 2.94±0.002 |
| 2nd Ni-O shell | 8 | 0.011 | 3.50 |
| 2nd Ni-Ni shell | 6 | 0.0067 | 4.24 |
| 3rd Ni-O shell | 24 | 0.011 | 4.63 |
| 3rd Ni-Ni shell | 24 | 0.0067 | 5.12 |

R-factor:0.02

The confidence limits on $\sigma^2$ and R are given by the program. Statistical parameters such as the R-factor, $\chi^2$ (chi squared), and $\chi_\upsilon^2$ (reduced chi squared) were also provided, and are used to examine the goodness of fit. The R-factor is defined as follows:

$$\mathrm{R-factor} = \frac{\sum_i (\mathrm{data}_i - \mathrm{fit}_i)^2}{\sum_i \mathrm{data}_i^{\,2}}$$

The chi squared is the sum of the squares of the differences between the predicted fit and the data, divided by the uncertainties ($\varepsilon$) at each data point ($i$). It is:

$$\chi^2 = \frac{N_{\mathrm{idp}}}{N_{\mathrm{pts}}} \sum_i \left( \frac{\mathrm{data}_i - \mathrm{fit}_i}{\varepsilon_i} \right)^2$$

where the sum is over each data point in the real and imaginary parts of the Fourier transform, $N_{idp}$ is the number of independent data points in the model fit, which is described by the following equation, and $N_{pts}$ is the number of data points.

$$N_{\mathrm{idp}} = \frac{2}{\pi} \Delta k \Delta R + 1$$

The $\Delta k$ is the Fourier-transformed data range, and $\Delta R$ is the region of R used in EXAFS data analysis. The reduced chi squared was used to comparing the fits for regression models where the number of fitted parameters differed. It is the chi squared divided by the number of degrees of freedom for the fit.[218]

# APPENDIX C. SUPPLEMENTARY INFORMATION FOR CHAPTER 2

Table C.1. Comparison of reforming rates at >1 h calculated from DSC/TGA results. Samples pretreated with either $N_2$ only or 25% $H_2/N_2$ at 750°C for at least 6 h, then fed 1:1 $CH_4$: $CO_2$ (0.25 atm each).

| Designation / Molar Ratios | Heat flow (mW/mg) | |
|---|---|---|
| | $N_2$ only | 25% $H_2/N_2$ |
| Co/Ce9 | 1.3 | 2.4 |
| Co/Ce5 | 6.8 | 6.7 |
| Ni0.12/Ce/Zr | 7.1 | 9.1 |
| Ni0.2/Co0.2/Ce/Zr | 8.9 | 11.9 |
| Pd0.27/Ce3/Zr | 3.9 | 6.2 |
| Ni0.5/Ce3/Zr | 6.3 | 9.2 |
| Mn0.82/Ce3/Zr | 0.99 | 0.76 |

Table C.2. BET surface areas of spent Pd and Ni catalysts. The initial mixed rare earth oxides all had surface areas >130 $m^2/g$, the TM-doped, calcined materials all were >60$m^2/g$.

| Designation / Molar Ratios | Surface Area, $m^2/g$ |
|---|---|
| Ni2/Ca/Mg2/Al[1] | 18 |
| Pd/Ce9 | 35 |
| Pd0.27/Ce3/Zr | 21 |
| Ni0.3/Co0.3/Ce3/La | 9.8 |
| Ni0.15/Ce2/Zr | 6.6 |
| Ni0.3/Ce2/Zr | 22 |
| Ni0.5/Ce3/Zr | 47 |
| Ni0.2/Co0.2/Ce/Zr | 13 |
| Co0.3/Ce3/Zr | 3.5 |
| Co/Ce9 | 5.6 |

[1]40 wt% $Al_2O_3$. The other numbers are molar ratios.

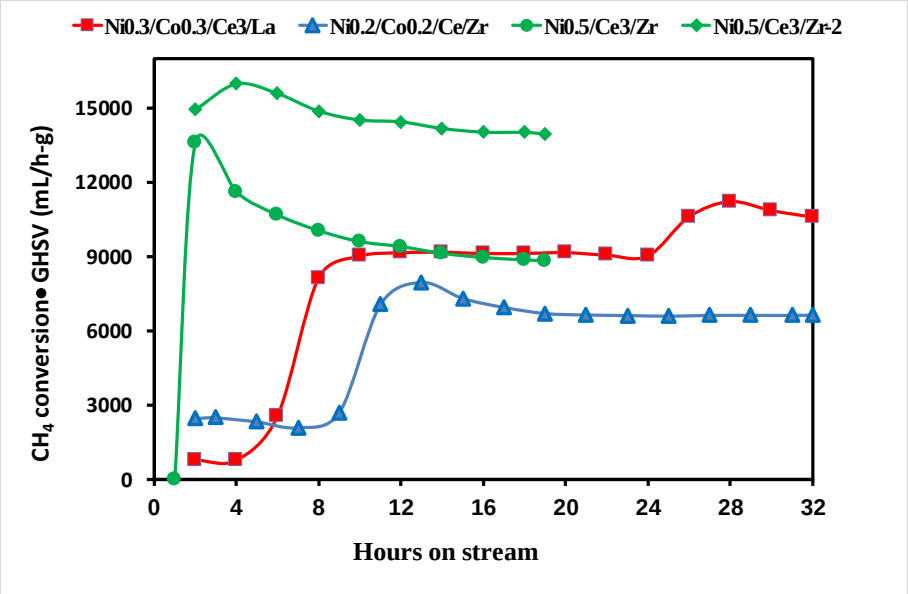


Figure C.1. Activation of freshly reduced (5% $H_2$, 750°C, 6 h) Ni-based catalysts with time on stream. Data for Ni0.5/Ce3/Zr-2 taken after an intermediate oxidation step.

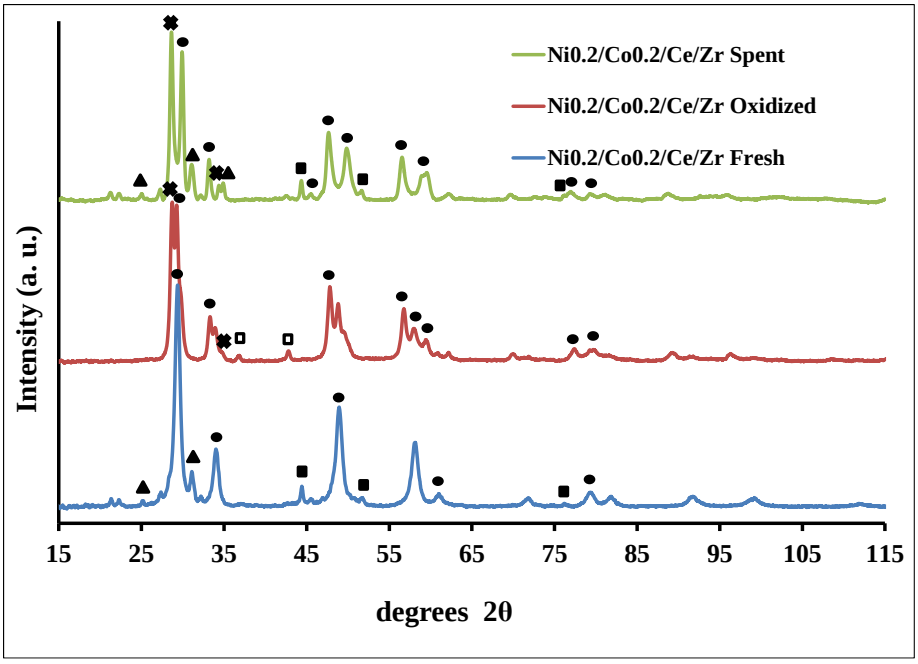


Figure C.2. XRDs of freshly reduced, oxidized (800°C, air), and spent Ni0.2/Co0.2/Ce/Zr. Peaks marked with filled triangles denote monoclinic $ZrO_2$, filled squares fcc Ni/Co metal, open squares NiO, circles distorted fluorite $CeO_2$-$ZrO_2$, crosses Ce-Zr oxide and/or $ZrO_2$.

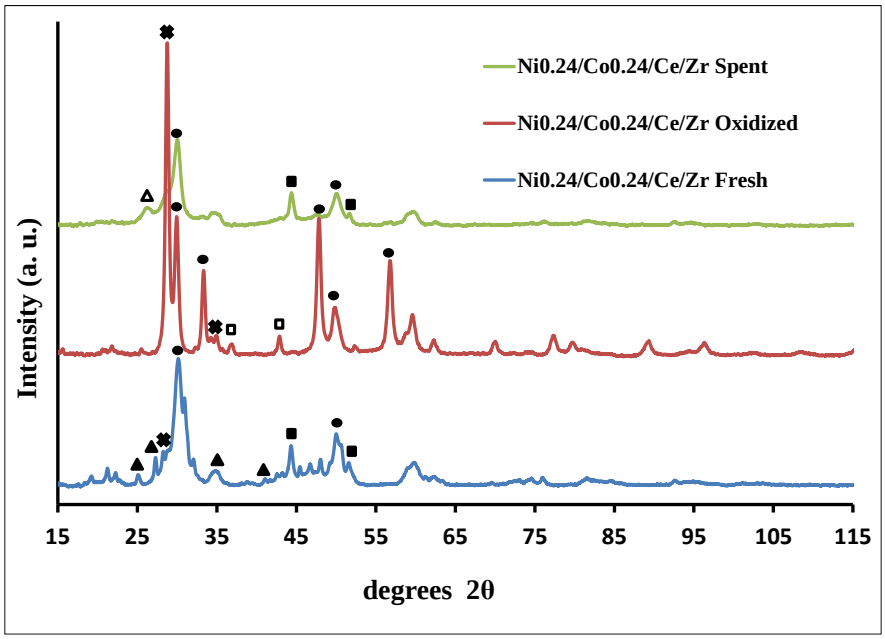


Figure C.3. XRDs of freshly reduced, oxidized and spent Ni0.24/Co0.24/Ce/Zr. Peaks marked with filled triangles denote monoclinic $ZrO_2$, open triangles carbon, filled squares fcc Ni/Co metal, open squares NiO, circles distorted fluorite $CeO_2$-$ZrO_2$, crosses both Ce-Zr oxide and/or $ZrO_2$.

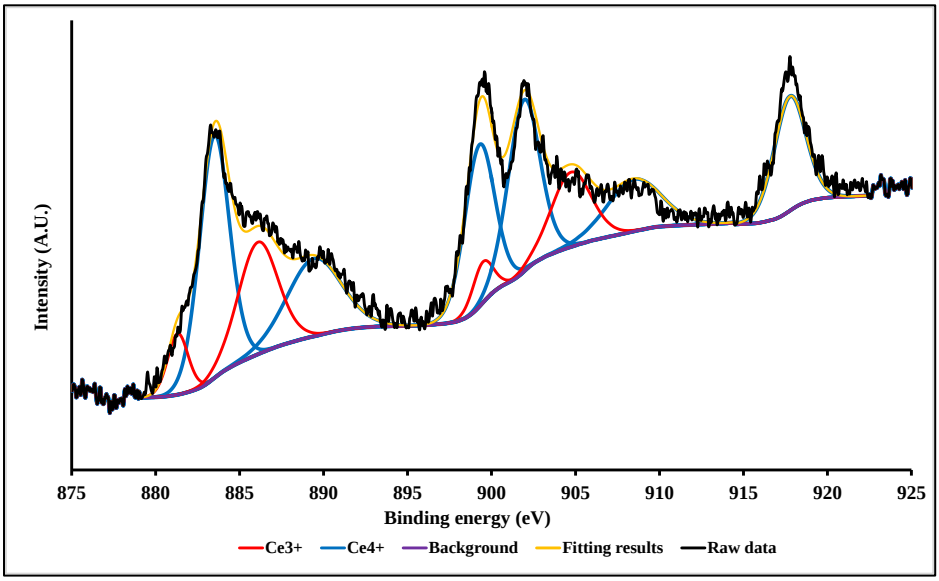


Figure C.4. Ce3d XPS of spent Ni0.15/Ce2/Zr.

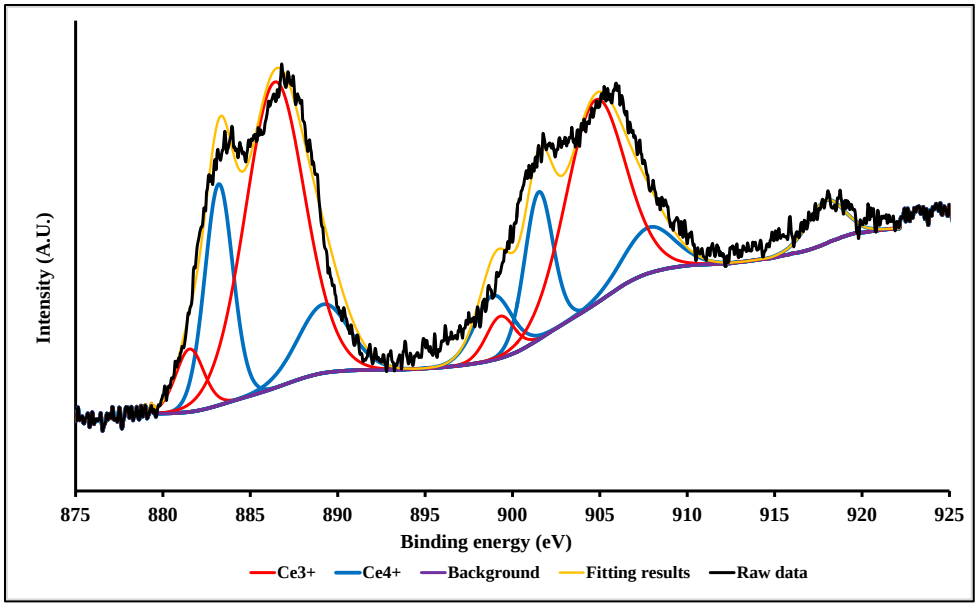

Figure C.5. Ce3d XPS of spent Ni0.24/Co0.24/Ce/Zr.

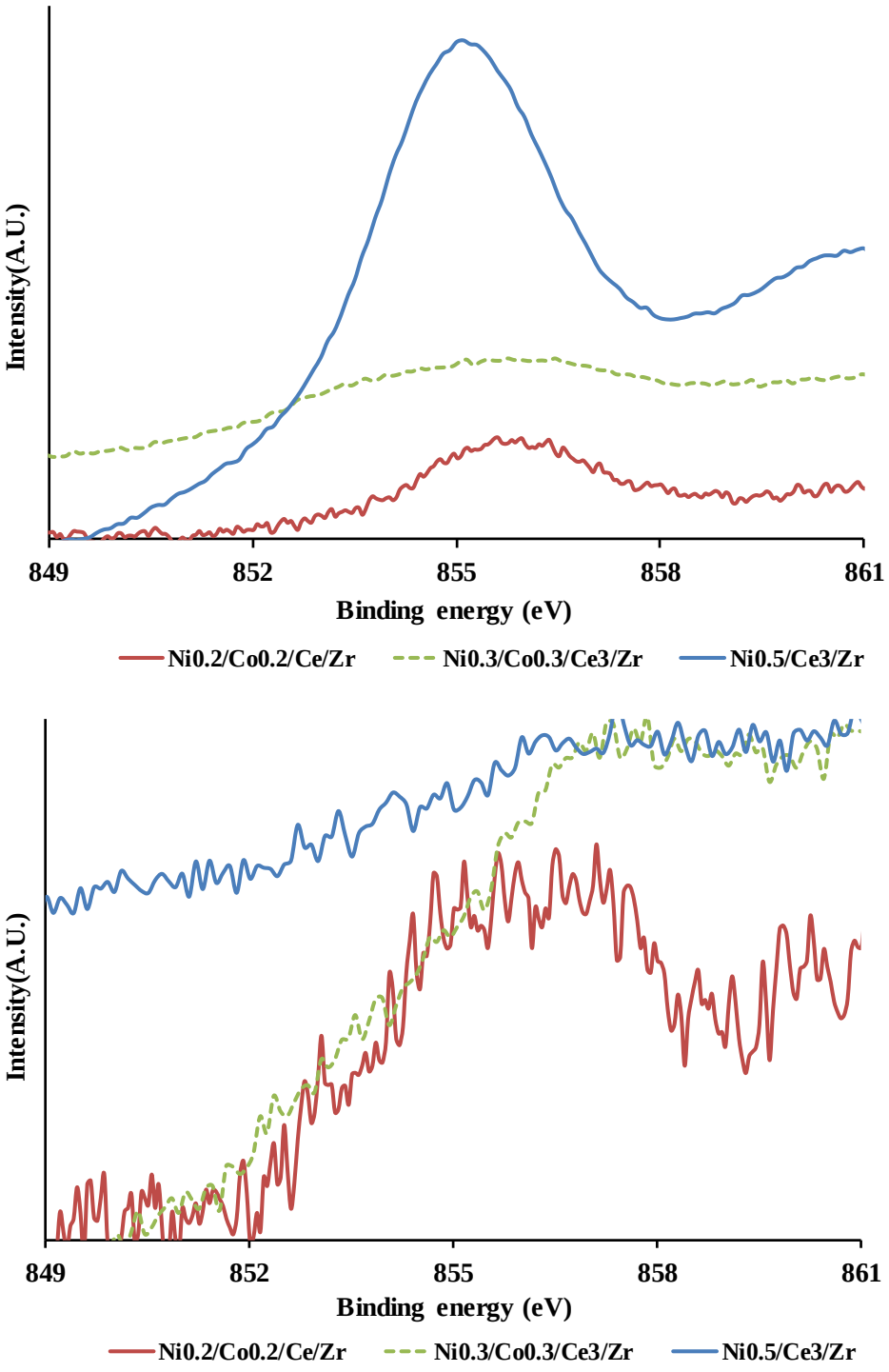


Figure C.6. Ni 2p 3/2 XPS of fresh (top) and spent (bottom) catalysts.

**La-doped Ceria DFT Results**

Table C.3. Vacancy formation energies ($E_{vac}$) to remove lattice O atoms from $M_4O_x$ to form $M_4O_{x-1}$ + ½ $O_2$ using a periodic bulk unit cell.

| Reaction | $E_{vac}$ (eV) |
|---|---|
| $Ce_4O_8 \rightarrow Ce_4O_7 + 1/2\ O_2$ | 3.77 |
| $Ce_4O_7 \rightarrow Ce_4O_6 + 1/2\ O_2$ | 2.94 |
| $LaCe_3O_8 \rightarrow LaCe_3O_7 + 1/2\ O_2$ | 1.53 |
| $La_2Ce_2O_8 \rightarrow La_2Ce_2O_7 + 1/2\ O_2$ | -0.20 |
| $La_2Ce_2O_7 \rightarrow La_2Ce_2O_6 + 1/2\ O_2$ | 2.76 |

Table C.4. Relative energies of $La_2Ce_{30}O_{64}$ bulk structures, with La dopant configurations 1-5 illustrated in Figure C.1.Energies are relative to most stable configuration 3.

| Configuration type | Relative Energy (in eV) |
|---|---|
| 1 | 0.05 |
| 2 | 0.04 |
| 3 | 0 |
| 4 | 0.02 |
| 5 | 0.01 |

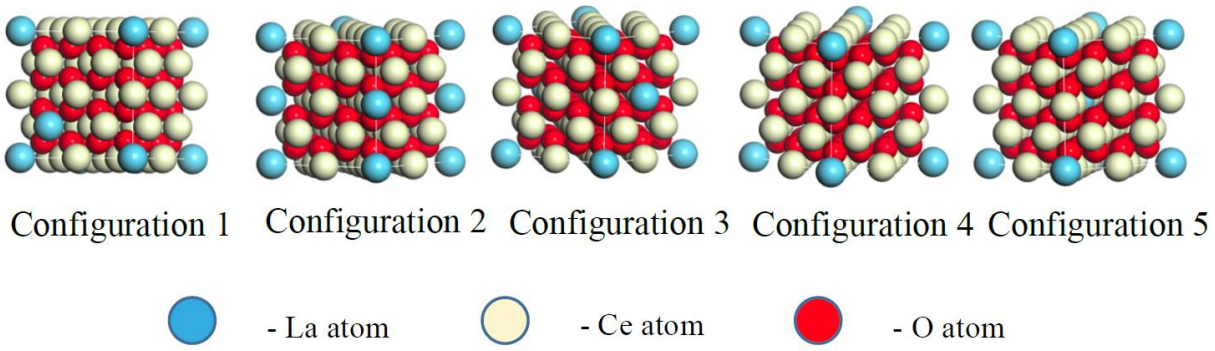


Figure C.7. Different configurations of 2 La dopants in $La_2Ce_{30}O_{64}$

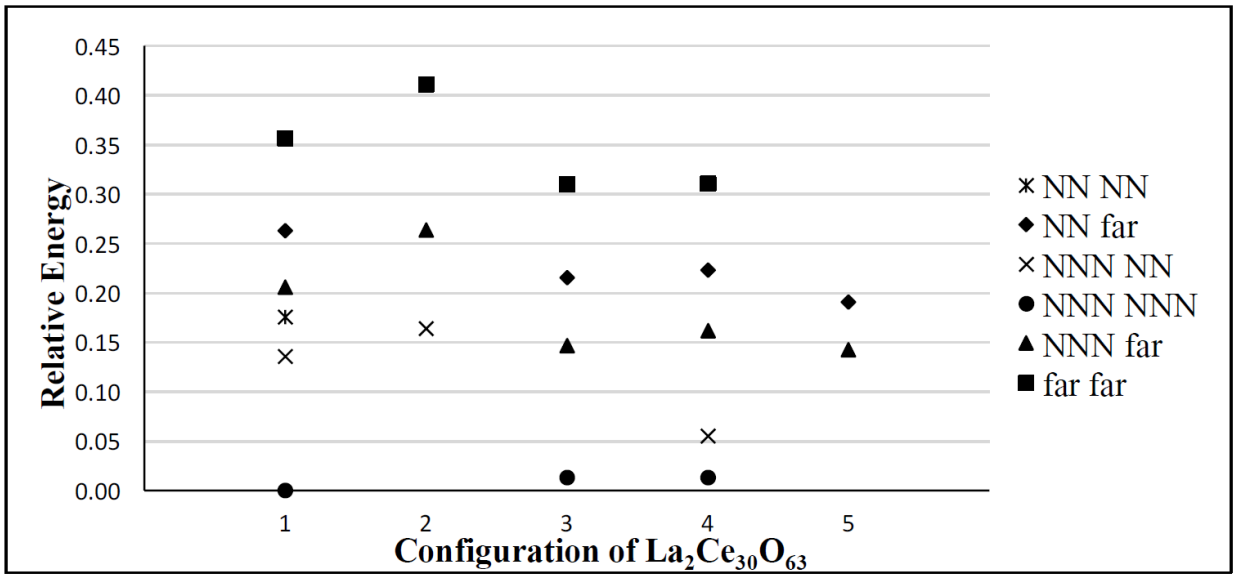


Figure C.8. Relative energies of the different $La_2Ce_{30}O_{63}$ bulk structures. La dopant configurations 1-5 are illustrated in Figure C7. Labels give O vacancy position relative to the 2 La dopants. NN and NNN indicate nearest neighbor and next nearest neighbor vacancy respectively. Energy is relative to most stable configuration (Configuration 1 with NNN-NNN vacancies).

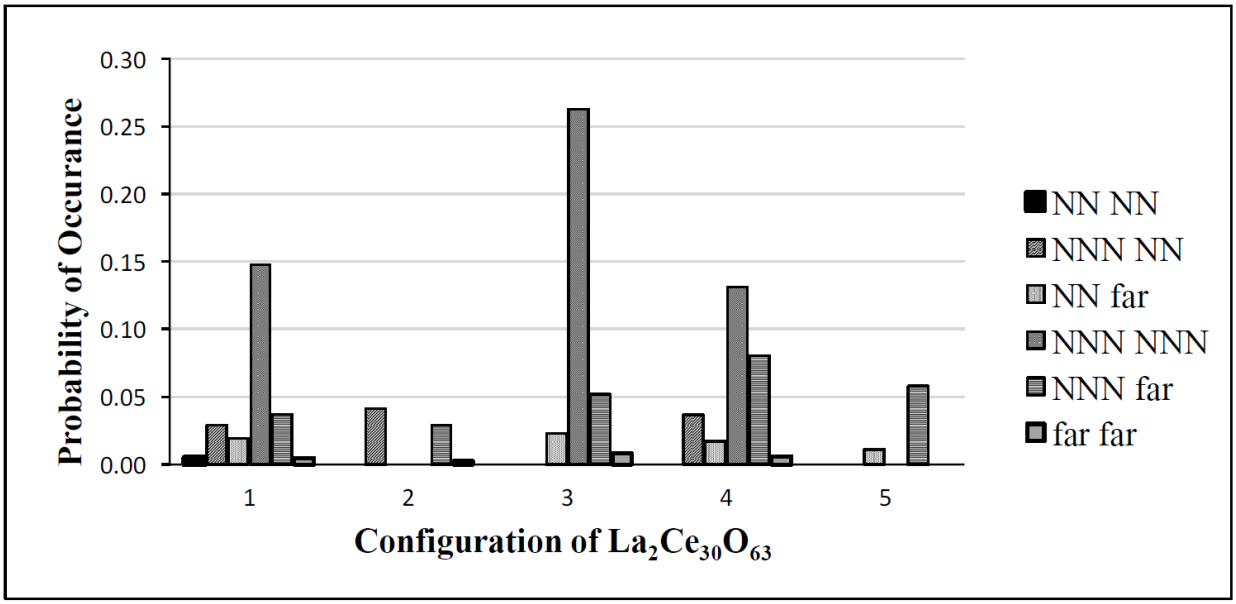


Figure C.9. Probability of occurrence of the different vacancy configurations in $La_2Ce_{30}O_{63}$ listed in Figure C.8. Probabilities calculated by Boltzmann weighting of all states enumerated in Figure C.8.

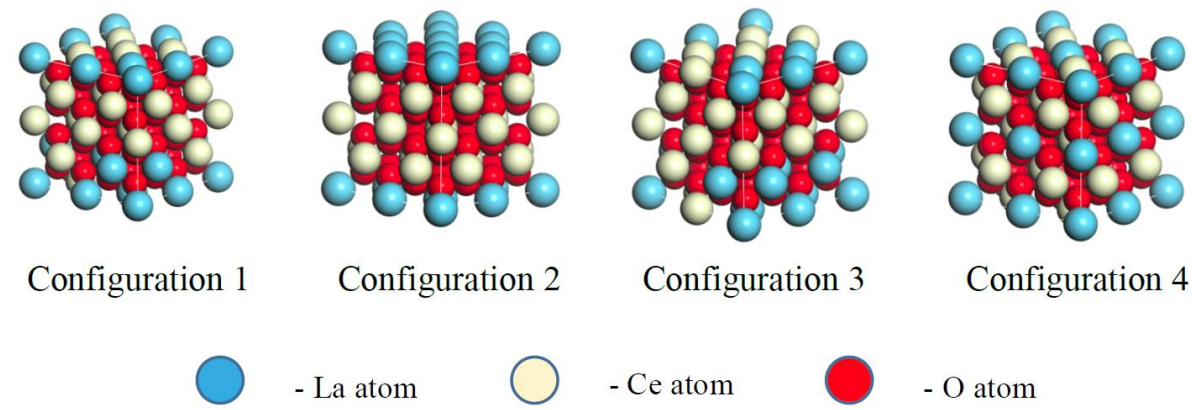


Figure C.10. Configurations considered for La dopants in a $La_8Ce_{24}O_{64}$ unit cell.

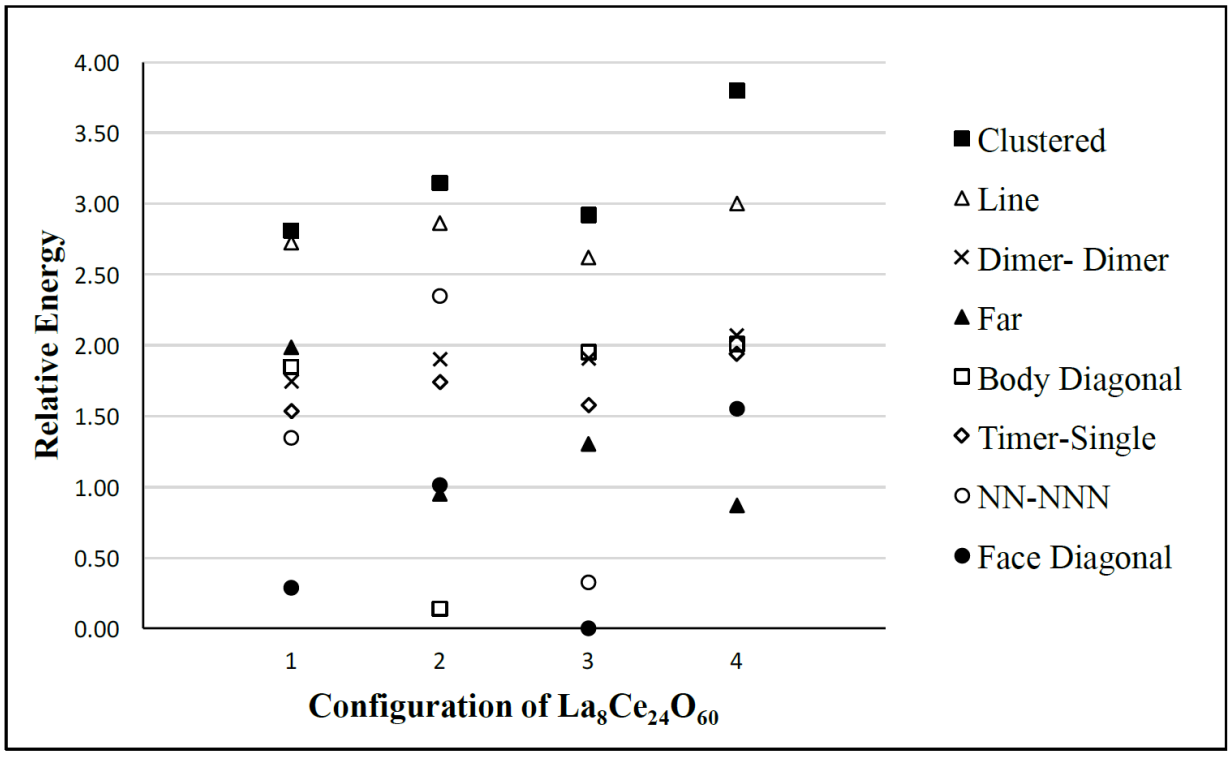


Figure C.11. Relative energies of $La_8Ce_{24}O_{60}$ structures. Configurations of La atoms are illustrated in Figure C.10. Energy is relative to the most stable configuration, which is Configuration 3 with the vacancies ordered along the face diagonal. "Clustered" refers to a configuration with the 4 O vacancies located near each other and sharing metal atoms, and is always found to be least stable. "Line" refers to the 4 vacancies located across a sequence of single metal atom sharing, and is also found to be relatively unstable.

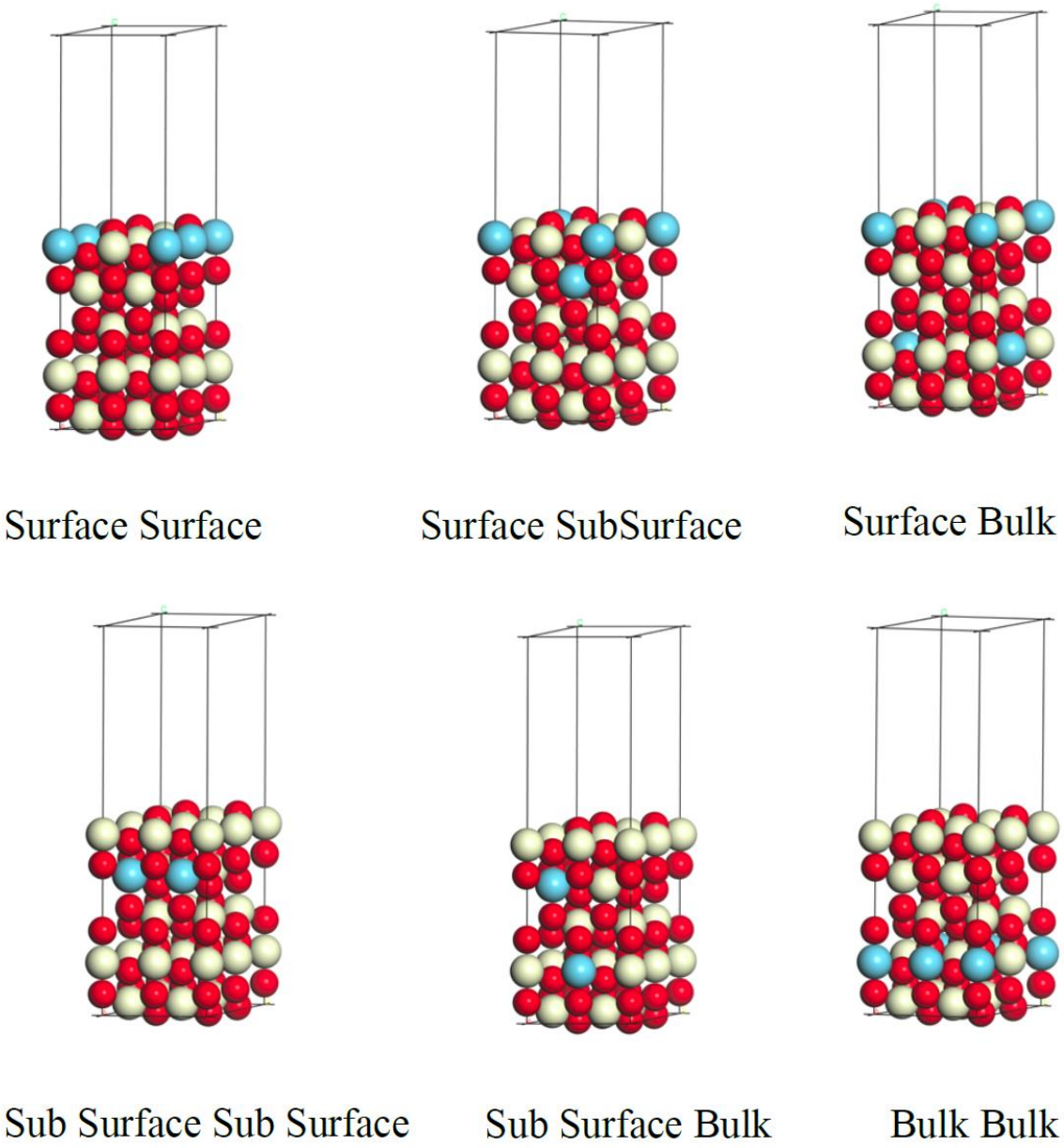


Figure C.12. Arrangements of La atoms in a $La_2Ce_{18}O_{39}$ unit cell.

Table C.5. Relative energies of $La_2Ce_{18}O_{39}$ unit cell. Headings "Surf_Surf" and "Surf_SubSurf" refer to the positioning of the La dopants in surface or subsurface layers. Energies are given in eV relative to the most stable configuration, with La dopants in the surface and subsurface and the O vacancy in the first subsurface layer.

| Vacancy Layer | Vacancy Position relative to La atoms | Relative Energy (in eV) | |
|---|---|---|---|
| | | Surf_Surf | Surf_subSurf |
| Surface | NN NN | 0.73 | |
| | NN NNN | 0.52 | 0.83 |
| | NNN NNN | | 1.02 |
| | NN Far | | 0.43 |
| Subsurface 1 | NN NN | 0.58 | 0.64 |
| | NN NNN | 0.18 | 0.38 |
| | NNN NNN | | 0.00 |
| Subsurface 2 | NN NN | | 0.80 |
| | NN NNN | 0.59 | 0.62 |
| | NNN NNN | 0.45 | 0.41 |
| Bulk | Far Far | 3.06 | 2.77 |

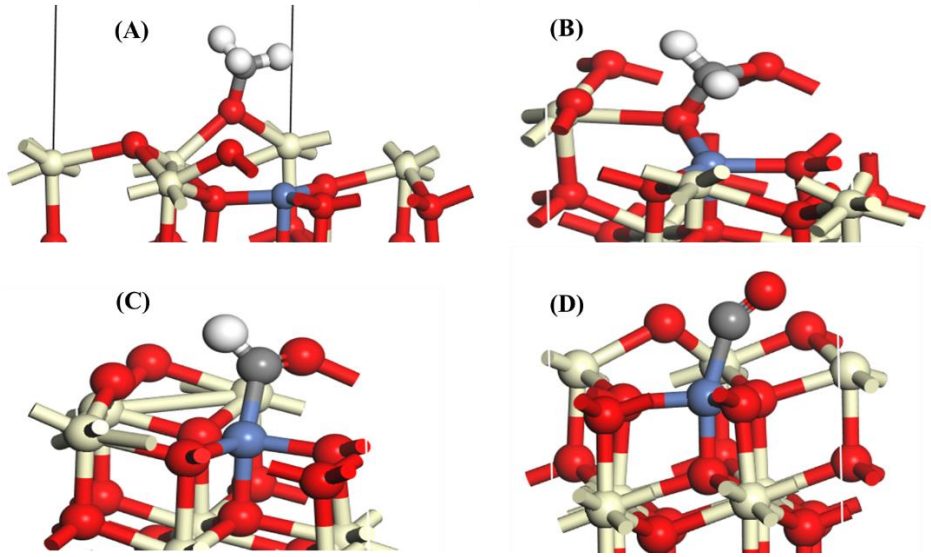


Figure C.13. Most stable structures of $CH_x$ species adsorbed to the Ni-doped $CeO_2$(111) surface (A) $CH_3$, (B) $CH_2$, (C) CH, (D) C.

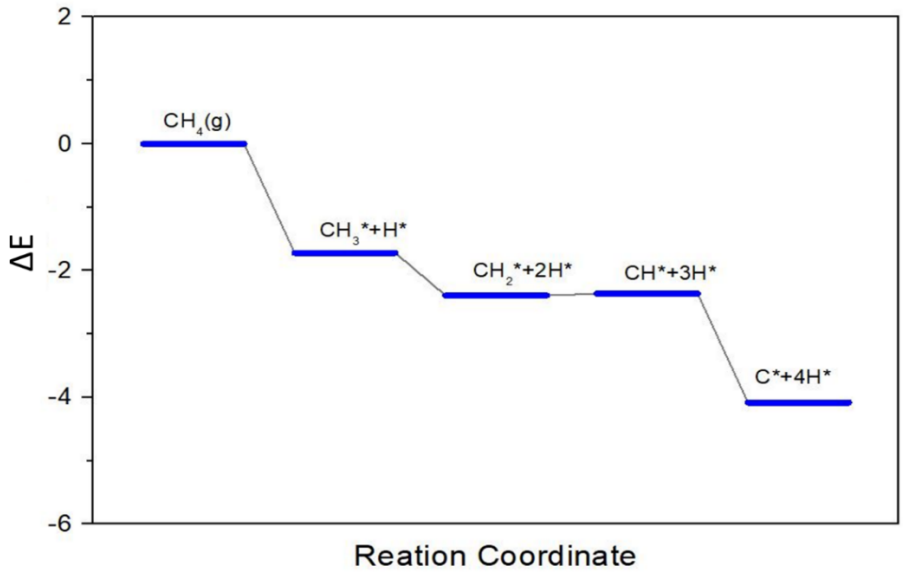


Figure C.14. Reaction energy diagram for dehydrogenation of methane on the Ni-doped $CeO_2$(111) surface.

# APPENDIX D. Supplementary Information for CHAPTER 3

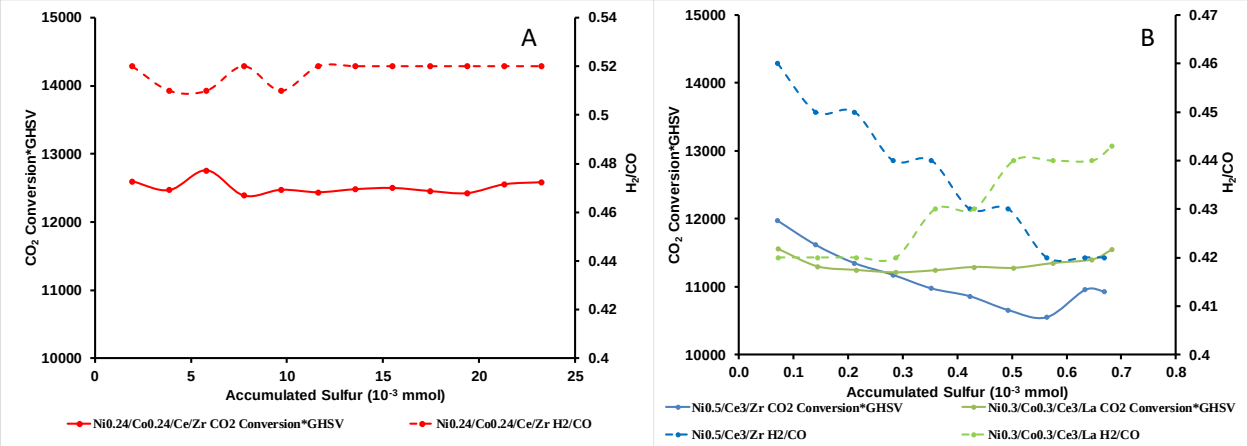


Figure D.1. Activities at 775°C of catalysts shown in Figure 3.1 after the addition of <1 ppm sulfur as DMSO. A-1 ppm sulfur in feed to Ni0.24/Co0.24/Ce/Zr; B-0.07 ppm sulfur in feed.

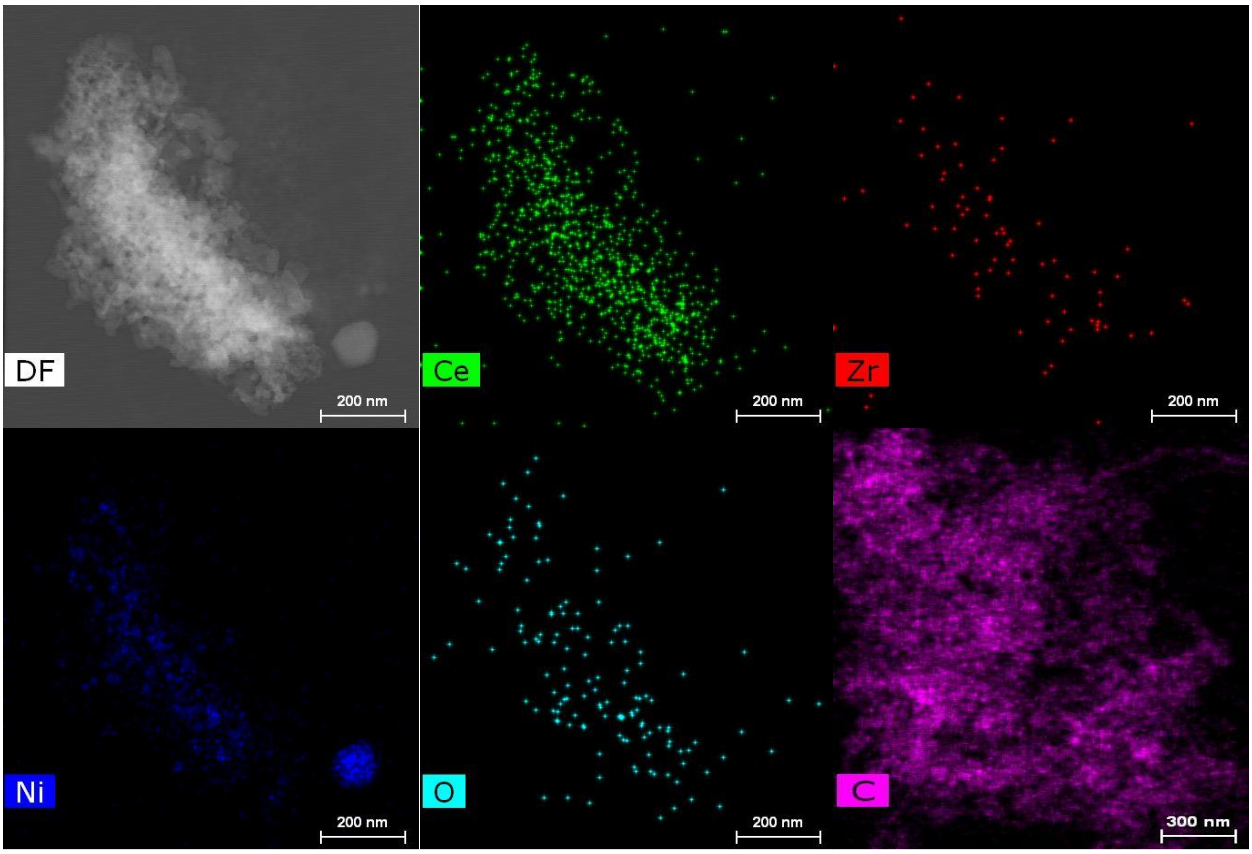

Figure D.2. EDS maps of a used catalyst particle of Ni0.5/Ce3/Zr. This is from a carbon-rich region.

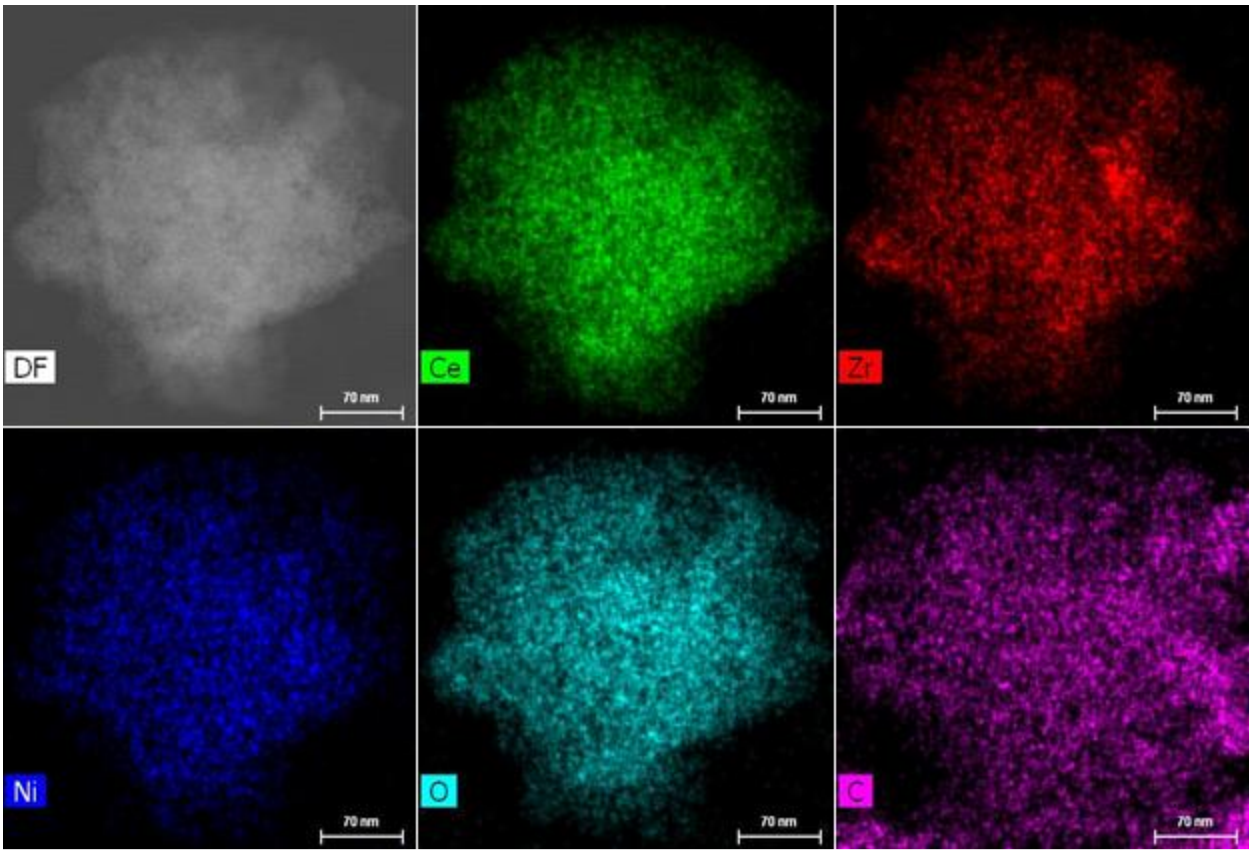

Figure D.3. EDS maps of a used catalyst particle of Ni0.5/Ce3/Zr. This is a highly uniform particle.

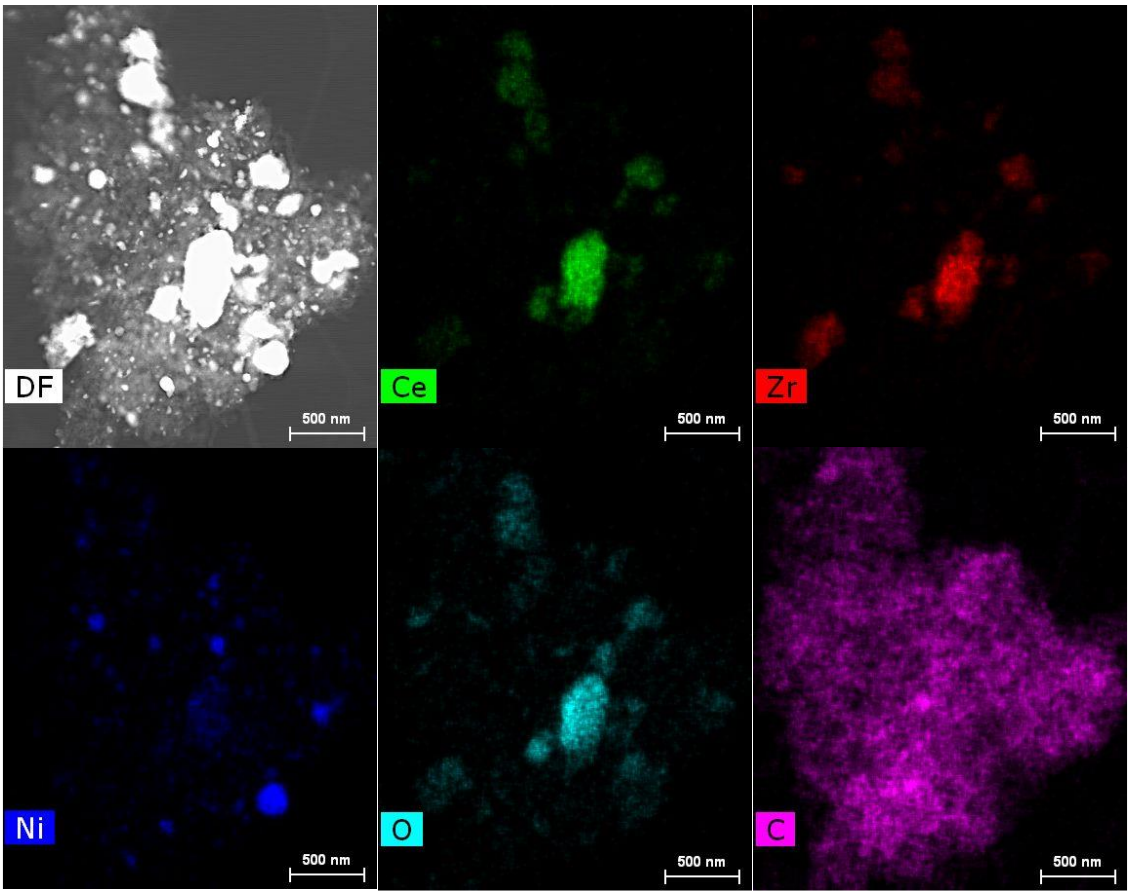

Figure D.4. EDS maps of a catalyst particle of Ni0.24/Co0.24/Ce/Zr.

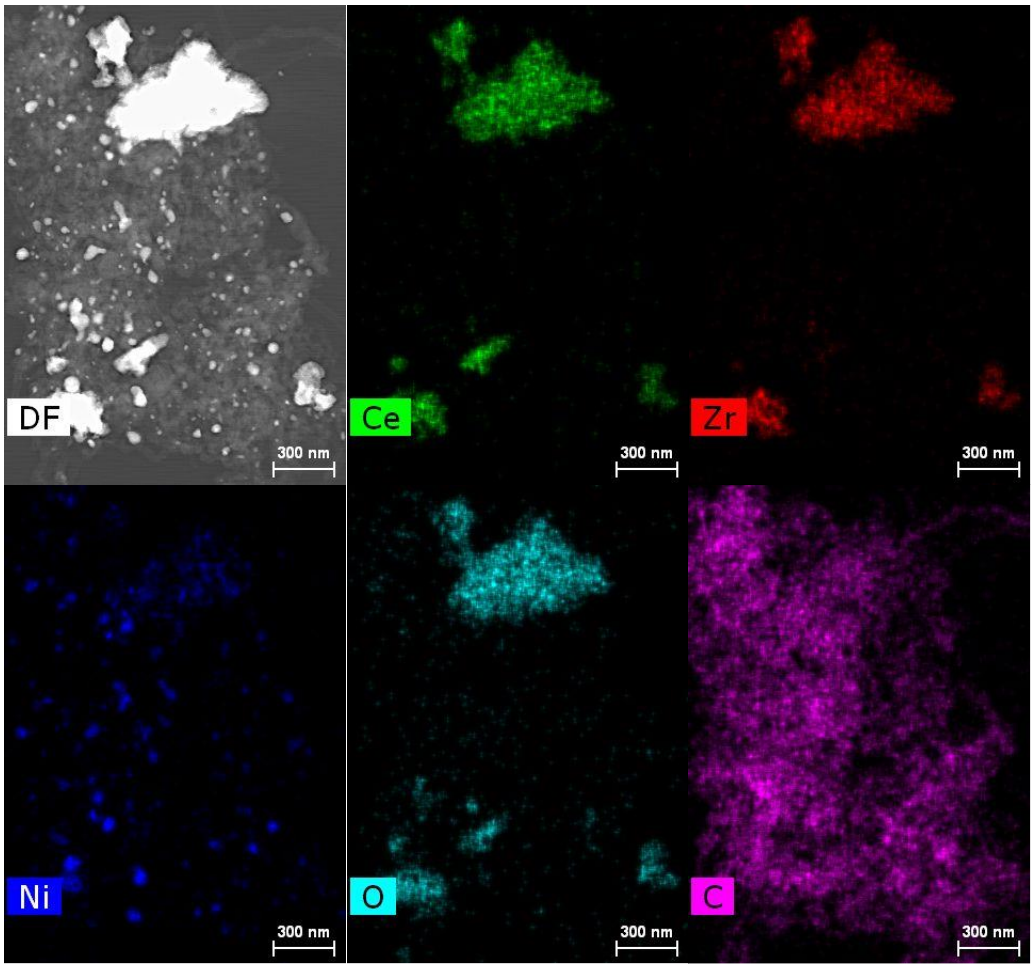

Figure D.5. EDS maps of a catalyst particle of Ni0.24/Co0.24/Ce/Zr.

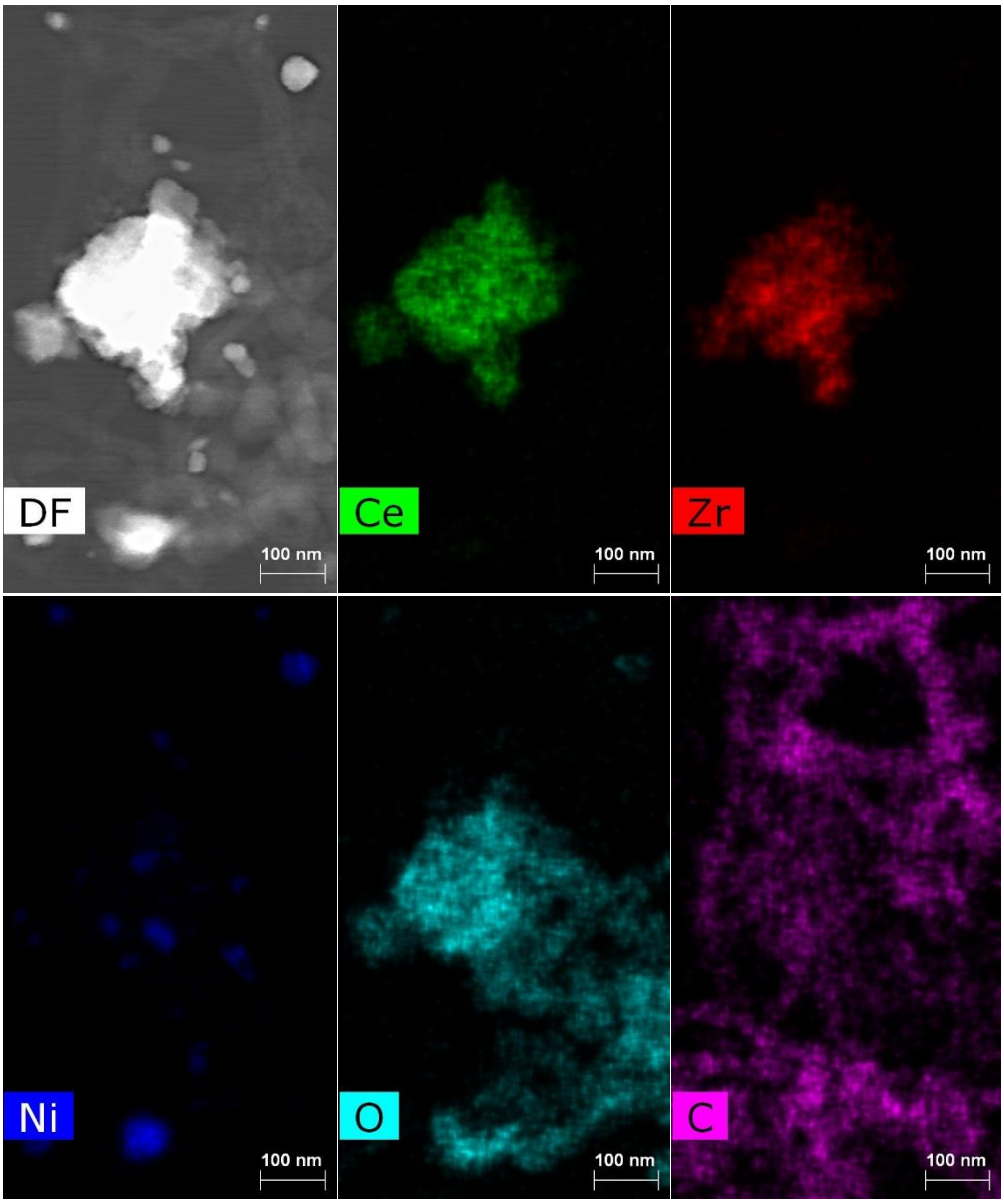

Figure D.6. EDS maps of a catalyst particle of Ni0.24/Co0.24/Ce/Zr.

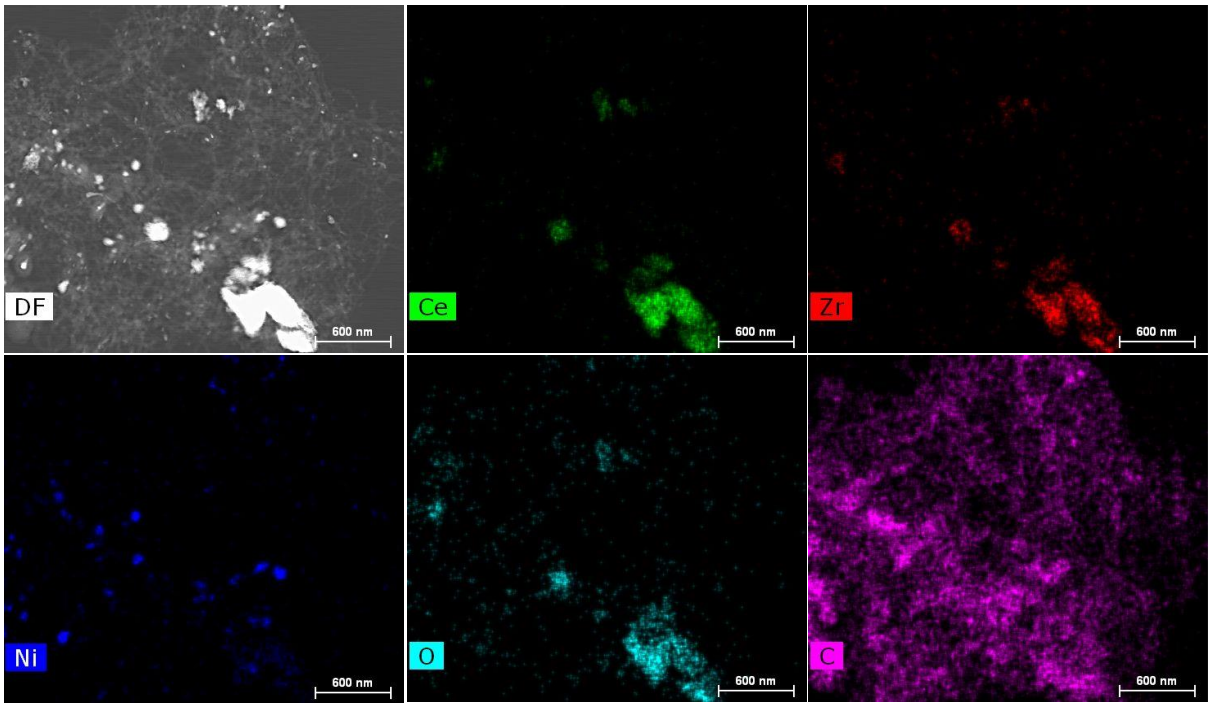

Figure D.7. EDS maps of a catalyst particle of Ni0.3/Co0.3/Ce3/Zr.

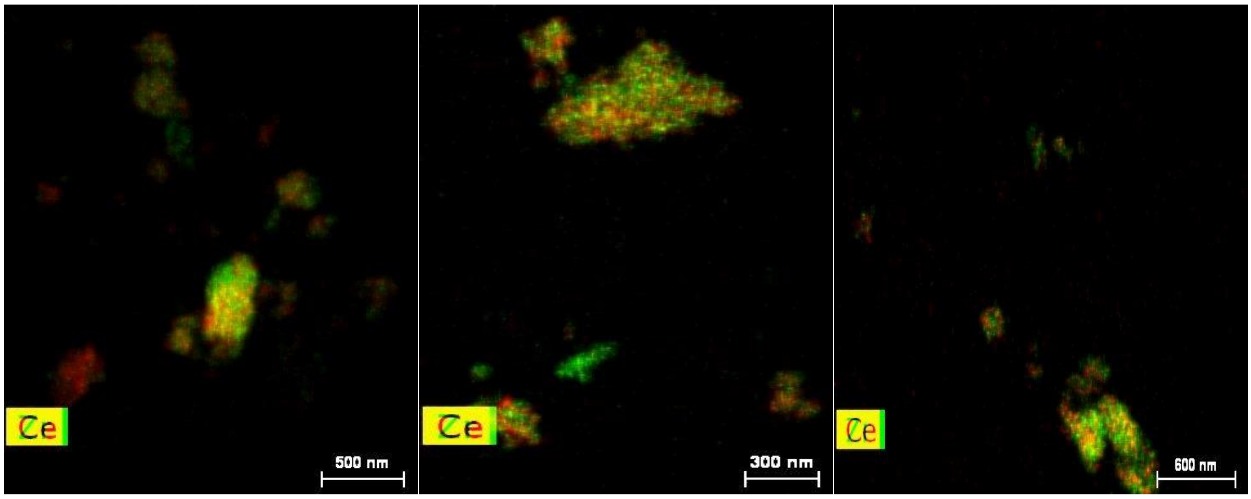

Figure D.8. Superimposed EDS maps of Ce/Zr(Ce green, Zr red) for (L to R): Ni0.24/Co0.24/Ce/Zr, Ni0.24/Co0.24/Ce/Zr, Ni0.3/Co0.3/Ce3/Zr.

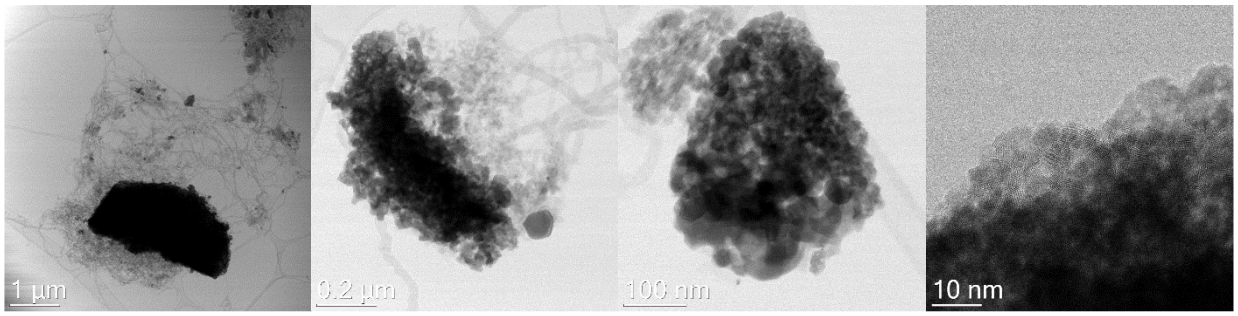

Figure D.9. TEM images of typical particles of Ni0.5/Ce3/Zr.

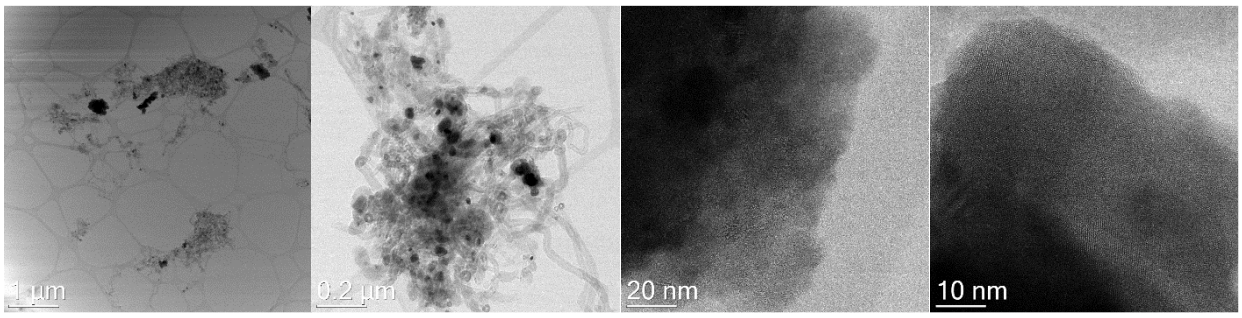

Figure D.10. TEM images of typical particles of Ni0.24/Co0.24/Ce/Zr.

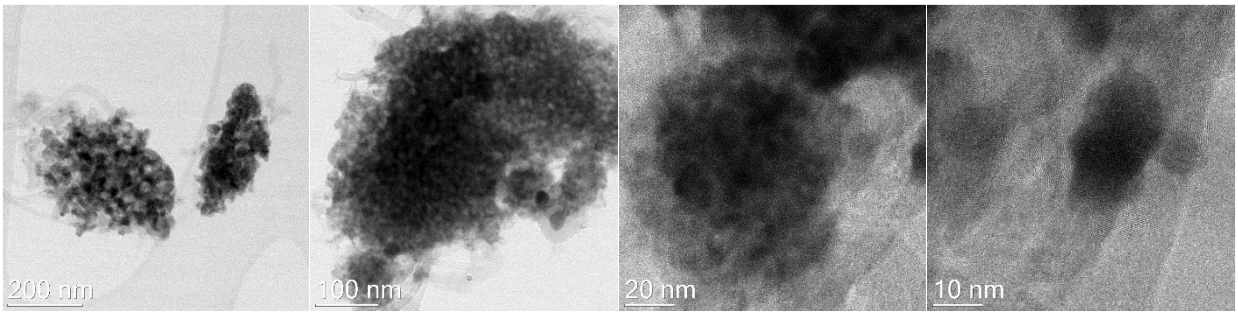

Figure D.11. TEM images of typical particles of Ni0.24/Co0.24/Ce/Zr.

Table D.1. O1s XPS fitting results

| | State | $O_\alpha$ | $O_\beta$ |
|---|---|---|---|
| Ni0.24/Co0.24/Ce/Zr | Spent | 38% | 62% |
| Ni0.15/Ce2/Zr | Spent | 52% | 48% |
| Ni0.5/Ce3/Zr | Spent | 35% | 65% |
| Ni0.3/Co0.3/Ce3/Zr | Spent | 37% | 63% |
| Ni0.5/Ce3/Zr | Fresh | 30% | 70% |
| Ni0.2/Co0.2/Ce/Zr | Fresh | 36% | 64% |

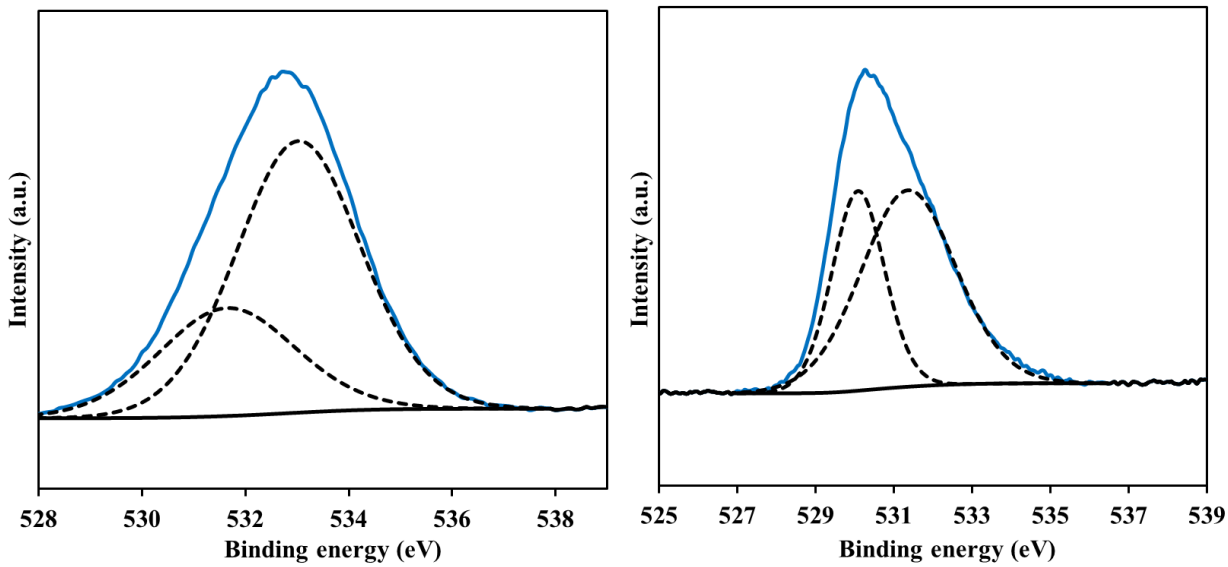


Figure D.12. O1s XPS of fresh Ni0.5/Ce3/Zr and Ni0.2/Co0.2/Ce/Zr.

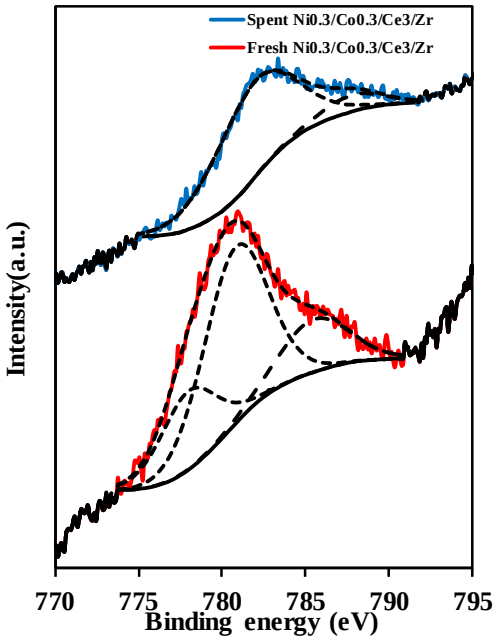


Figure D.13. Co 2p 3/2 core level spectra of fresh and spent Ni0.3/Co0.3/Ce3/Zr.

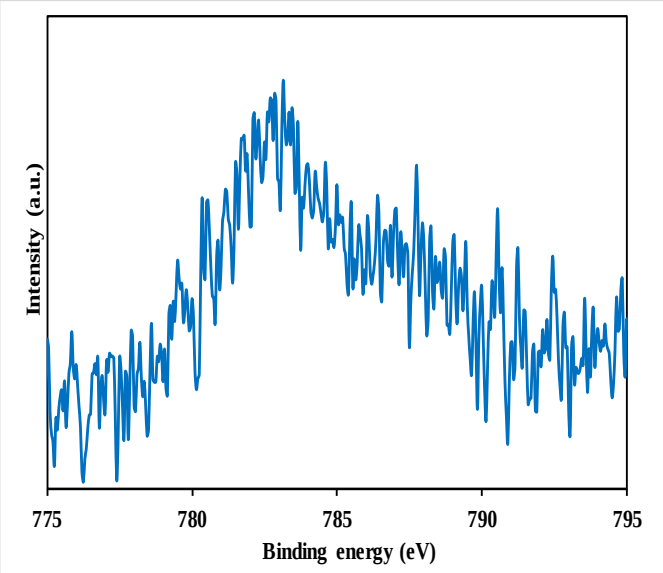

Figure D.14. Co 2p 3/2 core level spectra of spent Ni0.24/Co0.24/Ce/Zr

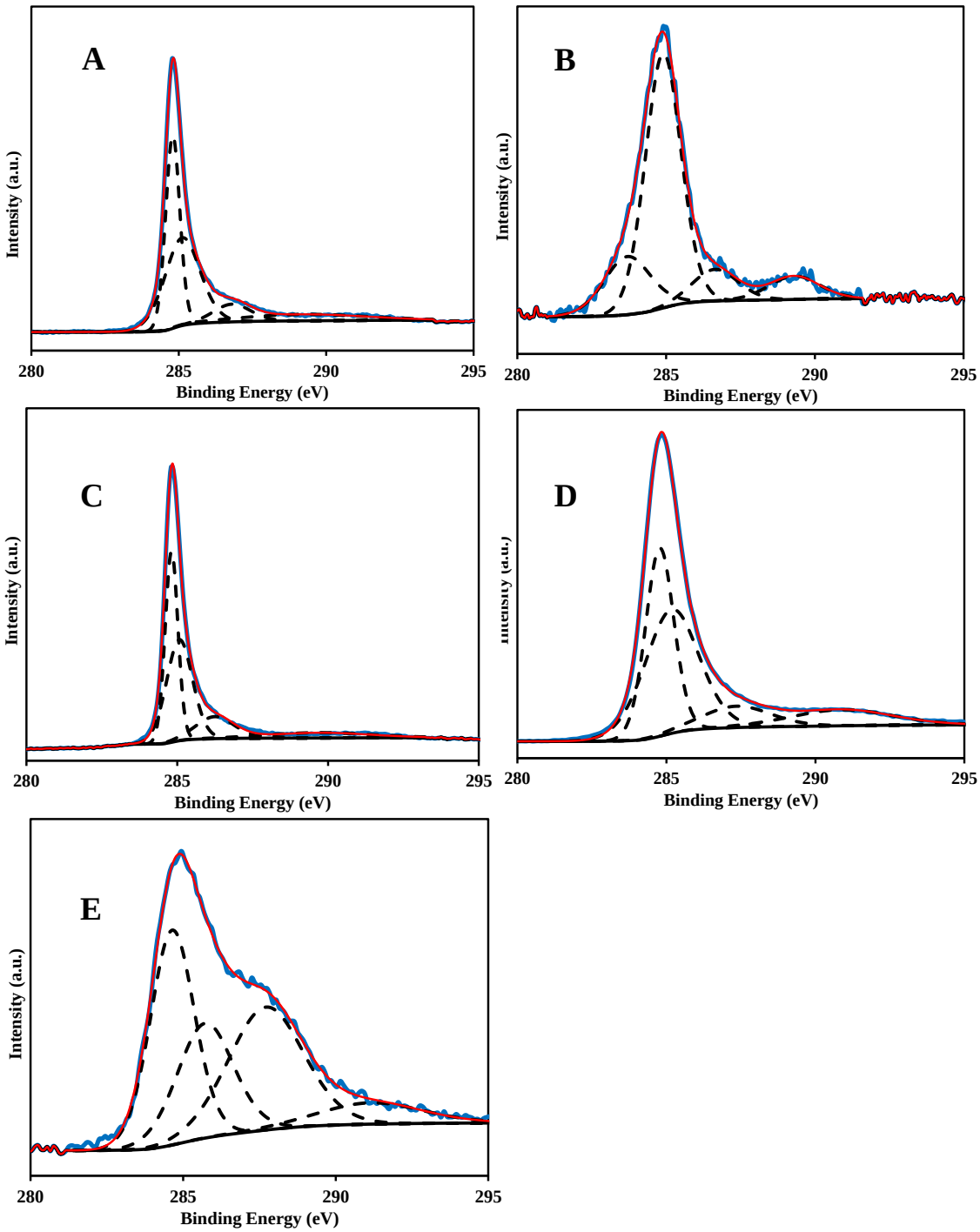


Figure D.15. Carbon 1s core level spectra of spent catalysts. A- Ni0.15/Ce2/Zr; B- Ni0.2/Co0.2/Ce/Zr; C-Ni0.24/Co0.24/Ce/Zr; D- Ni0.5/Ce3/Zr; E- Ni0.3/Co0.3/Ce3/Zr

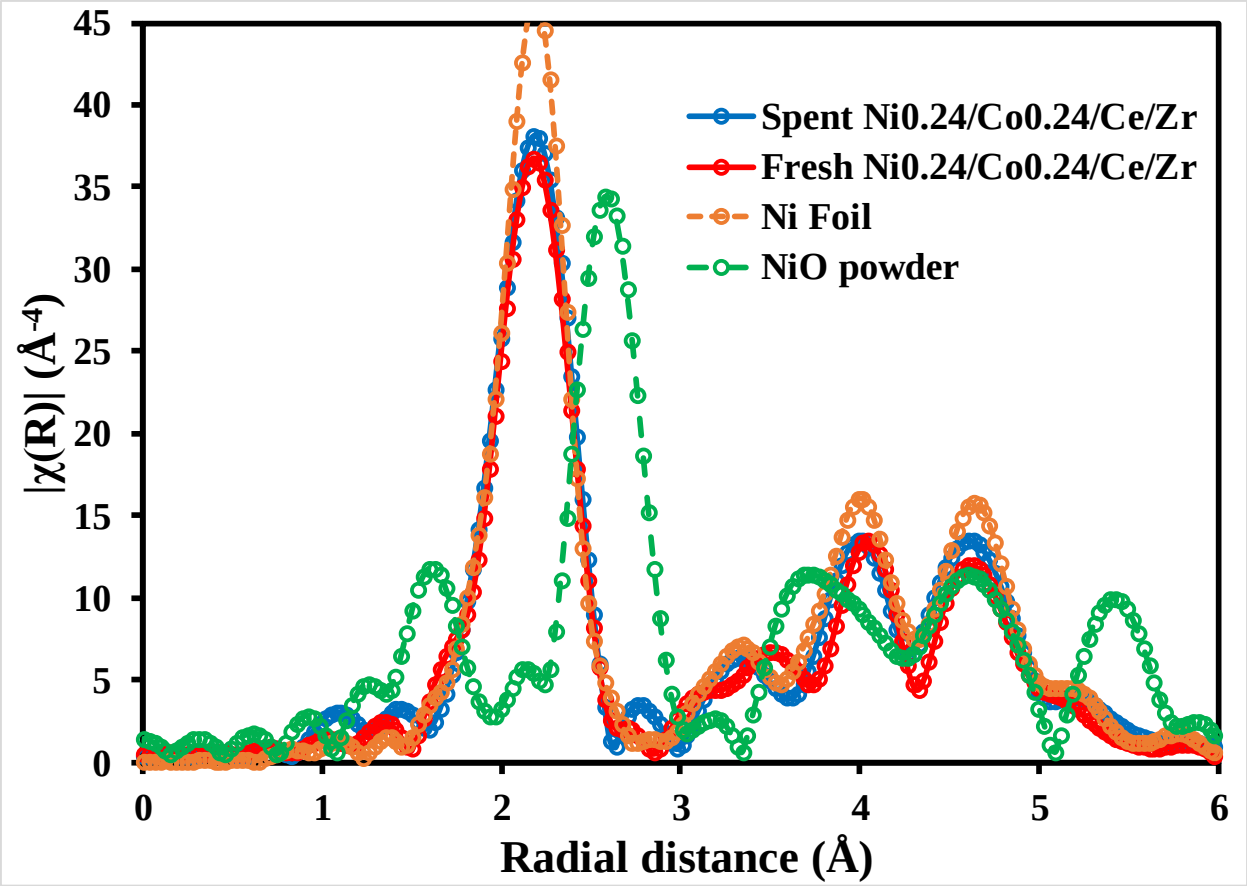

Figure D.16. The XAFS of fresh and spent Ni0.24/Co0.24/Ce/Zr.

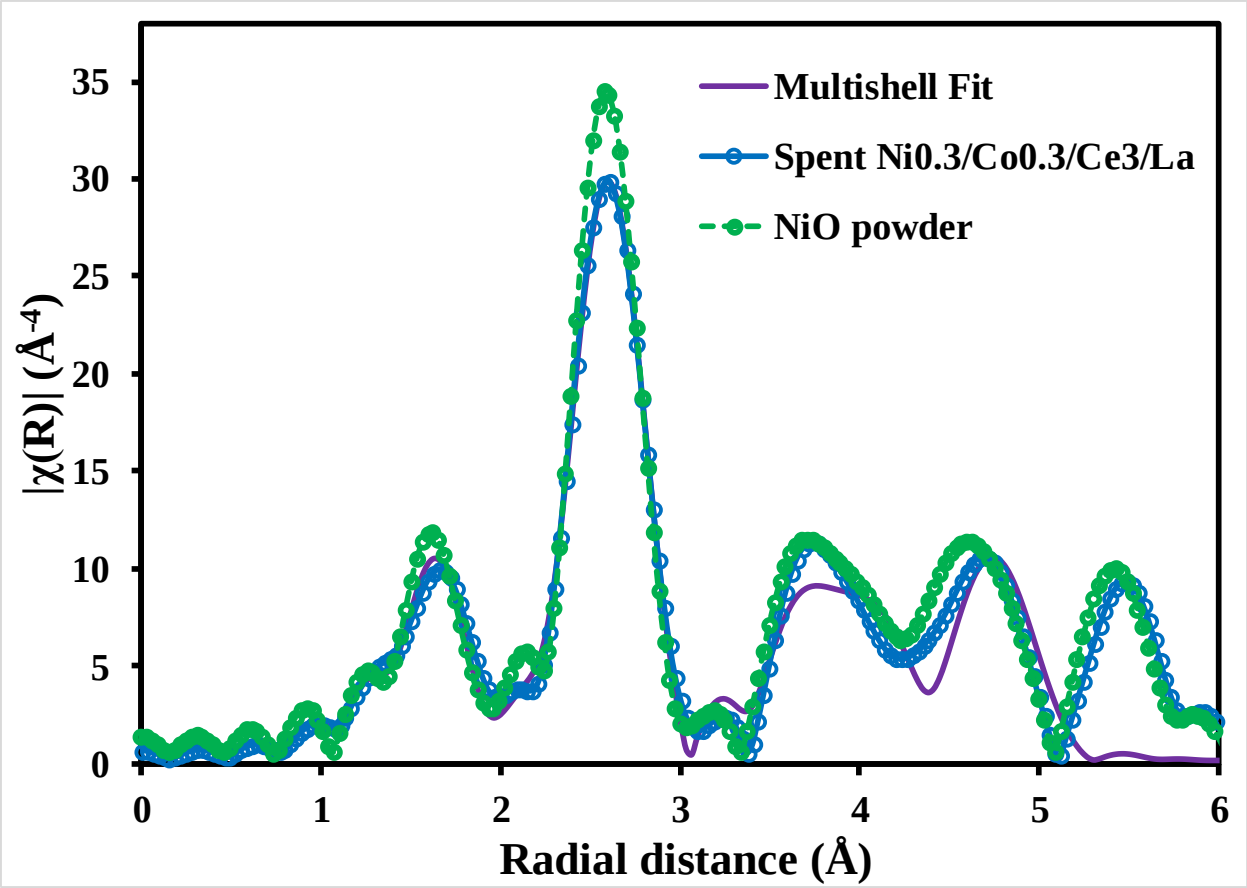

Figure D.17. The experimental and theoretical XAFS of spent Ni0.3/Co0.3/Ce3/La. Multi-shell fitting is 1-5 Å in R space.

# APPENDIX E. COPYRIGHT PERMISSION FILES

## E.1. Copyright Permission for Figure 1.1

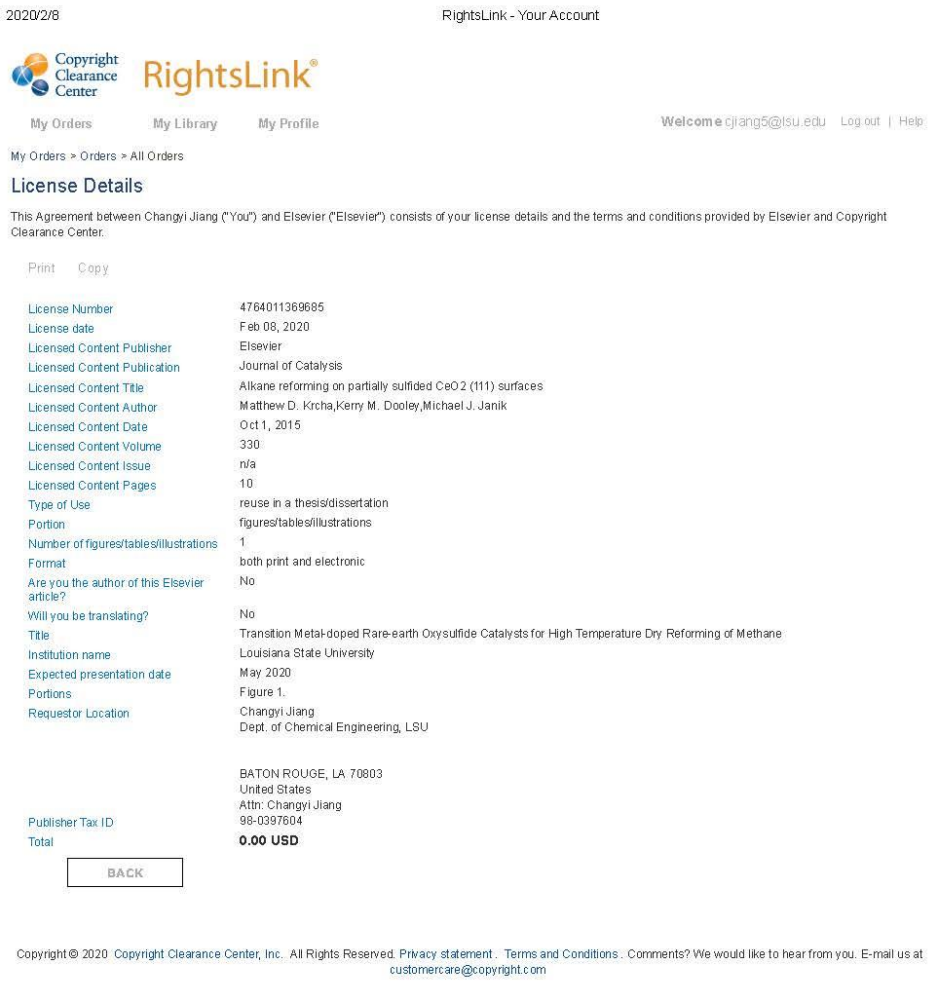

2020/2/8 RightsLink - Your Account

Copyright Clearance Center RightsLink®

My Orders My Library My Profile Welcome cjiang5@lsu.edu Log out | Help

My Orders > Orders > All Orders

License Details

This Agreement between Changyi Jiang ("You") and Elsevier ("Elsevier") consists of your license details and the terms and conditions provided by Elsevier and Copyright Clearance Center.

Print Copy

| | |
|---|---|
| License Number | 4764011369685 |
| License date | Feb 08, 2020 |
| Licensed Content Publisher | Elsevier |
| Licensed Content Publication | Journal of Catalysis |
| Licensed Content Title | Alkane reforming on partially sulfided CeO2 (111) surfaces |
| Licensed Content Author | Matthew D. Krcha,Kerry M. Dooley,Michael J. Janik |
| Licensed Content Date | Oct 1, 2015 |
| Licensed Content Volume | 330 |
| Licensed Content Issue | n/a |
| Licensed Content Pages | 10 |
| Type of Use | reuse in a thesis/dissertation |
| Portion | figures/tables/illustrations |
| Number of figures/tables/illustrations | 1 |
| Format | both print and electronic |
| Are you the author of this Elsevier article? | No |
| Will you be translating? | No |
| Title | Transition Metal-doped Rare-earth Oxysulfide Catalysts for High Temperature Dry Reforming of Methane |
| Institution name | Louisiana State University |
| Expected presentation date | May 2020 |
| Portions | Figure 1. |
| Requestor Location | Changyi Jiang<br>Dept. of Chemical Engineering, LSU<br><br>BATON ROUGE, LA 70803<br>United States<br>Attn: Changyi Jiang |
| Publisher Tax ID | 98-0397604 |
| Total | **0.00 USD** |

BACK

Copyright © 2020 Copyright Clearance Center, Inc. All Rights Reserved. Privacy statement. Terms and Conditions. Comments? We would like to hear from you. E-mail us at customercare@copyright.com

https://s100.copyright.com/MyAccount/viewLicenseDetails?ref=87b97e41-2cc2-457c-be35-a32a05026ba8 1/1

## E.2. Copyright Permission for Chapter 2



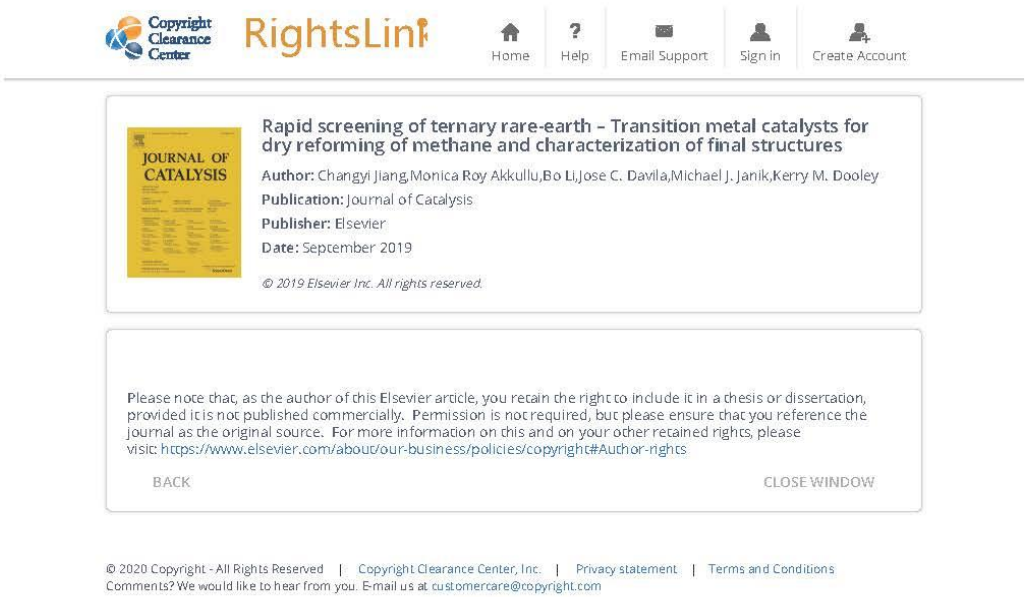

Rapid screening of ternary rare-earth – Transition metal catalysts for dry reforming of methane and characterization of final structures

**Author:** Changyi Jiang,Monica Roy Akkullu,Bo Li,Jose C. Davila,Michael J. Janik,Kerry M. Dooley
**Publication:** Journal of Catalysis
**Publisher:** Elsevier
**Date:** September 2019

© 2019 Elsevier Inc. All rights reserved.

Please note that, as the author of this Elsevier article, you retain the right to include it in a thesis or dissertation, provided it is not published commercially. Permission is not required, but please ensure that you reference the journal as the original source. For more information on this and on your other retained rights, please visit: https://www.elsevier.com/about/our-business/policies/copyright#Author-rights

BACK CLOSE WINDOW

© 2020 Copyright - All Rights Reserved | Copyright Clearance Center, Inc. | Privacy statement | Terms and Conditions
Comments? We would like to hear from you. E-mail us at customercare@copyright.com

## E.3. Copyright Permission for Figure 3.13



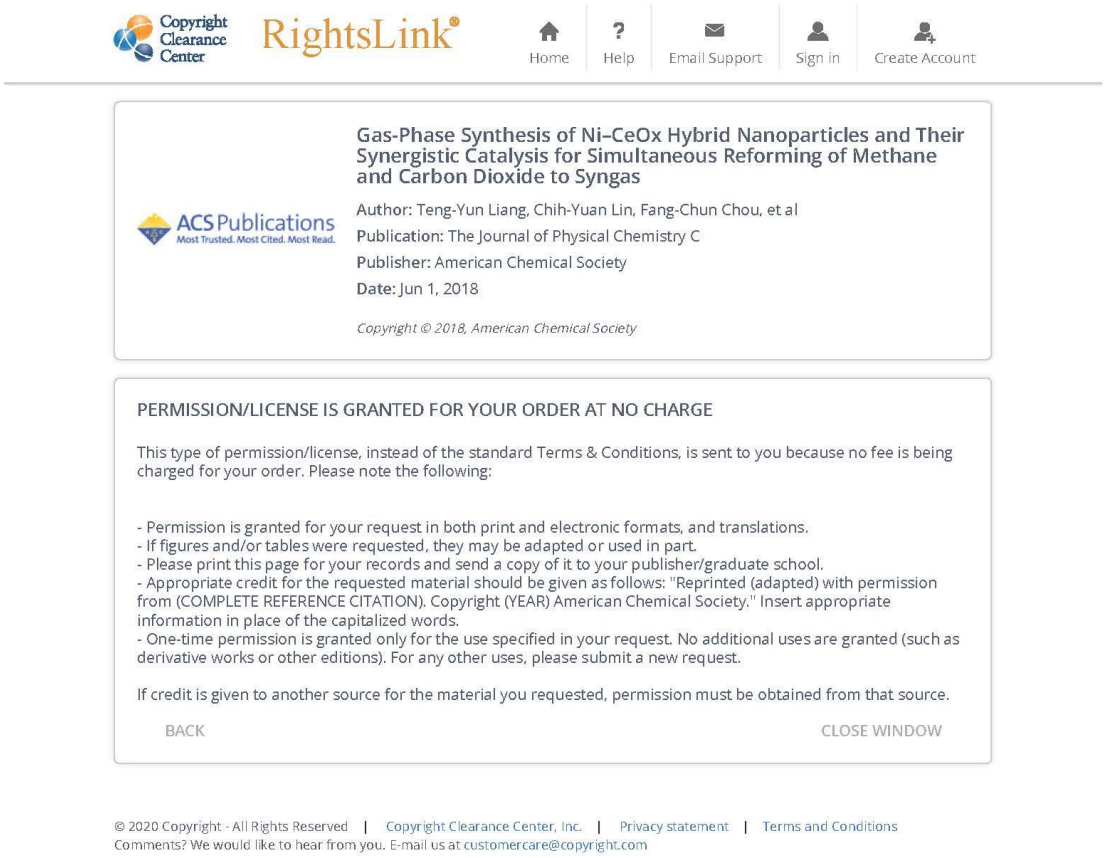

Copyright Clearance Center RightsLink®

Home | Help | Email Support | Sign in | Create Account

ACS Publications
Most Trusted. Most Cited. Most Read.

**Gas-Phase Synthesis of Ni–CeOx Hybrid Nanoparticles and Their Synergistic Catalysis for Simultaneous Reforming of Methane and Carbon Dioxide to Syngas**

**Author:** Teng-Yun Liang, Chih-Yuan Lin, Fang-Chun Chou, et al
**Publication:** The Journal of Physical Chemistry C
**Publisher:** American Chemical Society
**Date:** Jun 1, 2018

*Copyright © 2018, American Chemical Society*

PERMISSION/LICENSE IS GRANTED FOR YOUR ORDER AT NO CHARGE

This type of permission/license, instead of the standard Terms & Conditions, is sent to you because no fee is being charged for your order. Please note the following:

- Permission is granted for your request in both print and electronic formats, and translations.
- If figures and/or tables were requested, they may be adapted or used in part.
- Please print this page for your records and send a copy of it to your publisher/graduate school.
- Appropriate credit for the requested material should be given as follows: "Reprinted (adapted) with permission from (COMPLETE REFERENCE CITATION). Copyright (YEAR) American Chemical Society." Insert appropriate information in place of the capitalized words.
- One-time permission is granted only for the use specified in your request. No additional uses are granted (such as derivative works or other editions). For any other uses, please submit a new request.

If credit is given to another source for the material you requested, permission must be obtained from that source.

BACK CLOSE WINDOW

© 2020 Copyright - All Rights Reserved | Copyright Clearance Center, Inc. | Privacy statement | Terms and Conditions
Comments? We would like to hear from you. E-mail us at customercare@copyright.com

# REFERENCES


1. Bradford, M. C. J.; Vannice, M. A., $CO_2$ reforming of $CH_4$. *Catalysis Reviews-Science and Engineering* **1999,** *41* (1), 1-42.

2. Hu, Y. H.; Ruckenstein, E., Catalytic conversion of methane to synthesis gas by partial oxidation and CO2 reforming. *Advances in Catalysis, Vol 48* **2004,** *48*, 297-345.

3. Zhang, G.; Su, A.; Du, Y.; Qu, J.; Xu, Y., Catalytic performance of activated carbon supported cobalt catalyst for $CO_2$ reforming of $CH_4$. *Journal of Colloid and Interface Science* **2014,** *433*, 149-155.

4. WebBook, N. C. http://webbook.nist.gov/chemistry.

5. Gadalla, A. M.; Bower, B., The role of catalyst support on the activity of nickel for reforming methane with $CO_2$. *Chemical Engineering Science* **1988,** *43* (11), 3049-3062.

6. Reitmeier, R. E.; Atwood, K.; Bennett, H.; Baugh, H., Production of Synthetic Gas - Reaction of Light Hydrocarbons with Steam and Carbon Dioxide. *Industrial & Engineering Chemistry* **1948,** *40* (4), 620-626.

7. Valderrama, G.; Goldwasser, M. R.; Navarro, C. U. d.; Tatibouët, J. M.; Barrault, J.; Batiot-Dupeyrat, C.; Martínez, F., Dry reforming of methane over Ni perovskite type oxides. *Catalysis Today* **2005,** *107-108*, 785-791.

8. Rostrupnielsen, J. R.; Hansen, J. H. B., $CO_2$-Reforming of Methane over Transition Metals. *Journal of Catalysis* **1993,** *144* (1), 38-49.

9. Wang, S.; Lu, G. Q.; Millar, G. J., Carbon Dioxide Reforming of Methane To Produce Synthesis Gas over Metal-Supported Catalysts: State of the Art. *Energy & Fuels* **1996,** *10* (4), 896-904.

10. Nandini, A.; Pant, K. K.; Dhingra, S. C., Kinetic study of the catalytic carbon dioxide reforming of methane to synthesis gas over Ni-K/$CeO_2$-$Al_2O_3$ catalyst. *Applied Catalysis A: General* **2006,** *308*, 119-127.

11. Theofanidis, S. A.; Galvita, V. V.; Poelman, H.; Marin, G. B., Enhanced Carbon-Resistant Dry Reforming Fe-Ni Catalyst: Role of Fe. *ACS Catalysis* **2015,** *5* (5), 3028-3039.

12. Foo, S. Y.; Cheng, C. K.; Nguyen, T.-H.; Adesina, A. A., Kinetic study of methane $CO_2$ reforming on Co–Ni/$Al_2O_3$ and Ce–Co–Ni/$Al_2O_3$ catalysts. *Catal. Today* **2011,** *164*, 221-226.

13. Guo, J.; Lou, H.; Mo, L.; Zheng, X., The reactivity of surface active carbonaceous species with $CO_2$ and its role on hydrocarbon conversion reactions. *Journal of Molecular Catalysis A: Chemical* **2010,** *316* (1), 1-7.

14. Kambolis, A.; Matralis, H.; Trovarelli, A.; Papadopoulou, C., Ni/$CeO_2$-$ZrO_2$ catalysts for the dry reforming of methane. *Appl. Catal. A* **2010,** *377*, 16-26.

15. Bitter, J. H.; Seshan, K.; Lercher, J. A., Mono and Bifunctional Pathways of $CO_2$/$CH_4$ Reforming over Pt and Rh Based Catalysts. *Journal of Catalysis* **1998,** *176* (1), 93-101.

16. Eizenberg, M.; Blakely, J. M., Carbon monolayer phase condensation on Ni(111). *Surf. Sci.* **1979,** *82* (1), 228-236.

17. Bengaard, H. S.; Nørskov, J. K.; Sehested, J.; Clausen, B. S.; Nielsen, L. P.; Molenbroek, A. M.; Rostrup-Nielsen, J. R., Steam Reforming and Graphite Formation on Ni Catalysts. *J. Catal.* **2002,** *209* (2), 365-384.

18. Schouten, F. C.; Gijzeman, O. L. J.; Bootsma, G. A., Reaction of methane with nickel single crystal surfaces and the stability of surface nickel carbides. *Bulletin des Sociétés Chimiques Belges* **1979,** *88* (7‐8), 541-547.

19. Wang, S.; Lu, G. Q., Role of $CeO_2$ in Ni/CeO2–Al2O3 catalysts for carbon dioxide reforming of methane. *Applied Catalysis B: Environmental* **1998,** *19* (3), 267-277.

20. Wang, S.; Lu, G. Q., Effects of promoters on catalytic activity and carbon deposition of Ni/$\gamma$-$Al_2O_3$ catalysts in $CO_2$ reforming of $CH_4$. *Journal of Chemical Technology & Biotechnology* **2000,** *75* (7), 589-595.

21. Laosiripojana, N.; Assabumrungrat, S., Methane steam reforming over Ni/Ce–ZrO2 catalyst: Influences of Ce–ZrO2 support on reactivity, resistance toward carbon formation, and intrinsic reaction kinetics. *Appl. Catal. A* **2005,** *290*, 200-211.

22. Cui, H.; Turn, S. Q.; Reese, M. A., Removal of sulfur compounds from utility pipelined synthetic natural gas using modified activated carbons. *Catalysis Today* **2009,** *139* (4), 274-279.

23. De, S.; Zhang, J.; Luque, R.; Yan, N., Ni-based bimetallic heterogeneous catalysts for energy and environmental applications. *Energy & Environmental Science* **2016,** *9* (11), 3314-3347.

24. Moon, D. J.; Ryu, J. W.; Lee, S. D.; Lee, B. G.; Ahn, B. S., Ni-based catalyst for partial oxidation reforming of iso-octane. *Applied Catalysis A: General* **2004,** *272* (1), 53-60.

25. Kim, D. H.; Kang, J. S.; Lee, Y. J.; Park, N. K.; Kim, Y. C.; Hong, S. I.; Moon, D. J., Steam reforming of n-hexadecane over noble metal-modified Ni-based catalysts. *Catalysis Today* **2008,** *136* (3), 228-234.

26. Mancino, G.; Cimino, S.; Lisi, L., Sulphur poisoning of alumina supported Rh catalyst during dry reforming of methane. *Catalysis Today* **2016,** *277*, 126-132.

27. Pakhare, D.; Spivey, J., A review of dry ($CO_2$) reforming of methane over noble metal catalysts. *Chem Soc Rev* **2014,** *43* (22), 7813-37.

28. Seets, D. C.; Reeves, C. T.; Ferguson, B. A.; Wheeler, M. C.; Mullins, C. B., Dissociative chemisorption of methane on Ir(111): Evidence for direct and trapping-mediated mechanisms. *The Journal of Chemical Physics* **1997,** *107* (23), 10229-10241.

29. Bitter, J. H.; Seshan, K.; Lercher, J. A., On the contribution of X-ray absorption spectroscopy to explore structure and activity relations of $Pt/ZrO_2$ catalysts for $CO_2/CH_4$ reforming. *Topics in Catalysis* **2000,** *10* (3), 295-305.

30. Solymosi, F., The bonding, structure and reactions of $CO_2$ adsorbed on clean and promoted metal surfaces. *Journal of Molecular Catalysis* **1991,** *65* (3), 337-358.

31. Wambach, J.; Freund, H., $CO_2$ activation on transition metal surfaces. In *Carbon dioxide chemistry: environmental issues*, Athenaeum Press Stockholm: 1994; pp 31-43.

32. van Keulen, A. N. J.; Seshan, K.; Hoebink, J. H. B. J.; Ross, J. R. H., TAP investigations of the $CO_2$ reforming of $CH_4$ over $Pt/ZrO_2$. *J. Catal.* **1997,** *166*, 306-314.

33. Múnera, J. F.; Irusta, S.; Cornaglia, L. M.; Lombardo, E. A.; Vargas Cesar, D.; Schmal, M., Kinetics and reaction pathway of the $CO_2$ reforming of methane on Rh supported on lanthanum-based solid. *Journal of Catalysis* **2007,** *245* (1), 25-34.

34. Mark, M. F.; Maier, W. F., $CO_2$-Reforming of Methane on Supported Rh and Ir Catalysts. *Journal of Catalysis* **1996,** *164* (1), 122-130.

35. Yuan, K.; Zhong, J.-Q.; Zhou, X.; Xu, L.; Bergman, S. L.; Wu, K.; Xu, G. Q.; Bernasek, S. L.; Li, H. X.; Chen, W., Dynamic Oxygen on Surface: Catalytic Intermediate and Coking Barrier in the Modeled $CO_2$ Reforming of $CH_4$ on Ni (111). *ACS Catal.* **2016,** *6*, 4330-4339.

36. Pechimuthu, N. A.; Pant, K. K.; Dhingra, S. C.; Bhalla, R., Characterization and Activity of K, $CeO_2$, and Mn Promoted $Ni/Al_2O_3$ Catalysts for Carbon Dioxide Reforming of Methane. *Ind. Eng. Chem. Res.* **2006,** *45*, 7435-7443.

37. Bradford, M. C. J.; Vannice, M. A., Catalytic reforming of methane with carbon dioxide over nickel catalysts II. Reaction kinetics. *Applied Catalysis A: General* **1996,** *142* (1), 97-122.

38. Wang, H. Y.; Ruckenstein, E., $CH_4/CD_4$ Isotope Effect and the Mechanism of Partial Oxidation of Methane to Synthesis Gas over $Rh/\gamma\text{-}Al_2O_3$ Catalyst. *The Journal of Physical Chemistry B* **1999,** *103* (51), 11327-11331.

39. Holloway, S.; Lundqvist, B.; Nørskov, J. In *Electronic factors in catalysis*, Proceedings of the Eighth Conference on Catalysis, 1984; p 85.

40. Hammer, B.; Norskov, J. K., Why gold is the noblest of all the metals. *Nature* **1995,** *376* (6537), 238-240.

41. Nørskov, J. K.; Abild-Pedersen, F.; Studt, F.; Bligaard, T., Density functional theory in surface chemistry and catalysis. *Proceedings of the National Academy of Sciences* **2011,** *108* (3), 937.

42. Nilsson, A.; Pettersson, L. G. M.; Hammer, B.; Bligaard, T.; Christensen, C. H.; Nørskov, J. K., The electronic structure effect in heterogeneous catalysis. *Catalysis Letters* **2005,** *100* (3), 111-114.

43. Abild-Pedersen, F.; Lytken, O.; Engbæk, J.; Nielsen, G.; Chorkendorff, I.; Nørskov, J. K., Methane activation on Ni(111): Effects of poisons and step defects. *Surf. Sci.* **2005,** *590* (2), 127-137.

44. Liu, H.; Zhang, R.; Yan, R.; Wang, B.; Xie, K., $CH_4$ dissociation on NiCo (111) surface: A first-principles study. *Applied Surface Science* **2011,** *257* (21), 8955-8964.

45. Ruban, A.; Hammer, B.; Stoltze, P.; Skriver, H. L.; Nørskov, J. K., Surface electronic structure and reactivity of transition and noble metals 1 Communication presented at the First Francqui Colloquium, Brussels, 19–20 February 1996. 1. *Journal of Molecular Catalysis A: Chemical* **1997,** *115* (3), 421-429.

46. Getsoian, A. B.; Zhai, Z.; Bell, A. T., Band-Gap Energy as a Descriptor of Catalytic Activity for Propene Oxidation over Mixed Metal Oxide Catalysts. *Journal of the American Chemical Society* **2014,** *136* (39), 13684-13697.

47. Khan, M. M.; Ansari, S. A.; Pradhan, D.; Han, D. H.; Lee, J.; Cho, M. H., Defect-Induced Band Gap Narrowed $CeO_2$ Nanostructures for Visible Light Activities. *Industrial & Engineering Chemistry Research* **2014,** *53* (23), 9754-9763.

48. Tatar, B.; Sam, E. D.; Kutlu, K.; Ürgen, M., Synthesis and optical properties of $CeO_2$ nanocrystalline films grown by pulsed electron beam deposition. *Journal of Materials Science* **2008,** *43* (15), 5102-5108.

49. van der Kolk, E.; Dorenbos, P., Systematic and Material Independent Variation of Electrical, Optical, and Chemical Properties of Ln Materials over the Ln Series (Ln = La, Ce, Pr, ..., Lu). *Chemistry of Materials* **2006,** *18* (15), 3458-3462.

50. Montini, T.; Melchionna, M.; Monai, M.; Fornasiero, P., Fundamentals and Catalytic Applications of $CeO_2$-Based Materials. *Chemical Reviews* **2016,** *116* (10), 5987-6041.

51. Scanlon, D. O.; Morgan, B. J.; Watson, G. W., The origin of the enhanced oxygen storage capacity of $Ce_{1-x}(Pd/Pt)_xO_2$. *Phys. Chem. Chem. Phys.* **2011,** *13*, 4279-4284.

52. Yao, H. C.; Yao, Y. F. Y., Ceria in automotive exhaust catalysts. I. Oxygen storage. *J. Catal.* **1984**, 254-265.

53. Madier, Y.; Descorme, C.; Le Govic, A. M.; Duprez, D., Oxygen Mobility in $CeO_2$ and $Ce_xZr(1-x)O_2$ Compounds: Study by CO Transient Oxidation and $^{18}O/^{16}O$ Isotopic Exchange. *J. Phys. Chem. B* **1999,** *103* (50), 10999-11006.

54. Rossignol, S.; Madier, Y.; Duprez, D., Preparation of zirconia-ceria soft materials. *Catal. Today* **1999,** *50* (2), 261-270.

55. Trovarelli, A.; Zamar, F.; Llorca, J.; de Leitenburg, C.; Dolcetti, G.; Kiss, J. T., Nanophase fluorite-structured CeO2-ZrO2 catalysts prepared by high-energy mechanical milling. *J. Catal.* **1997,** *169*, 490-502.

56. Kacimi, S.; Barbier, J.; Taha, R.; Duprez, D., Oxygen storage capacity of promoted $Rh/CeC_2$ catalysts. Exceptional behavior of $RhCu/CeO_2$. *Catalysis Letters* **1993,** *22* (4), 343-350.

57. Senftle, T. P.; van Duin, A. C. T.; Janik, M. J., Role of Site Stability in Methane Activation on $Pd_xCe_{1-x}O_\delta$ Surfaces. *ACS Catalysis* **2015,** *5* (10), 6187-6199.

58. Cen, W. L.; Liu, Y.; Wu, Z. B.; Wang, H. Q.; Weng, X. L., A theoretic insight into the catalytic activity promotion of $CeO_2$ surfaces by Mn doping. *Phys. Chem. Chem. Phys.* **2012,** *14*, 5769−5777.

59. Krcha, M. D.; Dooley, K. M.; Janik, M. J., Alkane reforming on partially sulfided $CeO_2$ (111) surfaces. *J. Catal.* **2015,** *330*, 167-176.

60. Yang, Z.; Luo, G.; Lu, Z.; Hermansson, K., Oxygen vacancy formation energy in Pd-doped ceria: A DFT + U study. *J. Chem. Phys.* **2007,** *127* (7), 074704-5.

61. Chen, H. T.; Chang, J. G., Oxygen vacancy formation and migration in $Ce_{1-x}Zr_xO_2$ catalyst: A DFT+U calculation. *J. Chem. Phys.* **2010,** *132*, 214702-1-6.

62. Fornasiero, P.; Dimonte, R.; Rao, G. R.; Kaspar, J.; Meriani, S.; Trovarelli, A.; Graziani, M., Rh-Loaded CeO2-ZrO2 Solid-Solutions as Highly Efficient Oxygen Exchangers: Dependence of the Reduction Behavior and the Oxygen Storage Capacity on the Structural-Properties. *J. Catal.* **1995,** *151* (1), 168-177.

63. Hori, C. E.; Permana, H.; Ng, K. Y. S.; Brenner, A.; More, K.; Rahmoeller, K. M.; Belton, D., Thermal stability of oxygen storage properties in a mixed $CeO_2$-$ZrO_2$ system. *Applied Catalysis B: Environmental* **1998,** *16* (2), 105-117.

64. Vidal, H.; Kašpar, J.; Pijolat, M.; Colon, G.; Bernal, S.; Cordón, A.; Perrichon, V.; Fally, F., Redox behavior of $CeO_2$–$ZrO_2$ mixed oxides: I. Influence of redox treatments on high surface area catalysts. *Applied Catalysis B: Environmental* **2000,** *27* (1), 49-63.

65. Boaro, M.; de Leitenburg, C.; Dolcetti, G.; Trovarelli, A., The Dynamics of Oxygen Storage in Ceria-Zirconia Model Catalysts Measured by CO Oxidation under Stationary and Cycling Feedstream Compositions. *J. Catal.* **2000,** *193* (2), 338-347.

66. Hu, Z.; Metiu, H., Effect of Dopants on the Energy of Oxygen-Vacancy Formation at the Surface of Ceria: Local or Global? *The Journal of Physical Chemistry C* **2011,** *115* (36), 17898-17909.

67. Kim, K.; Yoo, J. D.; Lee, S.; Bae, M.; Bae, J.; Jung, W.; Han, J. W., A Simple Descriptor to Rapidly Screen CO Oxidation Activity on Rare-Earth Metal-Doped $CeO_2$: From Experiment to First-Principles. *ACS Applied Materials & Interfaces* **2017,** *9* (18), 15449-15458.

68. Kumar, G.; Lau, S. L. J.; Krcha, M. D.; Janik, M. J., Correlation of Methane Activation and Oxide Catalyst Reducibility and Its Implications for Oxidative Coupling. *ACS Catalysis* **2016,** *6* (3), 1812-1821.

69. Spivey, J. J., Chapter 10 - Deactivation of Reforming Catalysts. In *Fuel Cells: Technologies for Fuel Processing*, Shekhawat, D.; Spivey, J. J.; Berry, D. A., Eds. Elsevier: Amsterdam, 2011; pp 285-315.

70. Boldrin, P.; Ruiz-Trejo, E.; Mermelstein, J.; Bermúdez Menéndez, J. M.; Ramírez Reina, T.; Brandon, N. P., Strategies for Carbon and Sulfur Tolerant Solid Oxide Fuel Cell Materials, Incorporating Lessons from Heterogeneous Catalysis. *Chemical Reviews* **2016,** *116* (22), 13633-13684.

71. Rostrup-Nielsen, J.-R., Sulfur-Passivated Nickel Catalysts for Carbon-Free Steam Reforming of Methane. *J. Catal.* **1984,** *85*, 31-43.

72. Laycock, C. J.; Staniforth, J. Z.; Ormerod, R. M., Biogas as a fuel for solid oxide fuel cells and synthesis gas production: effects of ceria-doping and hydrogen sulfide on the performance of nickel-based anode materials. *Dalton Trans.* **2011,** *40* (20), 5494-5504.

73. Sato, K.; Shinoda, T.; Fujimoto, K., New nickel-based catalyst for tar reforming, with superior resistance to coking and sulfur poisoning in biomass gasification processes. *J. Chem. Eng. Japan* **2007,** *40*, 860-868.

74. Wang , L.; Murata, K.; Inaba, M., Highly efficient conversion of gasoline into hydrogen on $Al_2O_3$-supported Ni-based catalysts: Catalyst stability enhancement by modification with W. *Appl. Catal. A* **2009,** *358*, 264-268.

75. Qi, A.; Wang, S.; Fu, G.; Ni, C.; Wu, D., La-Ce-Ni-O monolithic perovskite catalysts potential for gasoline autothermal reforming system. *Appl. Catal. A* **2005,** *281* (1-2), 233-246.

76. Yu, F.; Yue, B.; Wang, X.; Geng, S.; Lu, X.; Ding, W., Hydrocracking of Tar Components from Hot Coke Oven Gas over a Ni/Ce-$ZrO_2$/γ-$Al_2O_3$ Catalyst at Atmospheric Pressure. *Chin. J. Catal.* **2009,** *30* (7), 690-696.

77. Murata, K.; Saito, M.; Inaba, M.; Takahara, I., Hydrogen production by autothermal reforming of sulfur-containing hydrocarbons over re-modified Ni/Sr/$ZrO_2$ catalysts. *Appl. Catal. B* **2007,** *70*, 509-514.

78. Wang, L.; Murata, K.; Matsumura, Y.; Inaba, M., Lower-Temperature Catalytic Performance of Bimetallic Ni-Re/$Al_2O_3$ Catalyst for Gasoline Reforming to Produce Hydrogen with the Inhibition of Methane Formation. *Energy & Fuels* **2006,** *20*, 1377-1381.

79. Li, C.; Hirabayashi, D.; Suzuki, K., A crucial role of $O_2^-$ and $O_2^{2-}$ on mayenite structure for biomass tar steam reforming over Ni/$Ca_{12}Al_{14}O_{33}$. *Appl. Catal. B* **2009,** *88* (3-4), 351-360.

80. Wang, L.; Murata, K.; Inaba, M., Control of the product ratio of $CO_2$/(CO + $CO_2$) and inhibition of catalyst deactivation for steam reforming of gasoline to produce hydrogen. *Appl. Catal. B* **2004,** *48*, 243-248.

81. Tan, C. D.; Baker, R. T. K., The effect of various sulfides on carbon deposition on nickel–iron particles. *Catal. Today* **2000,** *63*, 3-20.

82. Jazayeri, S. M.; Karimzadeh, R., Experimental Investigation of Initial Coke Formation over Stainless Steel, Chromium, and Iron in Thermal Cracking of Ethane with Hydrogen Sulfide as an Additive. *Energy & Fuels* **2011,** *25* (10), 4235-4247.

83. Venkataraman, R.; Eser, S., Characterization of Solid Deposits Formed from Jet Fuel Degradation under Pyrolytic Conditions: Metal Sulfides. *Ind. Eng. Chem. Res.* **2008,** *47*, 9351-9360.

84. M. Gaddalla, A.; E. Sommer, M., Carbon dioxide reforming of methane on nickel catalysts. *Chemical Engineering Science* **1989,** *44* (12), 2825-2829.

85. Seo, H. O., Recent Scientific Progress on Developing Supported Ni Catalysts for Dry ($CO_2$) Reforming of Methane. *Catalysts* **2018,** *8* (3), 110.

86. Nandini, A.; Pant, K. K.; Dhingra, S. C., K-, $CeO_2$-, and Mn-promoted Ni/$Al_2O_3$ catalysts for stable $CO_2$ reforming of methane. *Applied Catalysis A* **2005,** *290*, 166-174.

87. Wang, H.; Miller, J. T.; Shakouria, M.; Xia, C.; Wu, T.; Zhao, H.; Cem Akatay, M., XANES and EXAFS studies on metal nanoparticle growth and bimetallic interaction of Ni-based catalysts for $CO_2$ reforming of $CH_4$. *Catal. Today* **2013,** *207*, 3-12.

88. Misture, S. T.; McDevitt, K. M.; Glass, K. C.; Edwards, D. D.; Howe, J. Y.; Rector, K. d.; Hec, H.; Vogel, S. C., Sulfur-resistant and regenerable Ni/Co spinelbased catalysts for methane dry reforming. *Catal. Sci. Technol., 2015* **2015,** *5*, 4565-4574.

89. Koubaissy, B.; Pietraszek, A.; Roger, A. C.; Kiennemann, A., $CO_2$ reforming of methane over Ce-Zr-Ni-Me mixed catalysts. *Catal. Today* **2010,** *157*, 436-439.

90. Liu, F.; Zhao, L.; Wang, H.; Bai, X.; Liu, Y., Study on the preparation of Ni–La–Ce oxide catalyst for steam reforming of ethanol. *International Journal of Hydrogen Energy* **2014,** *39* (20), 10454-10466.

91. Stagg, S. M.; Resasco, D. E., Effects of promoters and supports on coke formation on Pt catalysts during CH4 reforming with CO2. In *Studies in Surface Science and Catalysis*, Bartholomew, C. H.; Fuentes, G. A., Eds. Elsevier: 1997; Vol. 111, pp 543-550.

92. Bartholomew, C. H.; Weatherbee, G. D.; Jarvi, G. A., EFFECTS OF CARBON DEPOSITS ON THE SPECIFIC ACTIVITY OF NICKEL AND NICKEL BIMETALLIC CATALYSTS. *Chemical Engineering Communications* **1980,** *5* (1-4), 125-134.

93. Foo, S. Y.; Cheng, C. K.; Nguyen, T.-H.; Adesina, A. A., Evaluation of lanthanide-group promoters on Co–Ni/$Al_2O_3$ catalysts for $CH_4$ dry reforming. *Journal of Molecular Catalysis A: Chemical* **2011,** *344* (1), 28-36.

94. Osojnik Crnivec, I. G.; P. Djinovic´, P.; Erjavec, B.; Pintar, A., Effect of synthesis parameters on morphology and activity of bimetallic catalysts in $CO_2$–$CH_4$ reforming. *Chem. Eng. J.* **2012,** *207-208*, 299-307.

95. Gonzalez-delaCruz, V. M.; Pereniguez, R.; Ternero, F.; Holgado, J. P.; Caballero, A., In Situ XAS Study of Synergic Effects on Ni-Co/$ZrO_2$ Methane Reforming Catalysts. *J. Phys. Chem. C* **2012,** *116*, 2919-2926.

96. Staudt, T.; Lykhach, Y.; Tsud, N.; Skála, T.; Prince, K. C.; Matolín, V.; Libuda, J., Ceria reoxidation by $CO_2$: A model study. *Journal of Catalysis* **2010,** *275* (1), 181-185.

97. Mamontov, E.; Egami, T., Structural defects in a nano-scale powder of $CeO_2$ studied by pulsed neutron diffraction. *Journal of Physics and Chemistry of Solids* **2000,** *61* (8), 1345-1356.

98. Jin, T.; Zhou, Y.; Mains, G. J.; White, J. M., Infrared and x-ray photoelectron spectroscopy study of carbon monoxide and carbon dioxide on platinum/ceria. *The Journal of Physical Chemistry* **1987,** *91* (23), 5931-5937.

99. Kim, D. K.; Stöwe, K.; Müller, F.; Maier, W. F., Mechanistic study of the unusual catalytic properties of a new NiCe mixed oxide for the $CO_2$ reforming of methane. *Journal of Catalysis* **2007,** *247* (1), 101-111.

100. Asencios, Y. J. O.; Bellido, J. D. A.; Assaf, E. M., Synthesis of NiO–MgO–$ZrO_2$ catalysts and their performance in reforming of model biogas. *Applied Catalysis A: General* **2011,** *397* (1), 138-144.

101. Djinović, P.; Osojnik Črnivec, I. G.; Erjavec, B.; Pintar, A., Influence of active metal loading and oxygen mobility on coke-free dry reforming of Ni–Co bimetallic catalysts. *Applied Catalysis B: Environmental* **2012,** *125*, 259-270.

102. Wang, J.; Shen, M.; Wang, J.; Yang, M.; Wang, W.; Ma, J.; Jia, L., Effects of Ni-doping of ceria-based materials on their micro-structures and dynamic oxygen storage and release behaviors. *Catalysis letters* **2010,** *140* (1-2), 38-48.

103. Hirano, M. A.; Suda, J., Oxygen storage capacity, specific surface area, and pore size distribution of ceria-zirconia solid solutions directly formed by thermal hydrolysis. *J. Am. Ceram. Soc.* **2003,** *86*, 2209-2211.

104. Shah, P. R.; Kim, T.; Zhou, G.; Fornasiero, P.; Gorte, R. J., Evidence for Entropy Effects in the Reduction of Ceria-Zirconia Solutions. *Chem. Mater.* **2006,** *18*, 5363-5369.

105. Zhou, G.; Shah, P. R.; Kim, T.; Fornasiero, P.; Gorte, R. J., Oxidation entropies and enthalpies of ceria-zirconia solid solutions. *Catal. Today* **2007,** *123* (1-4), 86-93.

106. Kim, T.; Vohs, J. M.; Gorte, R. J., Thermodynamic Investigation of the Redox Properties of Ceria-Zirconia Solid Solutions. *Ind. Eng. Chem. Res.* **2006,** *45*, 5561-5565.

107. Roh, H.-S.; Potdar, H. S.; Jun, K.-W.; Kim, J.-W.; Oh, Y.-S., Carbon dioxide reforming of methane over Ni incorporated into Ce–$ZrO_2$ catalysts. *Applied Catalysis A* **2004,** *276*, 231-239.

108. Pino, L.; Vita, A.; Cipitì, F.; Laganà, M.; Recupero, V., Hydrogen production by methane tri-reforming process over Ni–ceria catalysts: Effect of La-doping. *Appl. Catal. B: Environ.* **2011,** *104*, 64-73.

109. Sukonket, T.; Khan, A.; Saha, B.; Ibrahim, H.; Tantayanon, S.; Kumar, P.; Idem, R., Influence of the Catalyst Preparation Method, Surfactant Amount, and Steam on $CO_2$ Reforming of $CH_4$ over 5Ni/Ce0.6Zr0.4$O_2$ Catalysts. *Energy Fuels* **2011,** *25*, 864-877.

110. Terribile, D.; Trovarelli, A.; Llorca, J.; de Leitenburg, C.; Dolcetti, G., The synthesis and characterization of mesoporous high-surface area ceria prepared using a hybrid organic/inorganic route. *J. Catal.* **1998,** *178*, 299-308.

111. Dooley, K. M.; Kalakota, V.; Adusumilli, S., High-Temperature Desulfurization of Gasifier Effluents with Rare Earth and Rare Earth/Transition Metal Oxides. *Energy Fuels* **2011,** *25* (3), 1213-1220.

112. Colon, G.; Navio, J. A.; Monaci, R.; Ferino, I., $CeO_2$-$La_2O_3$ catalytic system. Part I: Preparation and characterisation of catalysts *Phys. Chem. Chem. Phys.* **2000,** *2*, 4453-4459.

113. Ravel, B.; Newville, M., Athena, artemis, hephaestus: Data analysis for x-ray absorption spectroscopy using ifeffit. *J. Synchrotron Radiat.* **2005,** *12*, 537-541.

114. Kresse, G.; Furthmuller, J., Efficiency of ab-initio total energy calculations for metals and semiconductors using a plane-wave basis set. *Comput. Mater. Sci.* **1996,** *6*, 15-50.

115. Kresse, G.; Furthmuller, J., Efficient iterative schemes for ab initio total-energy calculations using a plane wave basis set. *Phys. Rev. B* **1996,** *54* (16), 11169-11186.

116. Kresse, G.; Hafner, J., Ab initio molecular dynamics for liquid metals. *Phys. Rev. B* **1993,** *47* (1), 558-561.

117. Kresse, G.; Joubert, D., From ultrasoft pseudopotentials to the projector augmented-wave method. *Phys. Rev. B* **1999,** *59* (3), 1758 LP - 1775.

118. Perdew, J. P.; Burke, K.; Ernzerhof, M., Generalized Gradient Approximation Made Simple. *Phys Rev Lett* **1996,** *77* (18), 3865-3868.

119. Fabris, S.; Gironcoli, S. d.; Baroni, S.; Vicario, G.; Balducci, G., Taming multiple valency with density functionals: A case study of defective ceria. *Phys. Rev. B* **2005,** *71*, 041102.

120. Fabris, S.; Gironcoli, S. d.; Baroni, S.; Vicario, G.; Balducci, G., Reply to "Comment on 'Taming multiple valency with density functionals: A case study of defective ceria". *Phys. Rev. B* **2005,** *72*, 237102.

121. Kresse, G.; Blaha, P.; Silva, J. L. F. D.; Ganduglia-Pirovano, M. V., Comment on "Taming multiple valency with density functionals: A case study of defective ceria". *Phys. Rev. B* **2005,** *72*, 237101.

122. Herbst, J. F.; Watson, R. E.; Wilkins, J. W., Relativistic calculations of 4f excitation energies in the rare-earth metals: Further results. *Phys. Rev. B* **1978,** *17* (8), 3089 LP - 3098.

123. Anisimov, V. I.; Gunnarsson, O., Density-Functional Calculation of Effective Coulomb Interactions in Metals. *Physical Review B* **1991,** *43* (10), 7570-7574.

124. Mayernick, A. D.; Janik, M. J., Methane Activation and Oxygen Vacancy Formation over $CeO_2$ and Zr, Pd Substituted $CeO_2$ Surfaces. *J. Phys. Chem. C* **2008,** *112* (38), 14955-14964.

125. Mayernick, A. D.; Janik, M. J., Ab initio thermodynamic evaluation of Pd atom interaction with $CeO_2$ surfaces. *J. Chem. Phys.* **2009,** *131*, 084701.

126. Mayernick, A. D.; Janik, M. J., Methane oxidation on Pd-Ceria: A DFT study of the mechanism over PdxCe1-x$O_2$, Pd, and PdO. *J. Catal.* **2011,** *278*, 16-25.

127. Mayernick, A. D.; Li, R.; Dooley, K. M.; Janik, M. J., Energetics and Mechanism for $H_2S$ Adsorption by Ceria-Lanthanide Mixed Oxides: Implications for the Desulfurization of Biomass Gasifier Effluents. *J. Phys. Chem. C* **2011,** *115* (49), 24178-24188.

128. Krcha, M. D.; Janik, M. J., Examination of Oxygen Vacancy Formation in Mn-Doped $CeO_2$ (111) using DFT+U and the Hybrid Functional HSE06. *Langmuir* **2013,** *29*, 10120-10131.

129. Krcha, M. D.; Janik, M. J., Catalytic propane reforming mechanism over Zr-doped $CeO_2$ (111). *Catalysis Science & Technology* **2014,** *4* (9), 3278-3289.

130. Krcha, M. D.; Janik, M. J., Catalytic propane reforming mechanism over Mn-Doped $CeO_2$ (111). *Surf. Sci.* **2015,** *640*, 119-126.

131. Krcha, M. D.; Mayernick, A. D.; Janik, M. J., Periodic trends of oxygen vacancy formation and C–H bond activation over transition metal-doped $CeO_2$ (111) surfaces. *J. Catal.* **2012,** *293*, 103-115.

132. Cinquini, F.; Giordano, L.; Pacchioni, G.; Ferrari, A. M.; Pisani, C.; Roetti, C., Electronic structure of NiO/Ag(100) thin films from DFT+U and hybrid functional DFT approaches. *Physical Review B* **2006,** *74* (16), 165403.

133. Wilkes, M. F.; Hayden, P.; Bhattacharya, A. K., Catalytic studies on ceria lanthana solid solutions. III. Surface segregation and solid state studies. *J. Catal.* **2003,** *219*, 305-309.

134. Belliere, V.; Joorst, G.; Stephan, O.; de Groot, F. M. F.; Weckhuysen, B. M., Phase Segregation in Cerium-Lanthanum Solid Solutions. *J. Phys. Chem. B* **2006,** *110*, 9984-9990.

135. Dantas, S. C.; Escritori, J. C.; Soares, R. R.; Hori, C. E., Effect of different promoters on $Ni/CeZrO_2$ catalyst for autothermal reforming and partial oxidation of methane. *Chemical Engineering Journal* **2010,** *156* (2), 380-387.

136. Singhania, A., High Surface Area M (M = La, Pr, Nd, and Pm)-Doped Ceria Nanoparticles: Synthesis, Characterization, and Activity Comparison for CO Oxidation. *Ind. Eng. Chem. Res.* **2017,** *56*, 13594-13601.

137. Rossignol, S.; Gerard, F.; Mesnard, D.; Kappenstein, C.; Duprez, D., Structural changes of Ce–Pr–O oxides in hydrogen: a study by in situ X-ray diffraction and Raman spectroscopy. *J. Mater. Chem.* **2003,** *13* (13), 3017-3020.

138. Zhao, B.; Li, G.; Ge, C.; Wanga, Q.; Zhou, R., Preparation of $Ce_{0.67}Zr_{0.33}O_2$ mixed oxides as supports of improved Pd-only three-way catalysts. *Applied Catalysis B: Environmental* **2010,** *96*, 338-349.

139. Bensaid, S.; Piumetti, M.; Novara, C.; Giorgis, F.; Chiodoni, A.; Russo, N.; Fino, D., Catalytic Oxidation of CO and Soot over Ce-Zr-Pr Mixed Oxides Synthesized in a Multi-Inlet Vortex Reactor: Effect of Structural Defects on the Catalytic Activity. *Nanoscale Research Letters* **2016,** *11*, 494-1 - 494-14.

140. Weber, W. H.; Bass, K. C.; McBride, J. R., Raman study of $CeO_2$. Second-order scattering, lattice dynamics, and particle-size effects. *Phys. Rev. B* **1993,** *48*, 178-185.

141. McBride, J. R.; Hass, K. C.; Poindexter, B. D.; Weber, W. H., Raman and X-ray studies of $Ce_{1-x}RE_xO_{2-y}$ where RE = La, Pr, Nd, Eu, Gd and Tb. *J. Appl. Phys.* **1994,** *76*, 2435-3441.

142. Malecka, M. A.; Kepinski, L.; Mista, W., Structure evolution of nanocrystalline $CeO_2$ and $CeLnO_x$ mixed oxides (Ln = Pr, Tb, Lu) in $O_2$ and $H_2$ atmosphere and their catalytic activity in soot combustion. *Appl. Catal. B* **2007,** *74* (3-4), 290-298.

143. Reddy, B. M.; Khan, A.; Yamada, Y.; Kobayashi, T.; Loridant, S.; Volta, J.-C., Structual characterization of CeO2-MO2 (M = Si4+, Ti4+, and Zr4+) mixed oxides by Raman

Spectroscopy, X-ray photoelectron spectroscopy and other techniques. *J. Phys. Chem.* **2003,** *107*, 11475-11484.

144. Spanier, J. E.; Robinson, R. D.; Zhang, F.; Chan, S.-W.; Herman, I. P., Size dependent properties of $CeO_{2-y}$ nanoparticles as studied by Raman scattering. *Phys. Rev. B* **2001,** *64* (245407), 1-8.

145. Krishna, K.; Bueno-Lopez, A.; Makkee, M.; Moulijn, J. A., Potential rare earth modified $CeO_2$ catalysts for soot oxidation. I. Characterisation and catalytic activity with $O_2$. *Appl. Catal. B* **2007,** *75*, 189-200.

146. Reddy, B. M.; Bharali, P.; Saikia, P.; Park, S.-E.; van den Berg, M. W. E.; Muhler, M.; Gruner, W., Structural Characterization and Catalytic Activity of Nanosized $Ce_xM_{1-x}O_2$ (M ) Zr and Hf) Mixed Oxides. *J. Phys. Chem. C* **2008,** *112*, 11729-11737.

147. Löfberg, A.; Guerrero-Caballero, J.; Kane, T.; Rubbens, A.; Jalowiecki-Duhamel, L., $Ni/CeO_2$ based catalysts as oxygen vectors for the chemical looping dry reforming of methane for syngas production. *Applied Catalysis B: Environmental* **2017,** *212*, 159-174.

148. Maher , R. C.; Shearing , P. R.; Brightman , E.; Brett , D. J. L.; Brandon, N. P.; Cohen, L. F., Reduction Dynamics of Doped Ceria, Nickel Oxide, and Cermet Composites Probed Using In Situ Raman Spectroscopy. *Adv. Sci.* **2016,** *3*, 1500146-1 - 1500146-8.

149. Reddy, B.; Thrimurthulu, G.; Katta, L., Design of Efficient CeMO (M = Zr, Hf, Tb and Pr) Nanosized Model Solid Solutions for CO Oxidation. *Catalysis Letters* **2011,** *141* (4), 572-581.

150. Mullins, D. R.; Overbury, S. H.; Huntley, D. R., Electron spectroscopy of single crystal and polycrystalline cerium oxide surfaces. *Surf. Sci.* **1998,** *409* (2), 307-319.

151. Fagg, D.; Frade, J.; Kharton, V.; Marozau, I., The defect chemistry of Ce (Pr, Zr) $O_{2-\delta}$. *Journal of Solid State Chemistry* **2006,** *179* (5), 1469-1477.

152. Hasegawa, T.; Shahed, S. M. F.; Sainoo, Y.; Beniya, A.; Isomura, N.; Watanabe, Y.; Komeda, T., Epitaxial growth of $CeO_2$(111) film on Ru(0001): Scanning tunneling microscopy (STM) and x-ray photoemission spectroscopy (XPS) study. *The Journal of Chemical Physics* **2014,** *140* (4), 044711.

153. Hu, Z.; Liu, X.; Meng, D.; Guo, Y.; Guo, Y.; Lu, G., Effect of ceria crystal plane on the physicochemical and catalytic properties of Pd/ceria for CO and propane oxidation. *ACS Catalysis* **2016,** *6* (4), 2265-2279.

154. Papaefthimiou, V.; Niakolas, D. K.; Paloukis, F.; Dintzer, T.; Zafeiratos, S., Is Steam an Oxidant or a Reductant for Nickel/Doped ‐ Ceria Cermets? *Chemphyschem* **2017,** *18* (1), 164-170.

155. Ivanov, A. S., Physicochemical and catalytic properties of systems based on $CeO_2$. *Kinet. Catal.* **2009,** *50* (6), 797-815.

156. McIntyre, N. S.; Cook, M. G., X-ray photoelectron studies on some oxides and hydroxides of cobalt, nickel, and copper. ***Analytical Chemistry*** **1975,** *47* (13), 2208-2213.

157. Mahammadunnisa, S.; Manoj Kumar Reddy, P.; Lingaiah, N.; Subrahmanyam, C., $NiO/Ce_{1-x}Ni_xO_{2-\delta}$ as an alternative to noble metal catalysts for CO oxidation. *Catalysis Science & Technology* **2013,** *3* (3), 730-736.

158. Li, X.; Li, X.; Zeng, X.; Zhu, T., Correlation between the physicochemical properties and catalytic performances of micro/mesoporous CoCeOx mixed oxides for propane combustion. *Appl. Catal. A, Gen.* **2019,** *572*, 61-70.

159. Song, C.; Pan, W., Tri-reforming of methane: a novel concept for catalytic production of industrially useful synthesis gas with desired $H_2$/CO ratios. *Catalysis Today* **2004,** *98* (4), 463-484.

160. Sengupta, P.; Khan, A.; Zahid, M. A.; Ibrahim, H.; Idem, R., Evaluation of the Catalytic Activity of Various $5Ni/Ce0_{.5}Zr_{0.33}M_{0.17}O_{2-\delta}$ Catalysts for Hydrogen Production by the Steam Reforming of a Mixture of Oxygenated Hydrocarbons. *Energy & Fuels* **2012,** *26* (2), 816-828.

161. Dong, W.-S.; Roh, H.-S.; Ki-Won Jun; Park, S.-E.; Oh, Y.-S., Methane reforming over $Ni/Ce-ZrO_2$ catalysts: effect of nickel content. *Appl. Catal. A: General* **2002,** *226*, 63-72.

162. Walker, D. M.; Pettit, S. L.; Wolan, J. T.; Kuhn, J. N., Synthesis gas production to desired hydrogen to carbon monoxide ratios by tri-reforming of methane using Ni–MgO–$(Ce,Zr)O_2$ catalysts. *Applied Catalysis A: General* **2012,** *445-446*, 61-68.

163. Tang, K.; Liu, W.; Li, J.; Guo, J.; Zhang, J.; Wang, S.; Niu, S.; Yang, Y., The Effect of Exposed Facets of Ceria to the Nickel Species in Nickel-Ceria Catalysts and Their Performance in a NO + CO Reaction. *ACS Applied Materials & Interfaces* **2015,** *7* (48), 26839-26849.

164. Shan, W.; Fleys, M.; Lapicque, F.; Swierczynski, D.; Kiennemann, A.; Simon, Y.; Marquaire, P.-M., Syngas production from partial oxidation of methane over $Ce_{1-X}Ni_XO_Y$ catalysts prepared by complexation–combustion method. *Applied Catalysis A: General* **2006,** *311*, 24-33.

165. Zeng, S. H.; Fu, X.; Wang, X.; Su, H., Effect of Precursor Concentration on $CeO_2/Co_3O_4$ Catalysts for $CH_4/CO_2$ Reforming. *Catalysis Letters* **2013,** *144*.

166. Crnivec, I. G. O.; Djinovic´, P.; Erjavec, B.; Pintar, A., Effect of synthesis parameters on morphology and activity of bimetallic catalysts in $CO_2$–$CH_4$ reforming. *Chem. Eng. J.* **2012,** *207-208*, 299-307.

167. Poncelet, G.; Centeno, M. A.; Molina, R., Characterization of reduced α-alumina-supported nickel catalysts by spectroscopic and chemisorption measurements. *Applied Catalysis A: General* **2005,** *288* (1), 232-242.

168. Berlouis, L. E. A.; Jubin, C.; McMillan, B. G.; Morrow, J.; Spicer, M. D.; Tang, L. P.; Bordelanne, O.; Weston, M., Enhanced hydrogen storage in Ni/Ce composite oxides. *Phys. Chem. Chem. Phys.* **2007,** *9*, 6032-6039.

169. Senanayake, S. D.; Evans, J.; Agnoli, S.; Barrio, L.; Chen, T.-L.; Hrbek, J.; Rodriguez, J. A., Water–Gas Shift and CO Methanation Reactions over Ni–$CeO_2$(111) Catalysts. *Top. Catal.* **2011,** *54*, 34-41.

170. Fan, M.-S.; Abdullah, A. Z.; Bhatia, S., Utilization of greenhouse gases through carbon dioxide reforming of methane over Ni–Co/MgO–$ZrO_2$: Preparation, characterization and activity studies. *Appl. Catal. B: Environ.* **2010,** *100*, 365-377.

171. Lustemberg, P. G.; Ramírez, P. J.; Liu, Z.; Gutiérrez, R. n. A.; Grinter, D. G.; Carrasco, J.; Senanayake, S. D.; Rodriguez, J. A.; Ganduglia-Pirovano, M. V. n., Room-Temperature Activation of Methane and Dry Reforming with $CO_2$ on Ni-$CeO_2$(111) Surfaces: Effect of $Ce^{3+}$ Sites and Metal−Support Interactions on C−H Bond Cleavage. *ACS Catal.* **2016,** *6*, 8184-8191.

172. Saad, J. M.; Williams, P. T., Pyrolysis-Catalytic-Dry Reforming of Waste Plastics and Mixed Waste Plastics for Syngas Production. *Energy Fuels* **2016,** *30*, 3198-3204.

173. Takanabe, K.; Nagaoka, K.; Nariai, K.; Aika, K., Titania-supported cobalt and nickel bimetallic catalysts for carbon dioxide reforming of methane. *J. Catal.* **2005,** *232*, 268-275.

174. Aw, M. S.; Zorko, M.; Osojnik Črnivec, I. G.; Pintar, A., Progress in the Synthesis of Catalyst Supports: Synergistic Effects of Nanocomposites for Attaining Long-Term Stable Activity in $CH_4$−$CO_2$ Dry Reforming. *Ind. Eng. Chem. Res.* **2015,** *54*, 3775-3787.

175. Zhang, J.; Wang , H.; Dalai, A. K., Development of stable bimetallic catalysts for carbon dioxide reforming of methane. *J. Catal.* **2007,** *249*, 300-310.

176. Zhang, J.; Wang , H.; Dalai, A. K., Effects of metal content on activity and stability of Ni-Co bimetallic catalysts for $CO_2$ reforming of $CH_4$. *Appl. Catal. A: General* **2008,** *339*, 121-129.

177. Ferreira‐Aparicio, P.; Benito, M. J.; Sanz, J. L., New Trends in Reforming Technologies: from Hydrogen Industrial Plants to Multifuel Microreformers. *Catalysis Reviews* **2005,** *47* (4), 491-588.

178. Jiang, C.; Akkullu, M. R.; Li, B.; Davila, J. C.; Janik, M. J.; Dooley, K. M., Rapid screening of ternary rare-earth – Transition metal catalysts for dry reforming of methane and characterization of final structures. *Journal of Catalysis* **2019,** *377*, 332-342.

179. Jiang, C. Transition Metal-doped Rare-earth Oxysulfide Catalysts for High Temperature Dry Reforming of Methane. Ph.D., Louisiana St. Univ., Louisiana St. Univ., 2020.

180. Rogers, J. L.; Mangarella, M. C.; D'Amico, A. D.; Gallagher, J. R.; Dutzer, M. R.; Stavitski, E.; Miller, J. T.; Sievers, C., Differences in the Nature of Active Sites for Methane Dry Reforming and Methane Steam Reforming over Nickel Aluminate Catalysts. *ACS Catalysis* **2016,** *6* (9), 5873-5886.

181. Bischoff, K. B., An extension of the general criterion for importance of pore diffusion with chemical reactions. *Chemical Engineering Science* **1967,** *22* (4), 525-530.

182. Weisz, P. B.; Prater, C. D., Interpretation of Measurements in Experimental Catalysis. In *Advances in Catalysis*, Frankenburg, W. G.; Komarewsky, V. I.; Rideal, E. K., Eds. Academic Press: 1954; Vol. 6, pp 143-196.

183. PDF #00-034-0394. International Centre for Diffraction Data: Cambridge, UK, 2009; Vol. Powder Diffraction File.

184. Reddy, B. M.; Saikia, P.; Bharali, P.; Park, S.-E.; Muhler, M.; Grunert, W., Physicochemical Characteristics and Catalytic Activity of Alumina-Supported Nanosized Ceria-Terbia Solid Solutions. *J. Phys. Chem. C* **2009,** *113*, 2452–2462.

185. Atribak, I.; Bueno-López, A.; García-García, A., Combined removal of diesel soot particulates and NOx over $CeO_2$–$ZrO_2$ mixed oxides. *Journal of Catalysis* **2008,** *259* (1), 123-132.

186. PDF #00-004-0850. International Centre for Diffraction Data: Cambridge, UK, 2010; Vol. Powder Diffraction File.

187. PDF #00-047-1049. International Centre for Diffraction Data: Cambridge, UK, 2010; Vol. Powder Diffraction File.

188. Millet, M.-M.; Frei, E.; Agara-Siller, G.; Schlogl, R.; Tarasov, A., Surface titration of upported Ni catalysts by $O_2$-pulse thermal analysis. *Appl. Catal. A: Gen.* **2018,** *566*, 155-163.

189. Zhao, Y.; Dong, F.; Han, W.; Zhao, H.; Tang, Z., Construction of Cu–Ce/graphene catalysts via a one-step hydrothermal method and their excellent CO catalytic oxidation performance. *RSC Advances* **2018,** *8* (3), 1583-1592.

190. Jaiswar, S.; Mandal, K. D., Evidence of Enhanced Oxygen Vacancy Defects Inducing Ferromagnetism in Multiferroic CaMn7O12 Manganite with Sintering Time. *The Journal of Physical Chemistry C* **2017,** *121* (36), 19586-19601.

191. Tillborg, H.; Nilsson, A.; Hernnäs, B.; Mårtensson, N.; Palmer, R. E., X-ray and UV photoemission studies of mono-, bi- and multilayers of physisorbed molecules: $O_2$ and $N_2$ on graphite. *Surface Science* **1993,** *295* (1), 1-12.

192. Kwan, Y. C. G.; Ng, G. M.; Huan, C. H. A., Identification of functional groups and determination of carboxyl formation temperature in graphene oxide using the XPS O 1s spectrum. *Thin Solid Films* **2015,** *590*, 40-48.

193. Roh, H.-S.; Jun, K.-W.; Park, S.-E., Methane-reforming reactions over Ni/Ce-ZrO2/θ-Al2O3 catalysts. *Appl. Catal. A* **2003,** *251*, 275-283.

194. Ojagh, H.; Creaser, D.; Tamm, S.; Hu, C.; Olsson, L., Effect of Thermal Treatment on Hydrogen Uptake and Characteristics of Ni-, Co-, and Mo-Containing Catalysts. *Industrial & Engineering Chemistry Research* **2015,** *54* (46), 11511-11524.

195. Sciortino, L.; Giannici, F.; Martorana, A.; Ruggirello, A. M.; Liveri, V. T.; Portale, G.; Casaletto, M. P.; Longo, A., Structural Characterization of Surfactant-Coated Bimetallic Cobalt/Nickel Nanoclusters by XPS, EXAFS, WAXS, and SAXS. *The Journal of Physical Chemistry C* **2011,** *115* (14), 6360-6366.

196. Biesinger, M. C.; Payne, B. P.; Grosvenor, A. P.; Lau, L. W. M.; Gerson, A. R.; Smart, R. S. C., Resolving surface chemical states in XPS analysis of first row transition metals, oxides and hydroxides: Cr, Mn, Fe, Co and Ni. *Applied Surface Science* **2011,** *257* (7), 2717-2730.

197. Blyth, R. I. R.; Buqa, H.; Netzer, F. P.; Ramsey, M. G.; Besenhard, J. O.; Golob, P.; Winter, M., XPS studies of graphite electrode materials for lithium ion batteries. *Applied Surface Science* **2000,** *167* (1), 99-106.

198. Tien, H.-W.; Huang, Y.-L.; Yang, S.-Y.; Wang, J.-Y.; Ma, C.-C. M., The production of graphene nanosheets decorated with silver nanoparticles for use in transparent, conductive films. *Carbon* **2011,** *49* (5), 1550-1560.

199. Huang, Y.-L.; Baji, A.; Tien, H.-W.; Yang, Y.-K.; Yang, S.-Y.; Ma, C.-C. M.; Liu, H.-Y.; Mai, Y.-W.; Wang, N.-H., Self-assembly of graphene onto electrospun polyamide 66 nanofibers as transparent conductive thin films. *Nanotechnology* **2011,** *22* (47), 475603.

200. Goto, Y.; Taniguchi, K.; Omata, T.; Otsuka-Yao-Matsuo, S.; Ohashi, N.; Ueda, S.; Yoshikawa, H.; Yamashita, Y.; Oohashi, H.; Kobayashi, K., Formation of Ni3C Nanocrystals by Thermolysis of Nickel Acetylacetonate in Oleylamine: Characterization Using Hard X-ray Photoelectron Spectroscopy. *Chemistry of Materials* **2008,** *20* (12), 4156-4160.

201. Chen, Y.; Huang, S.; Ji, X.; Adepalli, K.; Yin, K.; Ling, X.; Wang, X.; Xue, J.; Dresselhaus, M.; Kong, J.; Yildiz, B., Tuning Electronic Structure of Single Layer MoS2 through Defect and Interface Engineering. *ACS Nano* **2018**, Ahead of Print.

202. Pawar, V.; Appari, S.; Monder, D. S.; Janardhanan, V., M., Study of the Combined Deactivation Due to Sulfur Poisoning and Carbon Deposition during Biogas Dry Reforming on Supported Ni Catalyst. *Ind. Eng. Chem. Res.* **2017,** *56*, 8448-8455.

203. Mamontov, E.; Egami, T.; Brezny, R.; Koranne, M.; Tyagi, S., Lattice defects and oxygen storage capacity of nanocrystalline ceria and ceria-zirconia. *J. Phys. Chem.* **2000,** *104*, 1110-1116.

204. Bonmassar, N.; Bekheet, M. F.; Schlicker, L.; Gili, A.; Gurlo, A.; Doran, A.; Gao, Y.; Heggen, M.; Bernardi, J.; Klötzer, B.; Penner, S., In Situ-Determined Catalytically Active State of $LaNiO_3$ in Methane Dry Reforming. **2020,** *10*, 1102-1112.

205. Li, L.; Chen, F.; Lu, J.-Q.; Luo, M.-F., Study of Defect Sites in $Ce_{1-x}M_xO_{2-\delta}$ (x = 0.2) Solid Solutions Using Raman Spectroscopy. *J. Phys. Chem. A* **2011,** *115*, 7972-7977.

206. Fornasiero, P.; Balducci, G.; Di Monte, R.; Kaspar, J.; Sergo, V.; Gubitosa, G.; Ferrero, A.; Graziani, M., Modification of the redox behavior of $CeO_2$ induced by structural doping with $ZrO_2$. *J. Catal.* **1996,** *164*, 173-183.

207. Goula, M. A.; Charisiou, N. D.; Siakavelas, G.; Tzounis, L.; Tsiaoussis, P.; Panagiotopoulou, P.; Goula, G.; Yentekakis, I. V., Syngas production via the biogas dry reforming reaction over Ni supported on zirconia modified with $CeO_2$ or $La_2O_3$ catalysts. *Intl. J. Hydrogen Energy* **2017,** *42*, 13724-13740.

208. Zhang, F.; Liu, Z.; Zhang, S.; Akter, N.; Palomino, R. M.; Vovchok, D.; Orozco, I.; Salazar, D.; Rodriguez, J. A.; Llorca, J.; Lee, J.; Kim, D.; Xu, W.; Frenkel, A. I.; Li, Y.; Kim, T.; Senanayake, S. D., In Situ Elucidation of the Active State of Co−CeOx Catalysts in the Dry Reforming of Methane: The Important Role of the Reducible Oxide Support and Interactions with Cobalt. *ACS Catal.* **2018,** *8*, 3550-3560.

209. Lou, Y.; Steib, M.; Zhang, Q.; Tiefenbacher, K.; Horváth, A.; Jentys, A.; Liu, Y.; Lercher, J. A., Design of stable $Ni/ZrO_2$ catalysts for dry reforming of methane. *356* **2017**, 147-156.

210. Vogt, C.; Kranenborg, J.; Monai, M.; Weckhuysen, B. M., Structure Sensitivity in Steam and Dry Methane Reforming over Nickel: Activity and Carbon Formation. *ACS Catal.* **2020,** *10* (2), 1428-1438.

211. Zuo, Z.; Liu, S.; Wang, Z.; Li, C.; Huang, W.; Huang, J.; Liu, P., Dry Reforming of Methane on Single-Site Ni/MgO Catalysts: Importance of Site Confinement. *ACS Catal.* **2018,** *8*, 9821-9831.

212. Liang, T.-Y.; Lin, C.-Y.; Chou, F.-C.; Wang, M.; Tsai, D.-H., Gas-Phase Synthesis of $Ni–CeO_x$ Hybrid Nanoparticles and Their Synergistic Catalysis for Simultaneous Reforming of Methane and Carbon Dioxide to Syngas. *The Journal of Physical Chemistry C* **2018,** *122* (22), 11789-11798.

213. Wei, J.; Iglesia, E., Isotopic and kinetic assessment of the mechanism of reactions of $CH_4$ with $CO_2$ or $H_2O$ to form synthesis gas and carbon on nickel catalysts. *Journal of Catalysis* **2004,** *224* (2), 370-383.

214. Wang, N.; Shen, K.; Huang, L.; Yu, X.; Qian, W.; Chu, W., Facile Route for Synthesizing Ordered Mesoporous Ni–Ce–Al Oxide Materials and Their Catalytic Performance for Methane Dry Reforming to Hydrogen and Syngas. *ACS Catalysis* **2013,** *3* (7), 1638-1651.

215. Shirley, D. A., High-Resolution X-Ray Photoemission Spectrum of the Valence Bands of Gold. *Physical Review B* **1972,** *5* (12), 4709-4714.

216. Stern, E. A., Structure determination by X-ray absorption. *Contemporary Physics* **1978,** *19* (4), 289-310.

217. Stern, E.; Heald, S., Basic principles and applications of EXAFS. *Handbook on synchrotron radiation* **1983,** *1*, 955-1014.

218. Kelly, S. D.; Hesterberg, D.; Ravel, B., Analysis of Soils and Minerals Using X-ray Absorption Spectroscopy. In *Methods of Soil Analysis Part 5—Mineralogical Methods*, 2008; pp 387-463.

# VITA

Changyi Jiang was born in Dalian, China. After graduating from Dalian No. 24 high school, he attended Dalian University of Technology in 2006, where he obtained his bachelor's degree in chemical engineering. He came to the United States in 2011 and acquired his master's degree at Michigan Technological University. In spring of 2016, he joined Dr. Kerry Dooley's research group at Louisiana State University to continue graduate studies. He expects to receive a Ph.D. in Chemical Engineering in May 2020.

**Publications and presentations**

Refereed journal publications:

**Jiang, C.**; Akkullu, M. R.; Li, B.; Davila, J. C.; Janik, M. J.; Dooley, K. M., Rapid Screening of Ternary Rare-earth – Transition Metal Catalysts for Dry Reforming of Methane and Characterization of Final Structures. *Journal of Catalysis* **2019,** *377*, 332-342.

Safavinia, B.; Wang, Y.; **Jiang, C.**; Roman, C.; Darapaneni, P.; Larriviere, J.; Cullen, D. A.; Dooley, K. M.; Dorman, J. A., Enhancing $Ce_xZr_{1-x}O_2$ Activity for Methane Dry Reforming Using Subsurface Ni Dopants. *ACS Catalysis* **2020**, 4070-4079.

**Jiang, C.**; Loisel, E.; Dorman, J. A. ; Cullen, D.A.; Dooley, K. M., On the Enhanced Sulfur and Carbon Tolerance of Ni-Co Doped Rare-Earth Oxide Catalysts for Dry Reforming of Methane. *Applied Catalysis A: General* (in preparation)

Conference presentations:

Dooley, K. M.; **Jiang, C.**; Janik, M. J.; Li, B.; Lee, J., "Towards the Design of Sulfur-Tolerant $CO_2$-Reforming Catalysts," AIChE Annual Meeting, Minneapolis, MN, 2017.

**Jiang, C.**; Lee, J.; Li, B.; Janik, M. J.; Dooley, K. M., "Ternary Oxides for Dry Reforming of Methane: Rapid Screening of Rare-Earth - Transition Metal Catalysts and Sulfur Tolerance Evaluation", North America Catalysis Society Meeting, Chicago, IL, 2019.

**Jiang, C.**; Janik, M. J.; Li, B.; Loisel, E.; Dooley, K. M., "Ternary Rare-Earth–Transition Metal Catalysts for Dry Reforming of Methane, Characterization of Final Structures and Sulfur Tolerance Evaluation", AIChE Annual Meeting, Orlando, FL,2019